REPORT NO.
UCB/EERC-85/02
MARCH 1985

EARTHQUAKE ENGINEERING RESEARCH CENTER

ESTIMATION OF SEISMIC WAVE COHERENCY AND RUPTURE VELOCITY USING THE SMART 1 STRONG-MOTION ARRAY RECORDINGS

by

N. A. ABRAHAMSON

Report to the National Science Foundation
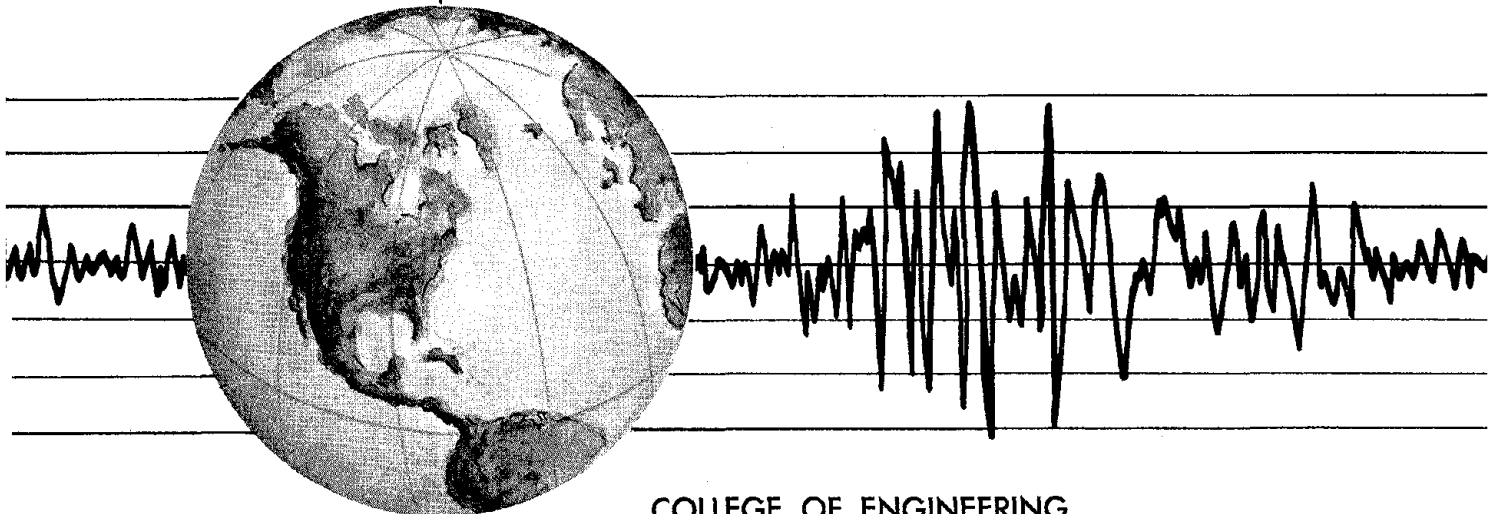
COLLEGE OF ENGINEERING

UNIVERSITY OF CALIFORNIA · Berkeley, California

PREFACE

This is the second report to be published by the Earthquake Engineering Research Center describing work done with the large-scale digital array of surface strong-motion accelerometers in Taiwan. The array is named SMART 1 (Strong Motion Array Taiwan, number 1) and a preliminary report on it was given in UCB/EERC-82/13 (August 1982) by B. A. Bolt, C. H. Loh, J. Penzien, Y. B. Tsai, and Y. T. Yeh.

The installation of SMART 1 began in September 1980 and by January 1981, 27 instruments were in place. Financial support has come from the National Science Foundation and the National Research Council in Taiwan. By June 1982, the full array was in place with all instruments exhaustively tested and field calibrated and the basic playback and computer analysis procedures developed. By June 1984, 28 earthquakes had triggered all or part of the array. Data reduction methods have been developed at both the Institute of Earth Sciences, Taipei, and the Seismographic Station, U.C. Berkeley. Programs were developed for computer analyses of the array data, including cross-correlation of travelling waves and generalized spectral response information.

Following recommendations of a Special International Seminar in Taipei in 1981, the Principal Investigator in Taiwan (Professor Y. B. Tsai) agreed to assume costs for almost all instrumental maintenance and development; the National Research Council now provides funds for operation and field maintenance, as well as data preparation and basic analysis at the Institute of Earth Sciences, Taipei. Two additional digital accelerographs have been installed to extend the array, and seismic refraction surveys have been completed at the site.

From the beginning of the research project it was anticipated that there would be considerable demand for accelerograms both in raw and corrected form. Many requests have been received from researchers in a number of countries for data tapes. Normally these are supplied at cost in the form of 9-track standard tapes in ASCII format. The file of tapes is kept at the Institute ot Earth Sciences, Taipei, and at the Seismographic Station, University of California, Berkeley. In addition, copies of a set of corrected ground motions have been placed in

i

standard tape form with the World Data Center in Colorado, operated for dissemination purposes by the National Oceanographic and Atmospheric Agency, and the U.S. Geological Survey.

The research reported in the following pages was carried out for the requirements of a Ph.D. dissertation by Dr. N. A. Abrahamson. In the various chapters he describes a number of important new developments using the array recordings. In particular, the attention of the reader is drawn to (a) studies of incoherent and frequency dependent scattered energy passing across the array, and (b) to the development of seismic response phase spectrum defined to compliment the usual Housner response (amplitude) spectrum. The latter concept should be of value in the analysis of structural systems which need multi-support inputs. Finally, some details of the rupture velocity of the fault rupture source in a large 1981 earthquake are estimated, using measurements of the phasing of wave fronts of coherent P and S waves across SMART 1. This estimate of rupture velocity is believed to be the first obtained with a two-dimensional strong-motion array.

<div style="text-align:right">

Professors Bruce A. Bolt
Joseph Penzien
Y. B. Tsai
Principal Investigators

</div>

Abstract

The January 29, 1981 Taiwan earthquake (M_L=6.7) was recorded digitally by 27 triaxial force-balanced accelerometers in the SMART 1 strong motion array centered 30 km north-northwest of the epicenter. The seismic source of this event had a reverse mechanism with unilateral rupture from east to west.

The array recordings are used to make direct measurements of the wave coherency and the time dependent rupture velocity. Frequency-wavenumber analysis shows that across the 4 km array, the P waves contain coherent energy from the source region at frequencies up to 6 Hz while the S waves contain coherent energy up to 3 Hz. Significant energy is present in the P and S waves at frequencies above these two levels, but it is incoherent or scattered energy.

The time dependent rupture velocity is estimated by measuring the time dependent phasing of the coherent P and S waves across the array. Temporal changes in the azimuth of the wavefronts provide a direct measurements of the moving source. The rupture velocity varies from a minimum of 2.1 km/sec to a maximum of 4.9 km/sec over a fault length of 14 km.

Engineering implications of coherent non-vertically propagating waves are explored by measuring the dynamic response ratio which indicates the relative amplitude of the dynamic response of the structure compared with the traditional response spectrum. Phase shifts in the ground motion across the array caused by non-vertically propagating waves produce up to a 25% reduction in the response spectrum at 5 Hz for rigid structures spanning a distance of 200 meters. The out-of-phase dynamic response ratio of a flexible structure with a period of 1 second and a support spacing of 200 meters is measured at 0.20-0.40 indicating that non-vertically propagating waves can produce a significant amount of out-of-phase energy for large engineered structures.

Acknowledgments

Table of Contents

Chapter 1

Introduction

Earthquake sources are sometimes represented as point sources whose positions are specified simply by their hypocenters. This elementary model of the seismic source is adequate for many seismological problems, although in order to study the details of the source mechanism, seismic sources should be represented as propagating ruptures. For small events, the rupture length is short so that effects of the rupture are difficult to observe. For large earthquakes, however, the rupture has an important effect on the observed seismograms. The effect of a propagating rupture on the seismograms becomes even more significant in the near-source region and one of the key source parameters which needs to be estimated is the time-dependent rupture velocity.

The seismic recordings of the 1952 Kern County Earthquake provided some of the earliest estimates of a direction and an average velocity for the moving rupture. The aftershocks were located primarily northeast of the epicenter indicating that the rupture direction was toward the northeast. Gutenberg (1955) noted a tenfold increase in teleseismic Rayleigh wave amplitudes recorded at azimuths northeast of the epicenter compared to the amplitudes recorded southwest of the epicenter. He interpreted this strong variation to be an interference pattern due to the moving source, and surmised that the rupture velocity had to be not much less than the Rayleigh wave velocity, in order to produce the observed amplitude variations.

Benioff (1951) showed that the finite speed of the rupture resulted in an asymmetrical radiation pattern for the seismic wave energy. In particular, the waves in the forward direction have larger amplitudes and shorter periods than waves in the backward direction. He later

1

interpreted the large shear wave amplitudes in the northeast direction from the 1952 Kern County Earthquake as caused by constructive interference of S waves and estimated the rupture velocity to be in the neighborhood of 0.9 β , where β is the shear wave velocity (Benioff, 1955).

A frequency domain approach for estimating an average rupture velocity from seismograms was developed by Ben-Menahem (1961). He noted that a simple moving source should produce regular spectral nulls caused by the interference of the waves emitted at different times along the fault. He proposed a "directivity function" measured from two stations located diametrically opposite of each other with respect to the source (see Aki and Richards, 1980 pages 636-639). By forming spectral ratios of surface waves from such diametrically opposed stations, all factors should cancel except for the effects of fault orientation, fault length and rupture velocity. The estimated directivity function was compared to theoretical directivity functions for various source mechanisms with various fault lengths and constant rupture velocities. A graphical inversion technique provided an estimate of the mean rupture velocity. He applied the method to teleseismic surface waves observed from large earthquakes. In particular, he estimated the rupture velocity of the 1957 Mongolian earthquake (M_s=7.75) at 2.5 km/sec (Ben-Menahem and Toksöz, 1962). Later, a "directivity function" formulation was developed corresponding to a variable rupture velocity (Ben-Menahem and Toksöz, 1962). The directivity method was also extended to consider any two station pairs rather than requiring diametrically opposite stations (Udias, 1971).

An early successful application of the spectral null model at regional distances was done by Filson and McEvilly (1967). They examined the Love wave spectrum recorded at Berkeley from the 1966 Parkfield Earthquake (M_L=5.5). The observed spectral nulls could be explained by a constant rupture velocity of 2.2 km/sec.

Another approach to the rupture velocity estimation problem considers the rupture as the superposition of a finite number of subevents. Each subevent is identified by a P and/or S wave and is individually located. The spatial separation of successive subevents along with the

difference in origin times gives the rupture velocity estimate. This method was used by Wyss and Brune (1967) and Nagamune (1971) to estimate the rupture speeds for the 1964 Alaskan (v = 3.5 km/sec) and the 1960 Chilean (v = 4.9 km/sec) earthquakes respectively. In both of these studies, the authors were able to distinguish multiple P phases but could not identify the corresponding multiple S phases.

Brune (1970, 1971) modeled the far-field Fourier displacement spectrum of SH waves for a simple source mechanism. The ω^2 or "Brune" spectrum has a 2 slope high frequency asymptote due to the finite source time and the finite fault length. The rupture velocity is related to the corner frequency of the Fourier amplitude spectrum where the corner frequency is defined as the frequency where the long period level and the high frequency asymptote intersect. This model essentially forms an upper envelope to the sinc function model that produces the spectral nulls mentioned earlier. The rupture velocity estimate is given by

$$V_r = \frac{\beta}{\frac{2\beta}{L\omega_c} + \cos\theta_o},$$

where β is the shear wave velocity, L is the fault length, ω_c is the corner frequency and θ_o is the angle between the rupture direction and the station azimuth. This method provides simple and inexpensive estimates of the rupture velocity from single station recordings.

The estimation of average rupture velocities by the above methods lead to empirical relations such as

$$\log(\frac{L}{V_r}) = 0.5\,M - 1.9$$

where M is the magnitude (Båth, 1979, chapter 8). Combined with a magnitude-fault length relation (Tocher, 1958), this empirical relation implies that rupture velocity is simply a function of magnitude. Such empirical relations, represent an over-simplification of the rupture process and do not provide information on the details of the rupture process.

The above methods provide estimates of the rupture process using long period waves. The long period waves provide average features of the rupture process. The high frequency energy emitted at the rupture front must be analyzed to study the fine details of the rupture.

One promising way to accomplish these measurements is to use high frequency array recordings from the near-source region.

The 1979 Imperial Valley Earthquake provided valuable array recordings of strong ground motion in the near-source region. The rupture that propagated through the network has been modeled in a variety of ways. One approach used was to discretize the fault into a finite sum of point sources. The time of the generation of each source and the amplitude and direction of slip were fit by waveform modeling. Hartzell and Heaton (1983) used forward modeling of displacements recorded by the El Centro network. They estimated the average rupture velocity at 2.5 - 2.7 km/sec. Olson and Apsel (1982) used a least-squares inversion of long period (T > 1 second) accelerations from the El Centro network to estimate the temporal and spatial distribution of slip. They obtained a horizontal rupture velocity between 4.0 and 5.0 km/sec. Hartzell and Helmburger (1982) modeled both teleseismic body waves and strong motion recordings simultaneously. They inferred an average rupture velocity of 2.5 km/sec. Their analysis suggested an acceleration of the rupture front from 2.2 km/sec near the hypocenter to 2.8 km/sec approximately 12 km northward along the fault. Waveform modeling is computationally expensive and to date has been unable to match recordings at frequencies greater than 1 Hz because at high frequencies, the waveforms are very sensitive to the fine details of the velocity structure between the fault and the receiver.

The recordings from the 213 meter linear El Centro Differential Array have been used by a number of researchers to study the rupture process of the 1979 Imperial Valley Earthquake. Niazi (1982) measured the time dependent polarization of the relatively long period (T > 1 second) P waves recorded on the horizontal components which indicated a rupture velocity between 2 - 3 km/sec during the first five seconds. After five seconds, the P waves on the horizontal components were contaminated by the S wave arrivals. Chu (1984) examined the Fourier amplitude spectra for a Doppler shift from a moving source with a constant velocity. His estimate of the mean rupture velocity is 2.085±0.045 km/sec. Spudich and Cranswick (1984) used a cross correlation method to measure the slowness of the P and S waves at the

4

differential array. With detailed knowledge of the velocity structure, the slowness observed at the differential array was correlated to a source position on the fault surface. In this manner, the fault surface was contoured in slowness forming "slowness maps". They estimated the average rupture velocity between 2.6 - 3.2 km/sec and suggested that the rupture velocity briefly accelerated up to speeds near the P wave velocity. Although slowness mapping provided additional insights into the rupture process, a major difficulty in the application of the method was the restriction to a scalar slowness rather than a vector slowness caused by the uni-dimensional array. The absence of a second dimension to the array resulted in a surface of possible source positions for any given slowness measured at the array making it impossible to determine uniquely the rupture velocity.

Two dimensional strong motion arrays were the subject of the international workshop on strong motion earthquake instrument arrays held in Honolulu, Hawaii in 1978 (Iwan, 1978). At the workshop, it was noted that two dimensional strong motion arrays with a common time base would be very useful for studying the details of the earthquake mechanism and wave propagation. Recordings from a two dimensional array provide direct measurements of the speed and azimuth of the seismic waves as they propagate through the array. In terms of engineering requirements for large structures, measurements of the ground motion at a single point are not adequate. A description of the gradients of ground motion that give rise to rocking, rotation and flexing of engineered structures is also needed.

The seismological goals of this thesis are to measure the coherency of the seismic waves using two dimensional array recordings, and to determine the dependence of the coherency on frequency, station separation and wave type. In a related study already published, a qualitative description of wave coherency observed during the 1971 San Fernando earthquake is given in Liu and Heaton (1984). Although absolute time is not available for the San Fernando strong motion recordings, these authors were able to observe coherent phase arrivals in the velocity and acceleration time time histories across distances of kilometers.

The central procedure in the following work is to analyze the spatial variations of the

Fourier phase of the coherent energy using frequency-wavenumber analysis and to attempt to follow the dislocation as it moves along the rupturing fault. By analyzing the spatial phasing over narrow frequency bands, the incoherent energy is separated from the coherent energy. This method removes some of the uncertainty that is inherent in a wide-band analysis such as the method used by Spudich and Cranswick. Frequency-wavenumber analysis leads to direct measurements of the time-dependent rupture velocity.

To accomplish these goals, recordings from the SMART 1 strong motion array will be used. The SMART 1 array is a large digital strong motion array with dense spatial coverage. The array is deployed in the highly seismic region of northeastern Taiwan. A large earthquake ($M_L = 6.7$) in 1981 recorded by the array has been selected for analysis. This earthquake source appears to have unilateral rupture which greatly simplifies the problem of following the moving rupture front. Its epicenter is 30 km southeast of the array (see figure 3.3) so that the westerly rupture does not pass through the array. Consequently, there are limits on the azimuthal variation of the seismic waves recorded at the array. The size and geometry of the source, however, provide sufficient azimuthal variation so that time dependent rupture velocity estimates may be made.

Chapter 2

The SMART 1 Array

2.1 Introduction

The SMART 1† array is located in the northeast corner of Taiwan near the city of Lotung on the Lan-yang Plain (figure 2.1). Installation of the array began in September 1980 and was completed in August 1982. The original array consisted of 37 force-balanced triaxial accelerometers configured in three concentric circles of radii 200m, 1000m and 2000m (figure 2.2). The three rings are named I (inner), M (middle) and O (outer), respectively. There are twelve equally spaced stations numbered 1 through 12 on each ring and a central station named C-00. The minimum station spacing is 100 m. In June 1983, two additional stations were added to the array. These stations named E-01 and E-02 are located 2.8 km and 4.8 km south of the central station respectively (figure 2.2).

During the first four years of operation, 28 events triggered all or part of the array. This set of events contained both reverse and strike-slip mechanisms associated with a subduction zone and transform faults. Lists of these events are given in tables 2.1 and 2.2 and the epicenters are plotted in figure 2.3. The largest acceleration recorded by the array through August 1984 is 0.24g from event 5. Details of this event are given in chapter 3.

---

† Strong Motion Array in Taiwan number 1

7

2.2 Geology

A geologic map of the Lan-yang Plain is shown in figure 2.4. The SMART 1 array, shown by the three concentric circles, is located on recent alluvium. The area is primarily rice fields so that the water table is at or near the ground surface. The topography is very flat with elevations ranging between 2.4 and 18.1 meters across the array (Table 2.3). The majority of the stations have elevations between 4.0 and 8.0 meters. Two cross sections running north-south are shown in figure 2.5. Dipping structures are clearly evident especially in the Eocene slate bedrock. The soils beneath the array consist of 4-12 meters of clays and muds over recent alluvium down to 50 meters. Below this layer are gravels and as is typical in alluvial fans, the size of the pebbles in the gravels increases with depth. The bedrock below the gravels consists of slate. The depth to the bedrock below the main array varies from 170 meters in the southern end of the outer ring to 600 meters in the northern part of the array. The extended array station E-02 is located on a slate outcrop and is considered a rock site.

P wave velocity profiles below the array running east-west and north-south are shown in figure 2.6. The P wave velocity profiles were obtained by refraction methods by the Institute of Earth Sciences during the summer of 1983. They dropped a 500 kg weight and measured P wave arrival times (Wen and Yeh, 1983). The profiles were all reversed so the dip in the lower structure on the north-south cross section is well determined. Unfortunately, S wave velocities are not available at this time.

2.3 Instruments

The seismometers used in the SMART 1 array are the SA-3000 triaxial accelerometers produced by Columbia for Sprengnether Instruments Inc. The natural frequency of the accelerometers is given as 140 Hz in the instruction manual (Sprengnether, 1980) but it is closer to 80 Hz.[1] The sensitivity of the SA-3000 is 3.75 volts/g with 2g full scale. Its resolution

---

[1] A horizontal unit was tested on a shaking table at the U. C. Seismographic Station. The corner frequency was found to be at approximately 80 Hz.

is 0.001 percent full scale or 2×10^{-6}g. Additional specifications of the SA-3000 accelerometer are given in Bolt *et al.* (1982, table 2.2).

The recorders are DR-100 digital event recorders that are 12 bit (± 2048 counts) systems. The dynamic range is 66 db. When combined with the SA-3000 accelerometer, the recording resolution is approximately 1 cm/sec^2 (1 count ≈ 0.96 gal). The DR-100's record on cassette tape at a sample rate of 100 samples per second.[2] The recording unit has a 5-pole Butterworth low-pass antialias filter at 25 Hz. The analog to digital converter samples each of the three channels every third of a sample so the samples from the three channels are taken 3.3 msec and 6.6 msec apart. This time delay is important if the phasing between the different channels is compared.

Each recorder is triggered individually. The triggering mechanism activates the recorder when the absolute acceleration exceeds the preset threshold (nominally 0.02g) on any one of the three components. The digital delay memory has a capacity of 250 samples per channel that corresponds to 2.5 seconds of pre-event memory at 100 samples per second.

The instruments sit on a 4" thick concrete pad with dimensions approximately 2'×3' poured in place over a steel wire mesh. Tie-down bolts anchor both the battery power supply and the recorder to the surface pad to prevent any spurious sources during a large earthquake. The whole system is covered by a fiberglas structure about 3' tall.

Each instrument is serviced once every three days. The maintenance includes measuring the clock drift using a comparator[3], checking the tape and changing the battery power supply. Such frequent maintenance is necessary to maintain accurate timing and because digital recorders require much more power than analog recorders. Typical clock drift curves are shown in figure 2.7. The largest clock drift rate is 10 msec per day. After every significant event, the clock corrections are measured again and the tapes are changed. The time correction is determined by linearly interpolating the measured clock drift. This correction should be accurate to

---

[2] The sample rate is actually 100.21 samples per second due to a clock design error.

[3] Clock drift measurements are given in Liu, 1981.

better than 5 msec.

Over the four years of use, the performance of the instruments has been excellent[4]. Part of the success can be attributed to the extensive testing that was done on each accelerometer and recorder at Berkeley before being shipped to Taiwan (Bolt *et al.*, 1982, chapter 2) but much of the success is also due to the careful field maintenance of the array instrumentation by staff of the Institute of Earth Sciences, Academia Sinica.

2.4 Seismicity and Tectonics of Taiwan

Taiwan is part of the Ryukyu-Taiwan-Philippine arc system and can be viewed as a transform zone between two subduction zones with very different geometries. Seismically, Taiwan is much more active than its neighbors, the Ryukyu and Luzon (Wu, 1978). This high rate of seismicity is due to the complicated interaction between the Eurasian and Philippine plates.

A simplified picture of the tectonics is shown in figure 2.8. In the east, the plate boundary is defined by the Ryukyu trench. Approximately 100-150 km east of Taiwan, the Ryukyu trench is offset by a right-lateral strike-slip fault. The subduction is displaced to the north relative to the Ryukyu trench and continues to the island edge, where it connects to the thrust-left-lateral Longitudinal Valley fault zone. This fault zone is not a simple transform fault, but rather a collision boundary with a strike-slip component. South of Taiwan, it is difficult to define a plate boundary. At approximately 21° north latitude the plate boundary becomes a right-lateral strike-slip fault that joins with the Manila trench (Lin and Tsai, 1981)

The complicated tectonics in the Taiwan region lead to a high rate of seismicity with a variety of focal mechanisms. The epicenters determined by the 26 stations of the Taiwan Telemetered Seismic Network (see figure 3.3) from 1975 to 1983 are shown in figure 2.9 and the hypocenters are shown in a three dimensional plot in figure 2.10. In most cases, the shallow seismicity does not correlate well with known faults (Wu, 1978) although some clear fault

---

[4] The array performance is discussed in appendix B

10

related concentrations of micro earthquakes have been found.

The SMART 1 array is located in the northeast corner of Taiwan. In this region, there is a high concentration of both shallow and intermediate depth earthquakes. This positioning of the SMART 1 array provides the opportunity to study strong motion recordings from a variety of earthquake mechanisms at various focal depths.

TABLE 2.1 Events Recorded by the SMART 1 Array

Event	Origin Time (UTC)		Latitude	Longitude	Depth	Ref	M_L	m_b	M_S	Mechanism
1	80 Oct 18	00:08:23.4	24.36° N	121.89° E	27	I	5.7	5.1	5.7	
2	80 Nov 14	13:37:01.5	24.61° N	121.75° E	81	T	5.9	5.1	4.9	
3	80 Nov 14	13:38:	24.42° N	121.77° E	10	T	5.6			
4	81 Jan 24	14:10:31.6	23.93° N	121.70° E	61	I	5.4	4.8		
5	81 Jan 29	04:51:34.5	24.44° N	121.92° E	25	A	6.7	5.7	5.7	R
6	81 Feb 27	02:27:	24.68° N	121.85° E	76	I	5.1	4.6		
7	81 Mar 02	12:13:46.2	22.88° N	121.47° E	25	I	6.5	5.4	6.2	
8	81 Mar 10	08:24:49.2	24.83° N	122.03° E	10	I	3.2			
9	81 Mar 22	21:25:33	24.70° N	121.8 ° E	5	I	3.5			
10	81 May 03	19:19:49.0	24.69° N	122.23° E	75	I	4.9	3.7		
11	81 Jun 01	11:53:46	24.44° N	121.9 ° E	10	I	4.6	3.5		
12	81 Aug 20	19:03:26	24.86° N	122.04° E	12	I	3.7	4.1		
13	81 Aug 20	20:55:03.7	24.80° N	122.09° E	10	I	3.8			
14	81 Aug 30	18:54:53.6	24.50° N	121.93° E	20	I	5.0			
15	81 Oct 05	13:24:30.5	24.66° N	121.74° E	4	T	3.4			
16	82 Jan 23	14:10:40.7	23.92° N	121.74° E	13	I	6.5	5.6	6.2	
17	82 Feb 21	06:04:37.4	24.79° N	121.90° E	11	I	3.8			
18	82 Feb 28	13:23:36.0	24.81° N	121.92° E	15	I	4.4	4.4		
19	82 Apr 01	04:50:01	24.58° N	122.1 ° E	17	I	4.2			
20	82 Dec 17	02:43:03.7	24.60° N	122.55° E	87	E	6.9	6.1		R
21	83 Apr 26	15:26:40.3	24.65° N	122.59° E	116	E	6.6	5.7		
22	83 May 10	00:15:05.6	24.42° N	121.56° E	28	E	6.3	5.6	5.4	
23	83 Jun 21	14:48:07.3	24.20° N	122.42° E	37	E	6.8	5.8	6.3	R/SS
24	83 Jun 24	09:06:45.8	24.18° N	122.40° E	44	E	7.2	6.1	6.7	R/SS
25	83 Sep 21	19:20:42.5	24.10° N	122.15° E	28	E	7.1	6.0	6.4	R/SS
26	84 Feb 23	12:15:25.8	25.91° N	121.20° E	33	P	5.2	4.5		
27	84 Mar 28	09:11:18.6	24.09° N	122.65° E	39	P	6.6	5.5	5.9	
28	84 Apr 18	01:34:17.2	24.90° N	122.43° E	33	P	5.3	4.9	3.6	

M_L is determined by the Institute of Earth Sciences, Taipei using the Taiwan Telemetered Seimic Network (TTSN) and a Wood-Anderson instrument located at Taipei.

References: A = Abrahamson, E = EDR, I = ISC, P = PDE, T = Taipei, IES.

Mechanism: SS = Strike-Slip, R = Reverse

TABLE 2.2 Events Recorded by the SMART 1 Array

Event	M_L	Depth (km)	Δ (km)	Azimuth (Deg)	T/I†	Maximum Accelerations (gal)		
						V	EW	NS
1	5.7	27	36	192	16/20	14.2	21.2	24.4
2	5.9	81	7	168	16/21	29.7	68.7	78.5
3	5.6	10	28	179	13/21	10.4	23.4	24.5
4	5.4	61	83	185	2/27	3.2	7.9	9.0
5	6.7	25	30	149	27/27	91.6	158.7	243.6
6	5.1	6	9	86	10/27	4.3	13.7	12.9
7	6.5	25	201	189	3/27	2.8	7.1	10.8
8	3.2	10	32	57	19/27	15.5	23.2	34.1
9	3.5	5	5	51	12/28	13.4	23.0	19.3
10	4.9	75	48	88	10/28	16.3	21.1	18.5
11	4.6	10	29	152	8/28	19.4	14.6	14.4
12	3.7	12	35	54	18/36	22.7	23.0	35.4
13	3	10	36	67	14/36	19.9	26.0	35.4
14	5.0	20	26	139	31/36	18.6	32.4	44.2
15	3.4	4	3	239	29/37	42.1	95.7	55.5
16	6.5	13	84	182	11/36	12.4	23.9	24.9
17	3.8	11	19	47	8/35	22.0	27.8	26.8
18	4.4	15	22	46	24/36	31.6	69.9	90.0
19	4.2	17	36	107	28/35	21.1	39.2	30.6
20	6.9	87	81	96	36/36	31.8	62.8	86.1
21	6.6	116	84	92	11/36	12.4	49.8	24.9
22	6.3	28	35	217	35/37	45.9	70.8	64.1
23	6.8	37	85	128	25/37	13.4	27.8	37.3
24	7.2	44	85	130	31/37	23.9	53.6	65.1
25	7.1	28	75	148	36/38	18.2	35.4	36.4
26	5.2	33	149	157	10/37	8.6	30.1	45.6
27	6.6	39	111	126	11/37	11.8	17.0	20.0
28	5.3	33	72	70	28/37			

† T/I = Number of stations triggered / Number of stations installed.

13

TABLE 2.3 SMART 1 Station Coordinates (as of 7/6/83)

Station	Relative to C-00 East (m)	Relative to C-00 North (m)	Longitude (E)	Latitude (N)	Radius (m)	Azimuth	Elevation (m)
C-00	0.0	0.0	121° 45' 53.23"	24° 40' 25.55"	0.0		6.1
I-01	30.5	190.9	121° 45' 54.33"	24° 40' 31.76"	193.3	9.07	5.9
I-02	132.5	141.6	121° 45' 57.93"	24° 40' 30.15"	193.9	43.10	5.5
I-03	193.6	65.1	121° 46' 00.09"	24° 40' 27.67"	204.2	71.41	6.1
I-04	202.2	-43.2	121° 46' 00.40"	24° 40' 24.15"	206.8	102.05	6.1
I-05	150.9	-134.0	121° 45' 58.58"	24° 40' 21.20"	201.8	131.60	6.3
I-06	45.5	-188.2	121° 45' 54.84"	24° 40' 19.46"	193.6	166.42	6.6
I-07	-51.8	-193.8	121° 45' 51.39"	24° 40' 19.22"	200.6	194.98	6.3
I-08	-122.3	-142.4	121° 45' 48.89"	24° 40' 20.92"	187.7	220.65	6.2
I-09	-196.7	-64.2	121° 45' 46.25"	24° 40' 23.46"	206.9	251.93	7.0
I-10	-196.3	36.5	121° 45' 46.30"	24° 40' 26.74"	199.7	280.53	7.0
I-11†	-136.1	120.3	121° 45' 48.40"	24° 40' 29.46"	181.6	311.46	6.8
I-12	-59.2	192.5	121° 45' 51.13"	24° 40' 31.81"	201.4	342.90	6.4
M-01†	186.6	938.6	121° 45' 59.87"	24° 40' 56.05"	956.9	11.24	5.0
M-02†	696.9	850.9	121° 46' 18.00"	24° 40' 53.21"	1099.9	39.32	4.4
M-03	879.6	348.4	121° 46' 24.45"	24° 40' 36.87"	946.1	68.39	4.0
M-04	988.3	-219.9	121° 46' 28.26"	24° 40' 18.20"	1012.5	102.55	4.5
M-05	743.0	-608.1	121° 46' 19.54"	24° 40' 05.79"	960.1	129.30	3.9
M-06	307.4	-954.5	121° 46' 04.10"	24° 39' 54.53"	1002.7	162.15	4.3
M-07	-265.0	-987.9	121° 45' 43.84"	24° 39' 53.44"	1022.9	195.01	5.2
M-08	-639.2	-747.8	121° 45' 30.58"	24° 40' 01.25"	983.7	220.52	7.4
M-09	-961.9	-379.0	121° 45' 19.13"	24° 40' 12.23"	1033.9	248.49	10.8
M-10	-913.0	135.7	121° 45' 20.84"	24° 40' 29.96"	923.0	278.46	7.6
M-11	-740.4	675.1	121° 45' 26.93"	24° 40' 47.49"	1002.0	312.36	7.1
M-12†	-294.6	959.2	121° 45' 42.77"	24° 40' 56.73"	1003.5	342.93	5.8
O-01†	389.9	1988.5	121° 46' 07.14"	24° 41' 30.18"	2026.4	11.09	5.3
O-02	1348.7	1487.8	121° 46' 41.23"	24° 41' 13.91"	2008.2	42.19	4.9
O-03	1948.0	608.0	121° 47' 02.42"	24° 40' 45.31"	2040.7	72.67	3.4
O-04	1949.3	-370.7	121° 47' 02.31"	24° 40' 13.50"	1984.3	100.77	2.4
O-05	1538.4	-1276.5	121° 46' 47.63"	24° 39' 44.06"	1999.0	129.68	3.8
O-06	627.4	-1909.8	121° 46' 15.37"	24° 39' 23.48"	2010.2	161.81	4.8
O-07	-381.1	-1964.1	121° 45' 39.74"	24° 39' 21.81"	2000.8	190.98	7.2
O-08	-1298.8	-1594.3	121° 45' 07.30"	24° 39' 33.73"	2056.4	219.17	18.1
O-09	-1921.0	-702.0	121° 44' 45.19"	24° 40' 02.73"	2045.2	249.92	9.6
O-10	-1953.5	442.5	121° 44' 43.88"	24° 40' 39.93"	2002.9	282.76	13.4
O-11	-1440.8	1312.3	121° 45' 01.99"	24° 41' 08.20"	1948.8	312.33	9.1
O-12	-599.5	1904.2	121° 45' 31.90"	24° 41' 27.44"	1996.4	342.53	6.5
E-01	-34.6	-2779.0	121° 45' 52.00"	24° 38' 55.42"	2779.2	180.71	5.2
E-02	-383.6	-4805.7	121° 45' 39.61"	24° 37' 49.69"	4820.9	184.56	9.7

† Station has been moved, see previous locations

TABLE 2.3 (Continued)

Previous Locations

Station	Relative to C-00 East (m)	North (m)	Longitude (E)	Latitude (N)	Radius (m)	Azimuth	Elevation (m)
From 4/20/81 to 11/20/82:							
I-11	-100.6	108.2	121° 45' 49.66"	24° 40' 29.06"	147.7	317.08	6.3
From 10/18/80 to 5/30/81:							
M-01	193.3	972.9	121° 46' 00.12"	24° 40' 57.05"	991.9	11.24	5.5
From 10/18/80 to 1/1/81:							
M-02	696.6	850.6	121° 46' 18.05"	24° 40' 53.09"	1099.4	39.31	4.4
From 10/15/80 to 12/20/82:							
M-12	-290.4	978.3	121° 45' 42.92"	24° 40' 57.28"	1020.5	343.47	5.9
From 12/24/80 to 7/6/83:							
O-01	383.6	2047.3	121° 46' 06.85"	24° 41' 31.95"	2083.0	10.61	5.4
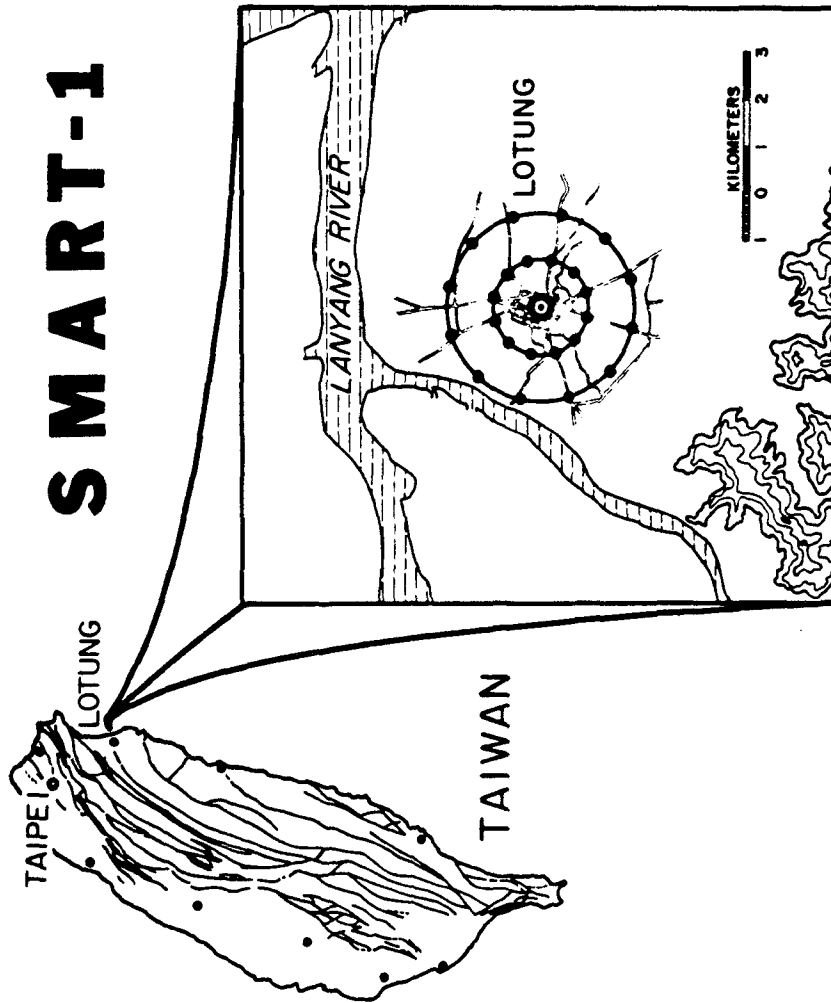
SMART-1

Figure 2.1 Location of the SMART 1 array.

SMART 1
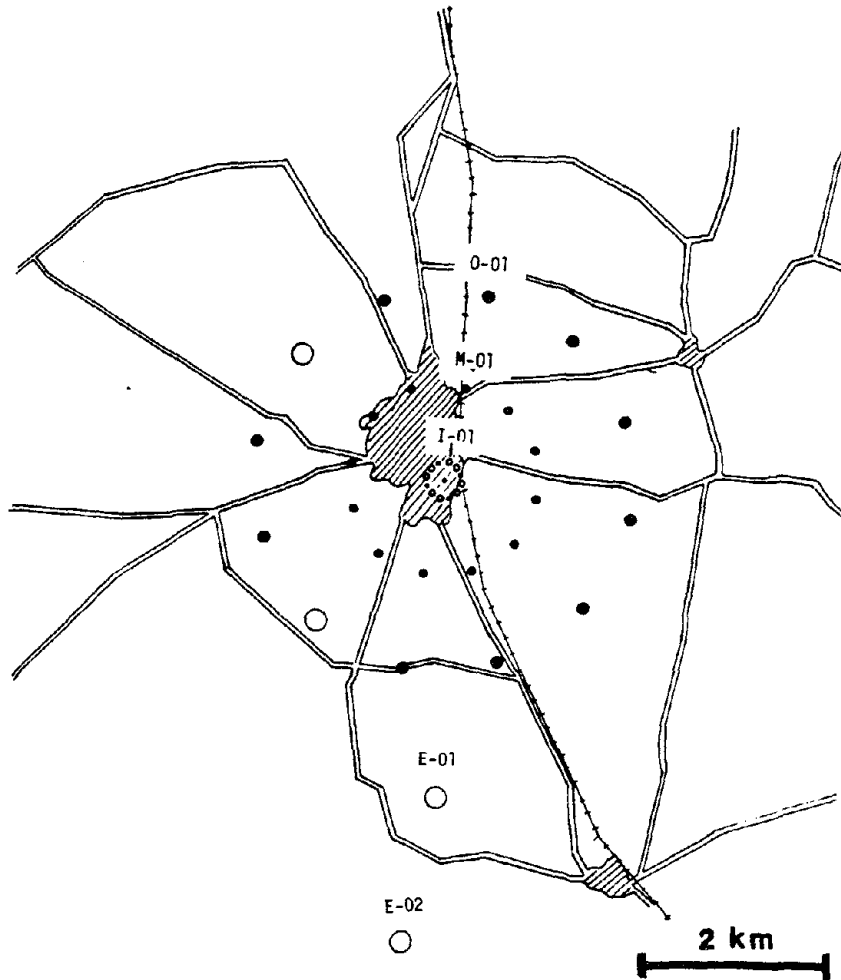
Figure 2.2 Geometry of the SMART array. The solid circles indicate stations that were installed during the Jan 29, 1981 event. The open circles indicate stations were installed after Jan 29, 1981. Stations in the three concentric circles are numbered 1 through 12 in a clockwise manner.
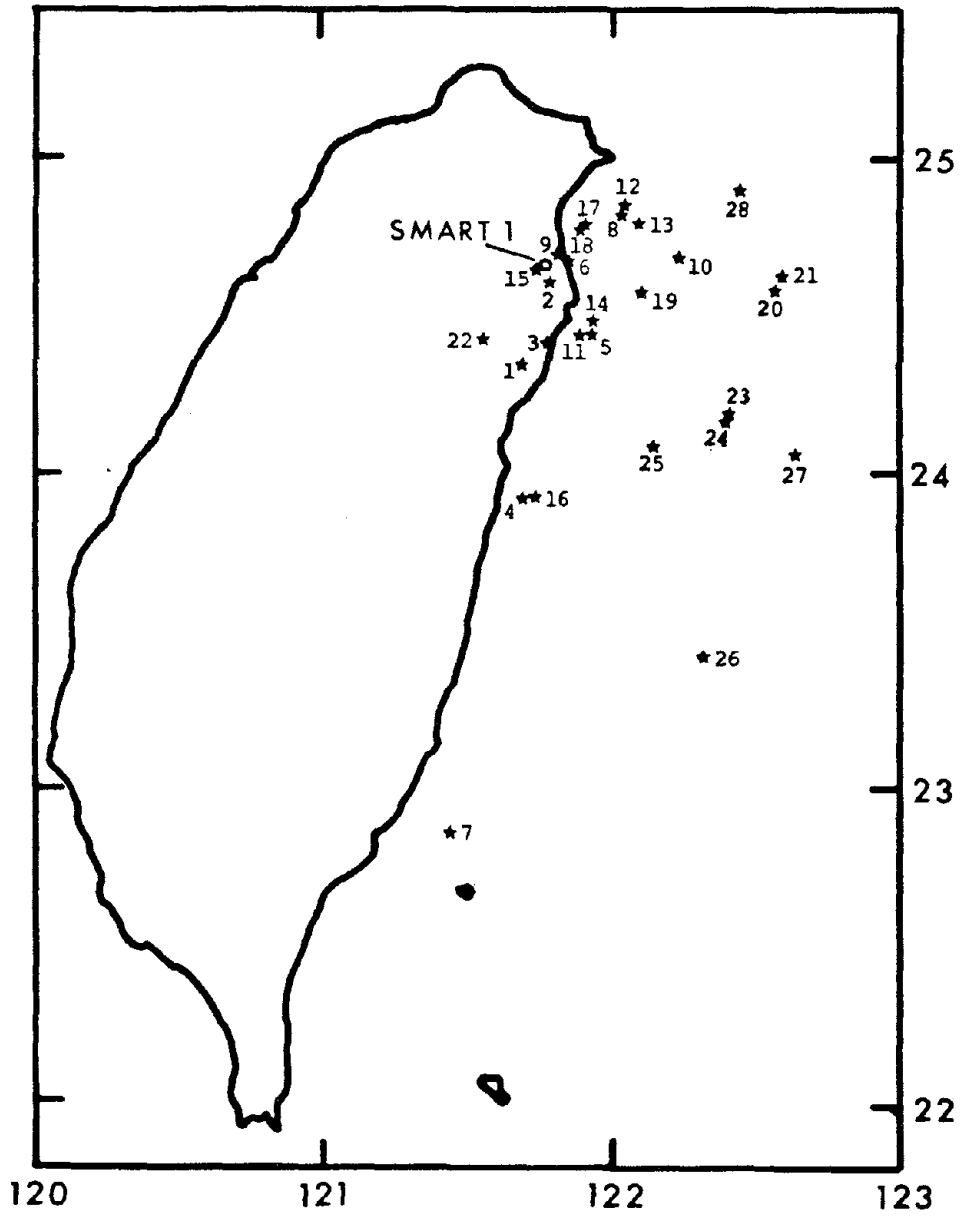
Figure 2.3 Epicenters of events recorded by the SMART 1 array.
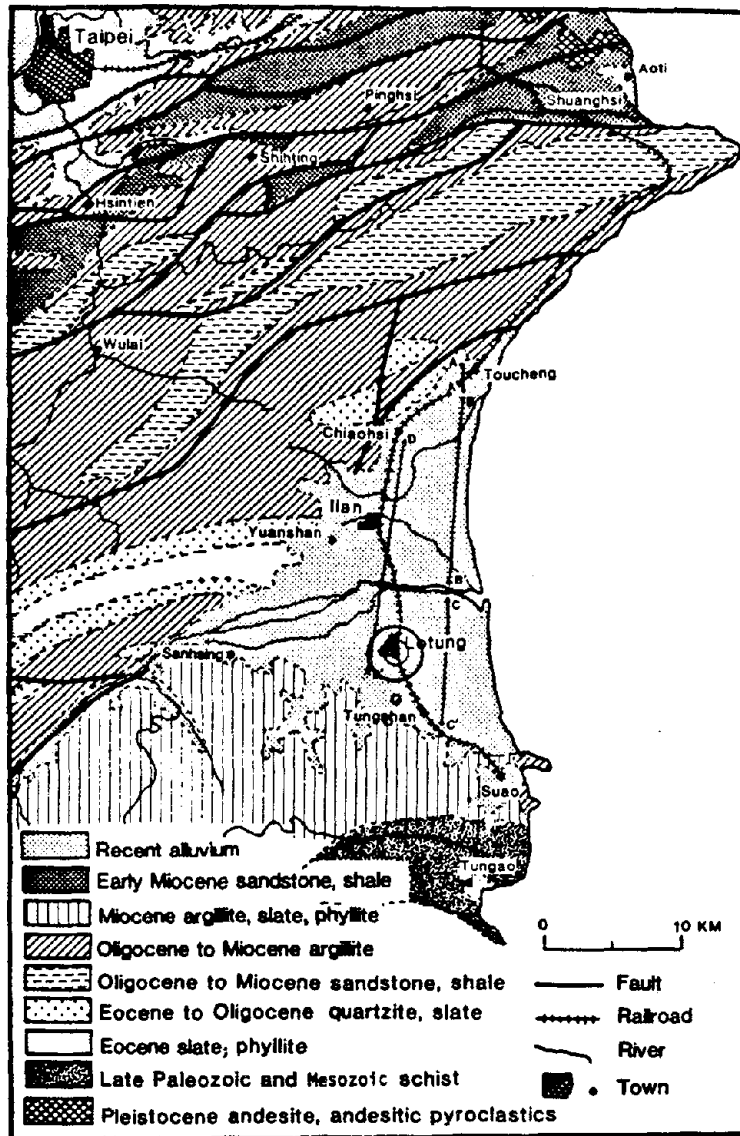
Figure 2.4 Geologic map of the Lan-yang Plain region. The location of the SMART 1 array is shown by the three concentric circles. The location of the extended array stations E-01 and E-02 are shown by the small circles near Tungshan. Cross-sections along lines A-C' and D-D' are shown in figure 2.5. (From Bolt *et al.*, 1982).

19

Subsurface geology along profile A-C'

Recent Alluvium
(500-1000m/sec)

Oligocene to Miocene
Argillite, Sandstone

Eocene Slate
(3300 m/sec)

Miocene Argillite
Slate

scale

0   2 km

Subsurface geology along profile D-D'

Recent Alluvium
(500-1000 m/sec)

Eocene to Oligocene Sandstone

Oligocene to Miocene
Argillite, Sandstone

Eocene to Oligocene
Sandstone

Miocene Argillite, Slate
(3300 m/sec)

Eocene Slate (3300)

scale

0   2 km
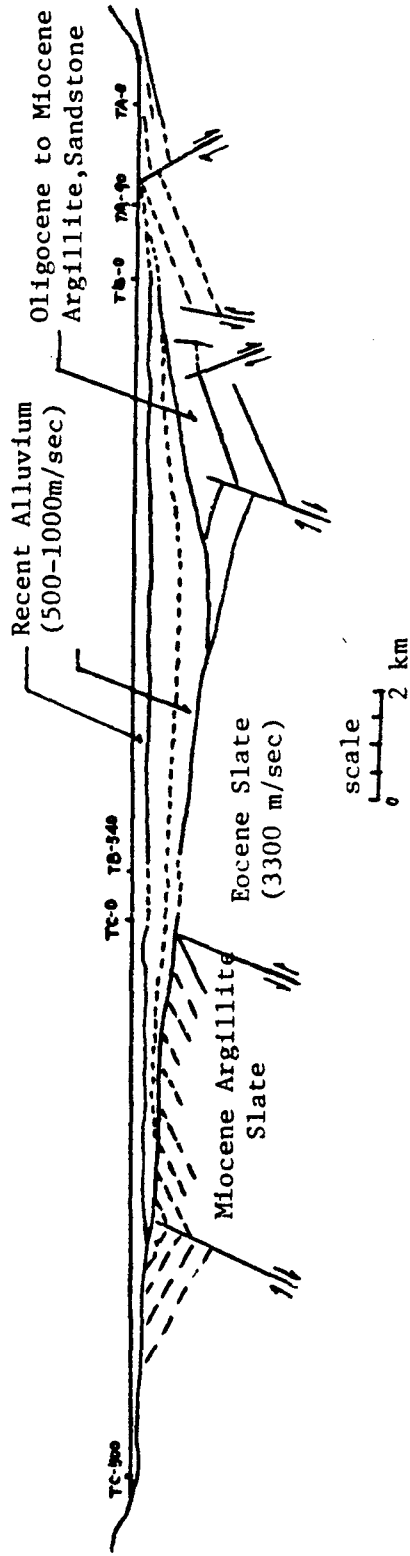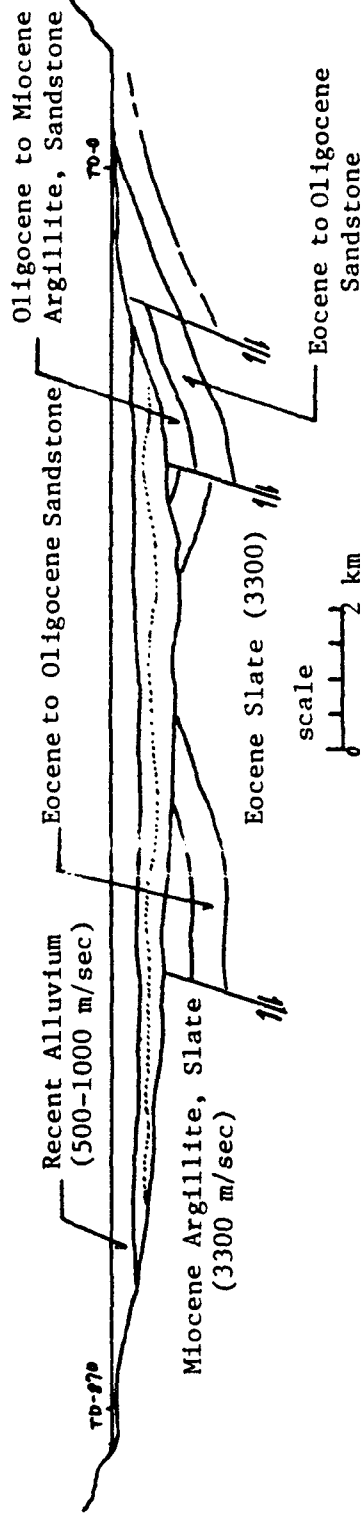
Figure 2.5 Cross-sections of the Lan-yang Plain along lines A-C' and D-D' in figure 2.4. The vertical exaggeration is 1:1. (From Bolt *et al.*, 1982).

20
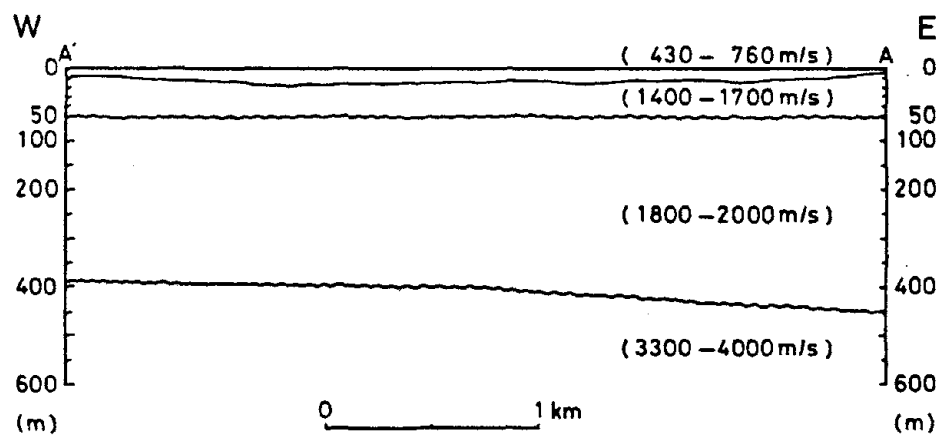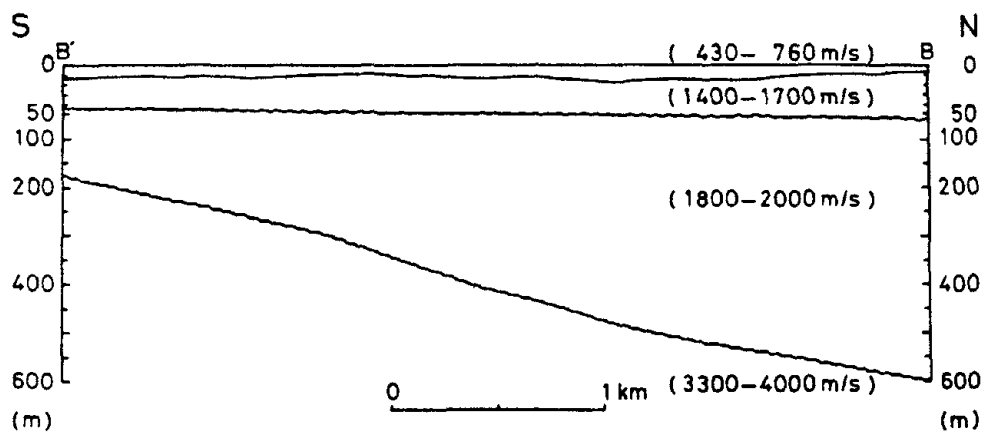
Figure 2.6 P wave velocities below the SMART 1 array. (From Wen and Yeh, 1983).
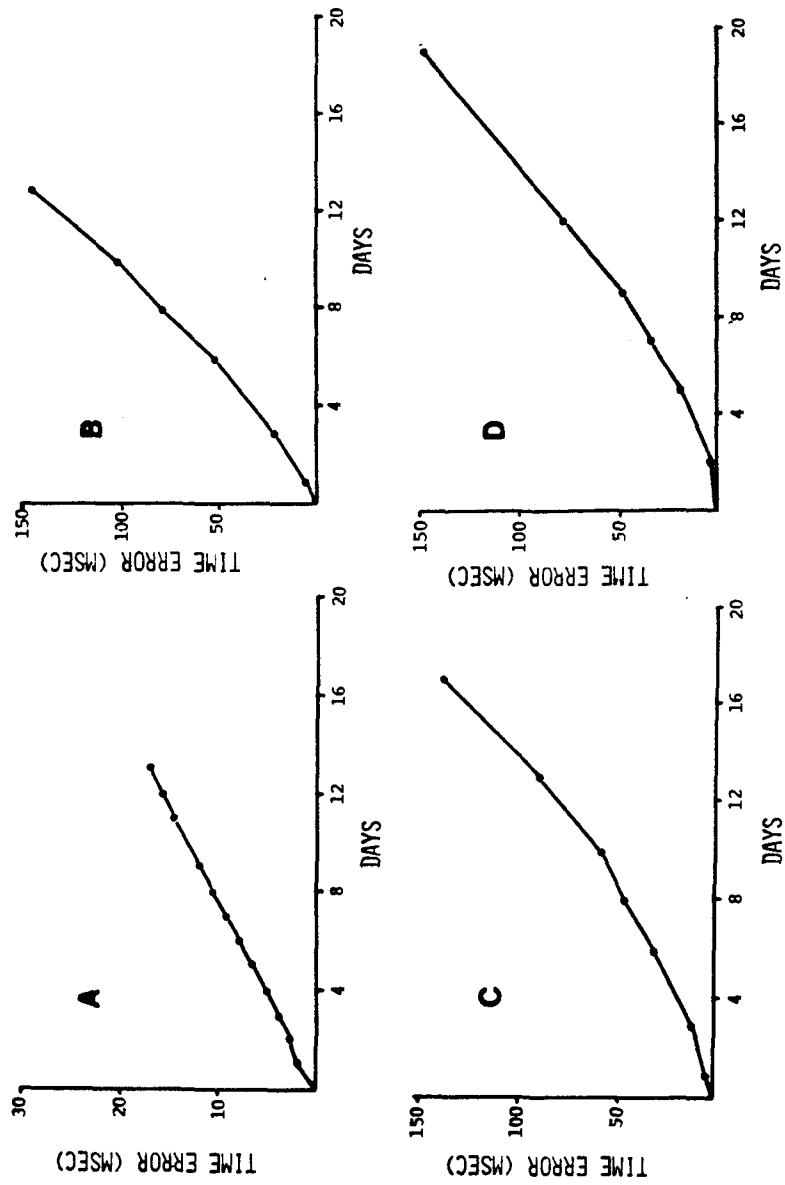
Figure 2.7 Typical clock drifts measured on four digital recorders. (From Liu, 1981).
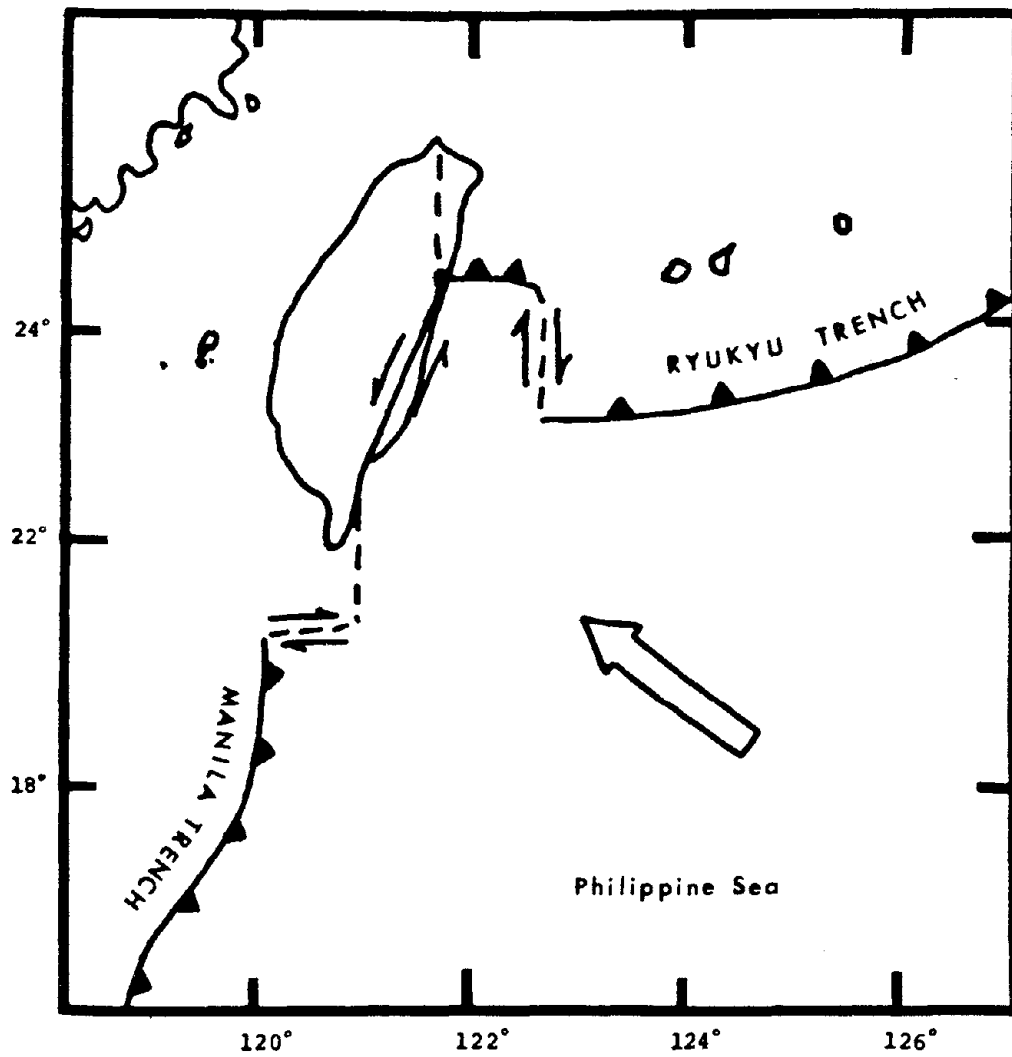
Figure 2.8 Simplified tectonics of the Taiwan region. The open arrow shows the direction of motion of the Philippine Sea plate.
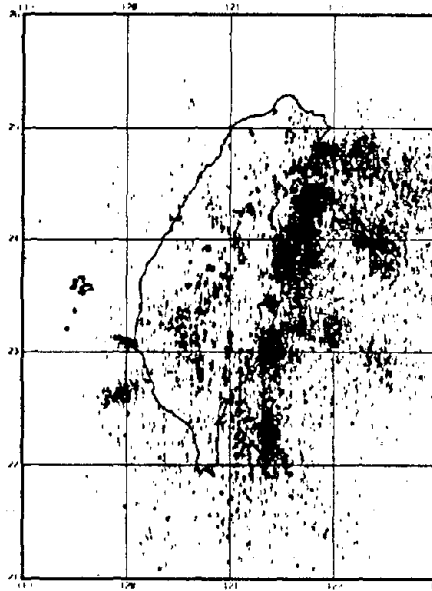
Figure 2.9 Epicenters $(M_D \geqslant 3.0)$ in Taiwan during 1973-1983. (From the Institute of Earth Sciences, Academia Sinica, Republic of China).
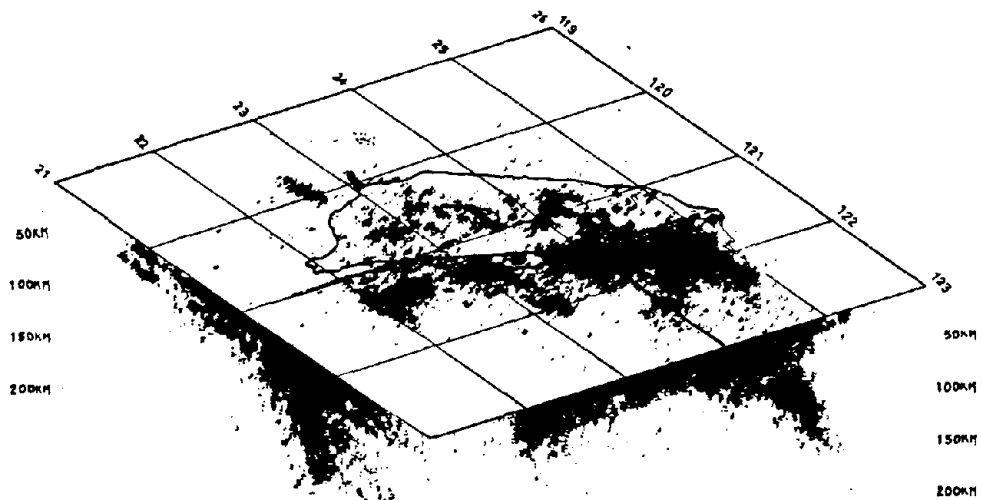
Figure 2.10 Stereographic projection of hypocenters $(M_D \geqslant 3.0)$ in Taiwan during 1973-1980. (From the Institute of Earth Sciences, Academia Sinica, Republic of China).

Chapter 3

The January 29, 1981 Taiwan Earthquake

3.1 Introduction

On January 29, 1981 at 04:51 (UTC) a large earthquake occurred off the northeastern coast of Taiwan. This event was felt throughout Taiwan with a maximum intensity of IV on the JMA[1] scale and triggered all 27 strong motion recorders in the SMART 1 array located 30 km NNW of the epicenter. The peak acceleration of 0.24 g is the largest acceleration recorded by the array during its first four years of operation.

The local magnitude is estimated from synthetic Wood-Anderson records calculated using the SMART 1 accelerograms (Kanamori and Jennings, 1978) and from a magnification 14 Wood-Anderson seismogram recorded at Taipei (Δ=75 km). The mean M_L determined from the array recordings is estimated at M_L=6.24 ± 0.08 by Bolt *et al.* (1982), however, they assume the Southern California attenuation curve (Richter, 1958). Richter's attenuation curve does not apply well to Taiwan as pointed out by Yeh *et al.* (1982). At an epicentral distance of 30 km, the Yeh *et al.* study gives $-\log A_o$=2.32 compared to $-\log A_o$=2.1 for Southern California. The corrected local magnitude estimate from the array recordings becomes M_L=6.46 ± 0.08. The Taipei 14x Wood-Anderson recording has a maximum trace amplitude of 52 millimeters (Figure 3.1). Applying the Taiwan attenuation curve yields

---

[1] The JMA intensity scale is defined in the *Seismological Bulletin of the Japan Meteorological Agency.* Intensity IV is given as "Strong: strong shaking of houses and buildings. Overturning of gravestones, stone lanterns, etc. Damage to chimneys and mud-and-plaster warehouses."

M_L=6.85. The mean of these two magnitude estimates is M_L=6.7.

3.2 Aftershocks and Direction of Rupture

During the two week period following the mainshock, 20 aftershocks with $M_D \geqslant 2.5$† were recorded by the TTSN.[2] These seismograms along with the mainshock recordings were read for P and S arrival times and for P wave polarities and then located using a linear gradient over a halfspace velocity model (Ferguson *et al.*, 1980). The velocity model is determined by simultaneously minimizing the residuals of four aftershocks that have at least 5 P and 5 S high quality readings each (events 8, 14, 16 and 17 listed in table 3.2). The resulting velocity model is shown in figure 3.2. There are difficulties in locating the events because they occurred offshore (figure 3.4), restricting the azimuthal coverage of the local network to approximately 160° (figure 3.3). The use of both P and S readings helps to constrain the solutions, although there remains a large covariance between origin time and longitude. A typical covariance matrix is given below.

TABLE 3.1 Covariance Matrix

	O.T.	Lat.	Long.	Dep
Origin Time	1.0	0.26	0.85	-0.63
Latitude	0.26	1.0	0.49	-0.01
Longitude	0.85	0.49	1.0	-0.44
Depth	-0.63	-0.01	-0.44	1.0

The longitude of the mainshock epicenter is estimated at 121.92°E±0.035° and agrees well with the ISC location of 121.88°E±0.015° which is based on teleseismic recordings. This indicates that the longitude estimates calculated using the velocity model shown in figure 3.2 are reliable for events in the same region as the mainshock.

The epicenters of the mainshock and 20 aftershocks are shown in figure 3.4. Note that

---

† Taiwan duration magnitude is defined in Liaw and Tsai (1981). Duration magnitude has been correlated with local magnitude by Yeh et al. (1982).
They find $M_L = 1.10 + 0.93 M_D \pm 0.30$

[2] The Taiwan Telemetered Seismic Network (TTSN) consists of 24 short period vertical seismometers and 2 short period horizontal seismometers. The data are telemetered to Taipei where they are analyzed at the IES.

all of the aftershocks lie west of the mainshock, suggesting unilateral rupture from east to west. The aftershocks are listed in table 3.2 and the north-south and east-west depth sections are shown in figures 3.5a-b. The latitude is the best determined hypocenter parameter because there is wide north-south coverage. The standard errors in the latitudes are between 0.4 and 1.1 km while the standard errors in the longitudes are approximately three times as large being between 1.4 and 3.9 km. The uncertainty in the depth estimates are approximately as large as the uncertainties in the longitude estimates.

The least-squares fit plane constrained to pass through the mainshock hypocenter strikes N108°E ± 5° with a dip of 53° ± 8°. The rupture appears to have progressed up the dipping plane based on the decrease in depth of the aftershocks from east to west.

3.3 Focal Mechanisms

The first motion data of the mainshock and aftershocks were read from the short period vertical seismometers in the TTSN. The focal mechanism of the mainshock cannot be uniquely determined using the regional first motion data alone because of limited coverage on the focal sphere (figure 3.6). To help constrain the focal mechanism, the first motion data from the aftershocks are included to form composite or group focal plane solutions.

A group focal mechanism algorithm developed by Brillinger *et al.* (1980) is used. The estimation of the group focal mechanism is highly non-linear causing the final solution to be strongly dependent on the initial solution. The first motion data from 19 of the 21 events in the earthquake sequence are plotted in figure 3.7. Events 15 and 20 are excluded because of the relatively large uncertainties in their focal parameters (see table 3.2). Two initial solutions consistent with the mainshock data are used in the group focal mechanism program.

Initial solution 1 is primarily strike-slip (figure 3.8a). Seven events including the mainshock are consistent with this mechanism; these are events 1, 2, 6, 11, 13, 18, and 19. The group focal plane solution is shown in figure 3.8b with 95% confidence intervals shown around the P and T axes.

27

Initial solution 2 is primarily reverse (figure 3.9a). Nine events including the mainshock are consistent with this mechanism; These are events 1, 4, 8, 9, 10, 12, 13, 16, and 21. The group focal plane solution is shown in figure 3.9b with 95% confidence intervals shown around the P and T axes. Solution 1 and 2 are possible mechanisms for the mainshock.

We can choose between these two solutions by checking for compatability with the teleseismic first motion data for the mainshock listed in the ISC catalog. These first motions data are plotted in figure 3.10. Near the center of the projection, the majority of the readings are compressional which disagrees with mechanism 1. Only 26% of the teleseismic readings agree with mechanism 1 while 70% of the readings agree with mechanism 2. For this reason, solution 2 is preferred.

Of the two possible fault planes given by solution 2, the plane striking N109E is preferred since it is consistent with the trend of the mainshock and aftershock epicenters. The preferred fault plane fault plane parameters are

Preferred Fault Plane

Strike	$108.8° ± 8.2°$
Dip	$60.7° ± 4.5°$
Slip	$64.3° ± 4.1°$

3.4 Array Recordings

At the time of the Jan. 29, 1981 event, 27 stations were installed in the array. Of the 81 records obtained, only one[3] failed to operate correctly. Absolute time was successfully recorded at all 27 stations.

The 80 usable records are shown in figures 3.11a-c and are aligned according to increasing epicentral distance and absolute time. Note the very coherent S pulse on the NS component which can be clearly seen across the whole array. The P and S wave windows used in chapters 5 and 6 are marked in each figure by the bracket above the time axis. The coherency

---

[3] The EW component of station M-11 failed.

of the P and S waves and their frequency dependence are discussed in chapter 5.

Figure 3.12 shows in more detail the three components of acceleration recorded at the central array station C-00. The baseline correction procedures are described in appendix B.

There are variations in the vertical and horizontal peak accelerations observed across the array of factors of 3.9 and 3.3 respectively. The peak vertical accelerations vary from 0.023 g at station O-05 to 0.090 g at station M-01. The peak horizontal accelerations vary from 0.072 g at station M-09 to 0.240 g at station O-02. The ratio of peak horizontal acceleration to peak vertical acceleration varies from 1.8 to 6.3 across the array. These large variations over distances of less than 4 km accentuate the difficulty with describing an accelerogram simply by its peak value.

TABLE 3.2 Event 5 Aftershock Sequence

No.	Origin Time (UTC)		σ (sec)	M_L	Latitude (North)	σ (km)	Longitude (East)	σ (km)	Depth (km)	σ (km)
1	Jan 29	04:51:34.5	0.48	6.7	24°26.20'	1.1	121°54.92'	3.5	25.2	1.8
2	Jan 29	04:57:04.1	0.31	3.5	24°27.66'	0.8	121°51.79'	2.2	14.6	2.5
3	Jan 29	04:59:42.4	0.30	3.5	24°27.04'	0.8	121°51.63'	2.2	15.9	2.7
4	Jan 29	05:01:37.3	0.37	3.4	24°27.39'	0.6	121°51.58'	2.0	17.3	1.6
5	Jan 29	05:04:17.9	0.21	3.4	24°27.38'	0.5	121°49.31'	1.2	18.1	1.4
6	Jan 29	05:29:48.5	0.18	3.4	24°27.74'	0.3	121°49.74'	0.8	13.1	1.5
7	Jan 29	07:48:26.6	0.25	3.4	24°28.57'	0.6	121°46.78'	1.6	8.4	3.4
8	Jan 29	19:19:20.4	0.42	4.3	24°28.22'	1.0	121°49.98'	3.9	20.7	3.0
9	Jan 29	19:35:40.3	0.34	3.8	24°29.91'	0.8	121°48.59'	2.7	15.9	2.9
10	Jan 30	02:50:56.4	0.33	3.5	24°28.59'	0.8	121°48.66'	2.1	12.5	3.0
11	Jan 30	20:18:55.8	0.29	3.8	24°27.14'	0.6	121°52.51'	1.7	19.9	2.1
12	Feb 01	03:27:07.4	0.23	3.5	24°26.45'	0.7	121°49.94'	1.8	9.1	2.9
13	Feb 01	12:00:14.4	0.36	3.5	24°28.80'	0.5	121°51.24'	2.2	13.6	1.3
14	Feb 01	21:12:00.7	0.28	4.1	24°25.24'	1.0	121°53.56'	2.2	23.7	1.9
15	Feb 02	01:08:00.8	0.57	3.4	24°25.60'	1.4	121°51.16'	6.8	6.0	22.3
16	Feb 02	10:42:02.4	0.14	3.7	24°25.07'	0.7	121°52.05'	1.6	24.6	1.1
17	Feb 03	00:15:42.1	0.24	3.4	24°28.80'	0.8	121°49.97'	1.6	17.8	1.5
18	Feb 03	20:58:04.9	0.30	4.0	24°24.82'	0.7	121°51.48'	1.4	15.2	2.0
19	Feb 10	22:32:34.9	0.34	3.5	24°24.62'	0.8	121°50.21'	2.1	13.9	2.1
20	Feb 12	11:02:38.1	0.66	3.4	24°28.62'	1.9	121°48.72'	4.4	18.1	5.7
21	Feb 14	19:13:02.2	0.20	3.7	24°25.60'	0.4	121°51.92'	1.2	19.7	1.0
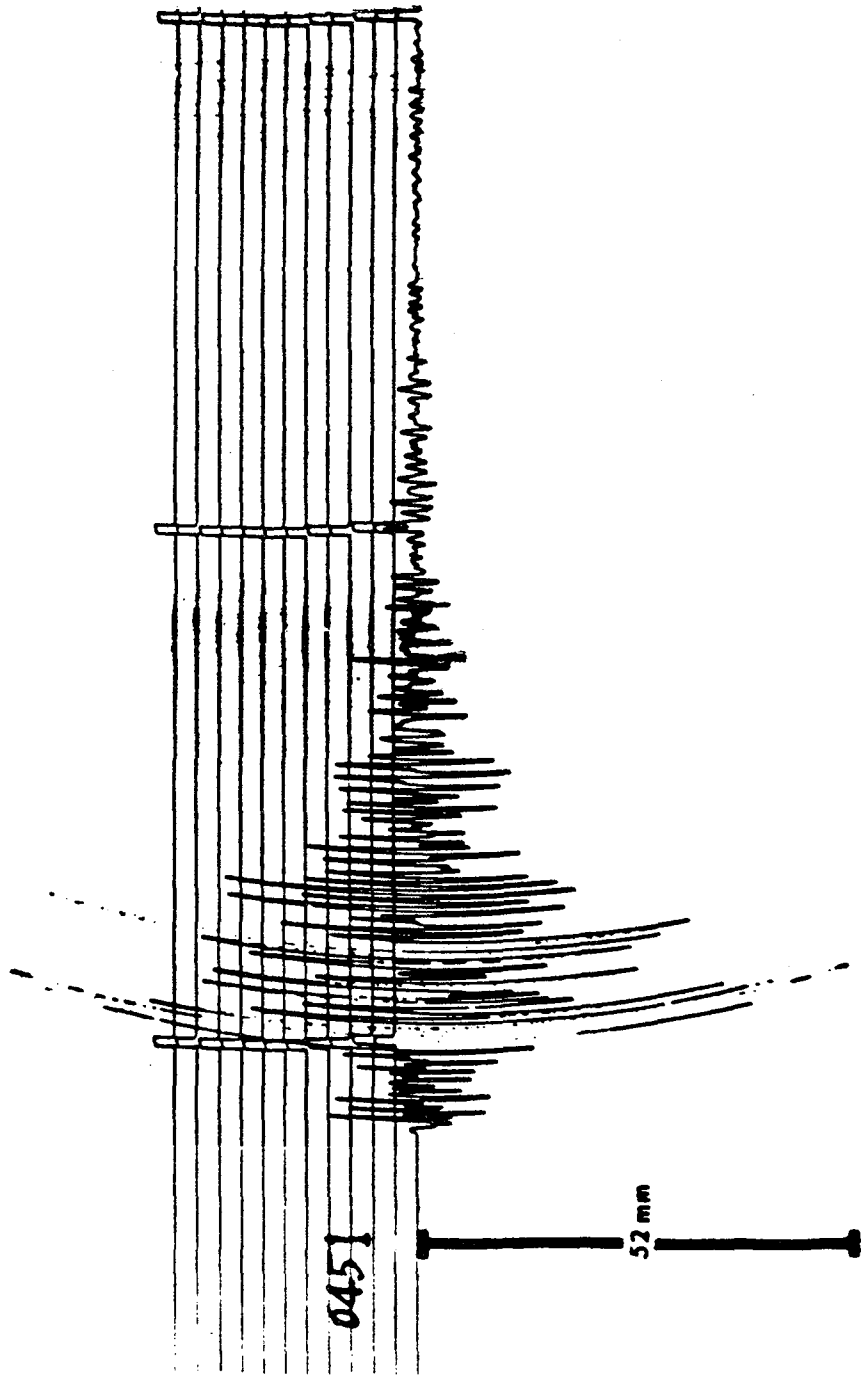
Figure 3.1 14x Wood-Anderson seismogram recorded at Taipei (Δ = 75 km). The maximum trace amplitude is 52 mm.
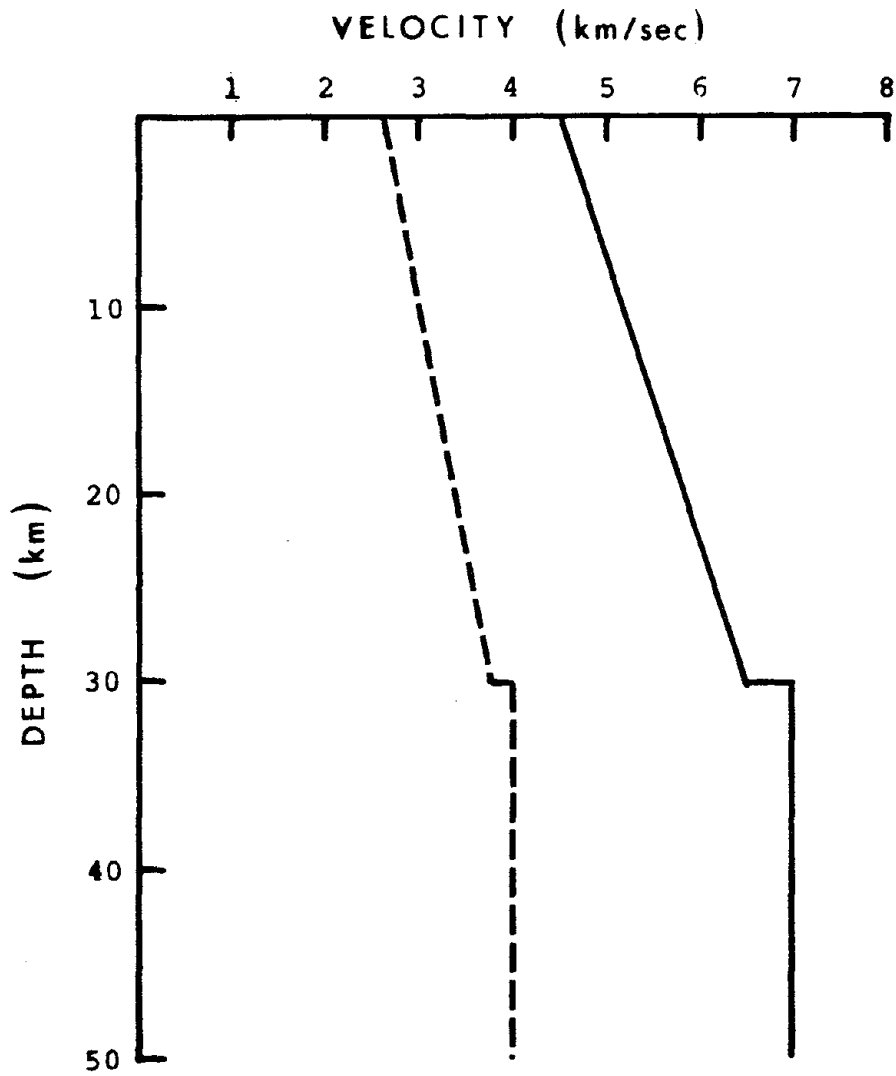
Figure 3.2 Velocity model used for locating the mainshock and the aftershocks.
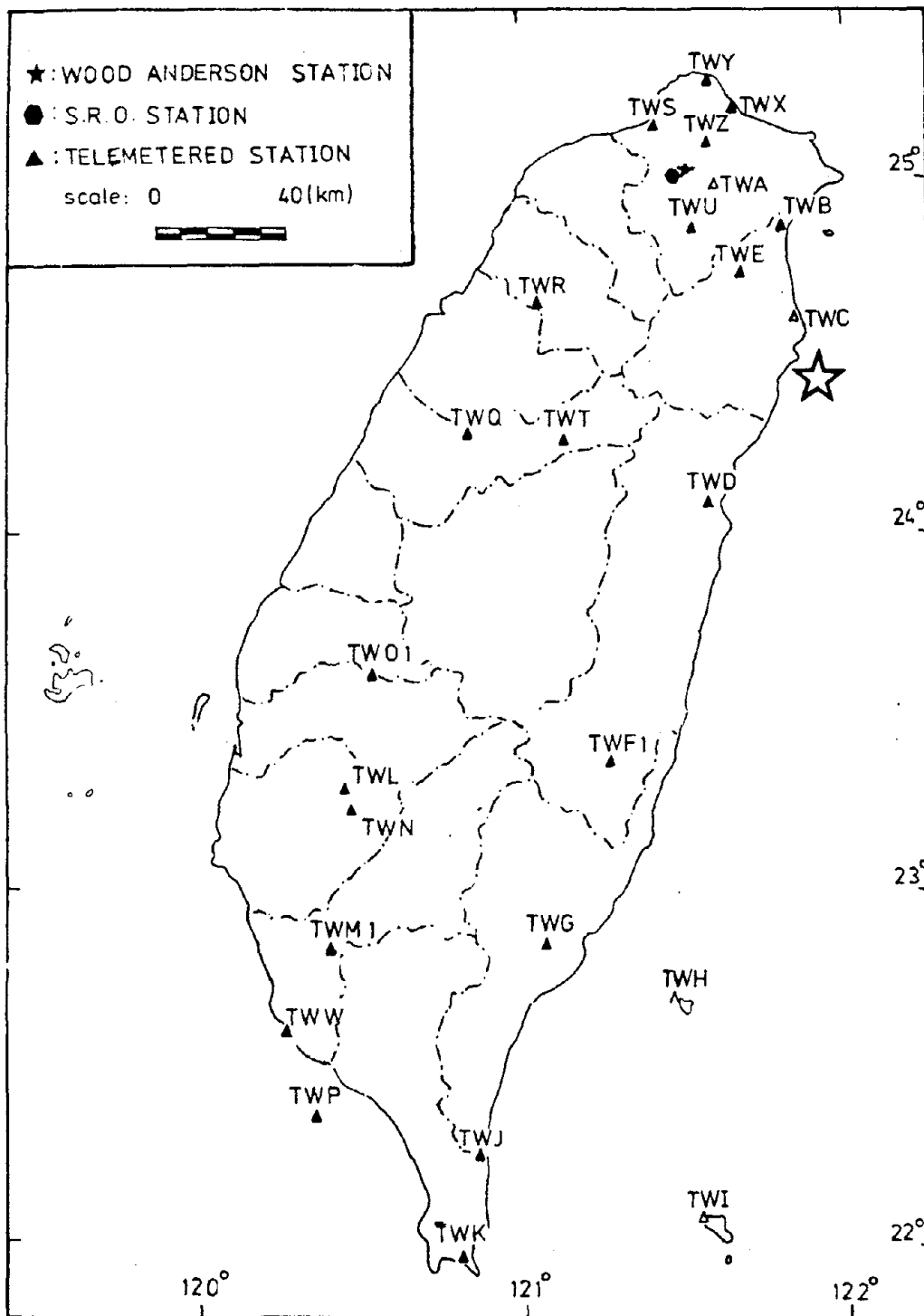
Figure 3.3 Stations of the Taiwan Telemetered Seismic Network. (From Institute of Earth Sciences, Academia Sinica). The open star indicates the location of the January, 29, 1981 epicenter.

33
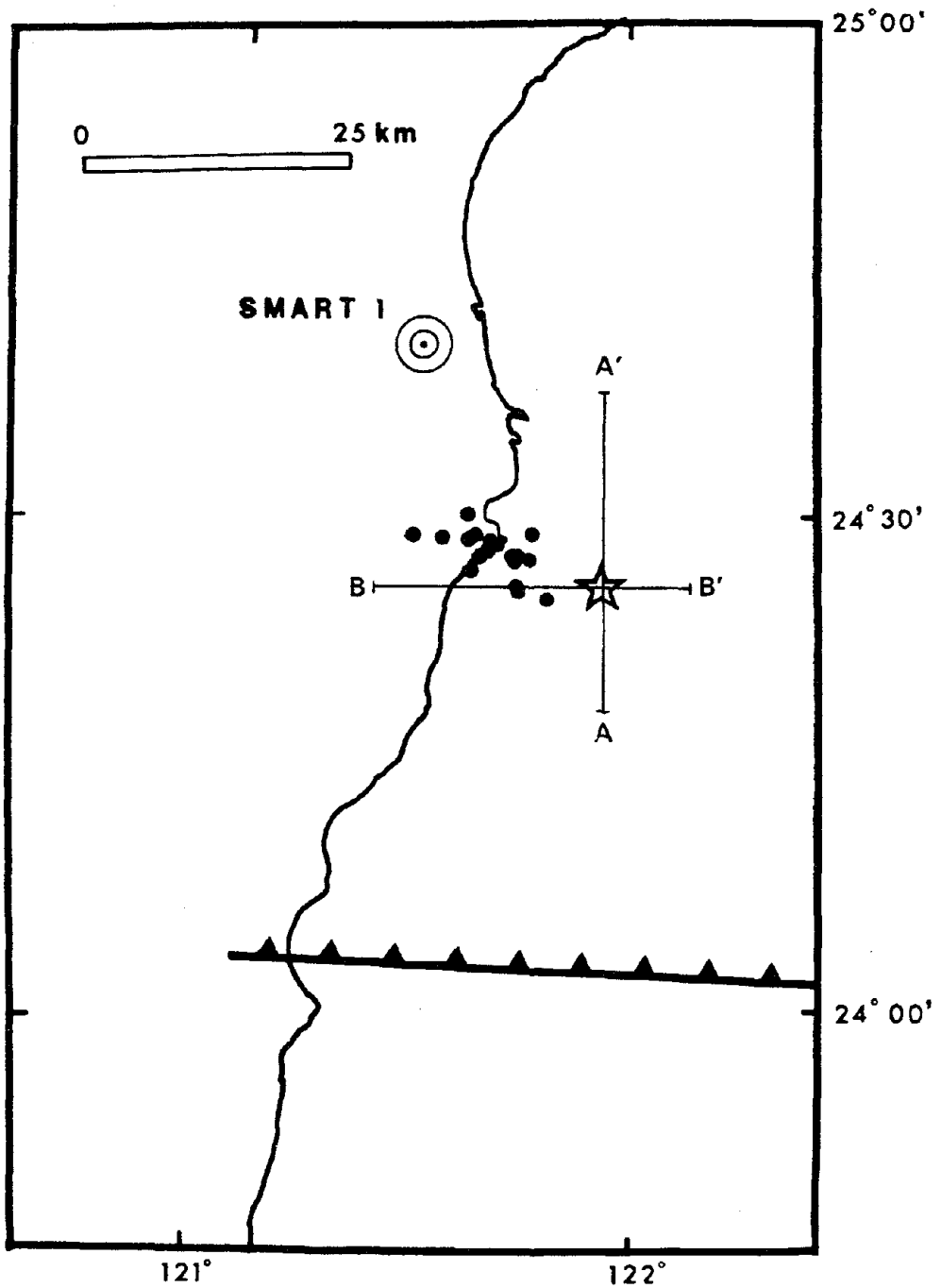
Figure 3.4 The epicenters of the January 29, 1981 sequence during the two week period following the mainshock. The mainshock is shown by the star. The distribution of aftershocks suggests unilateral rupture from east to west.
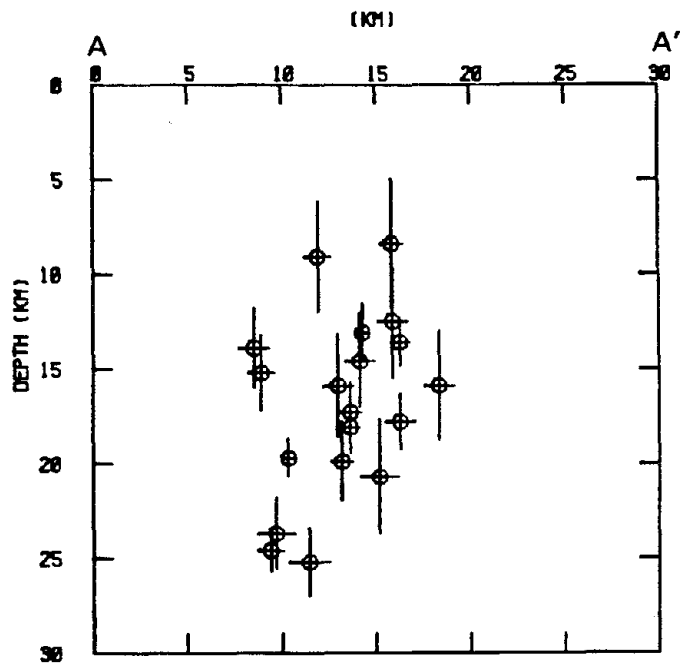
Figure 3.5 (a) Hypocenters of the event 5 sequence projected on a North-South cross section. The vertical and horizontal lines indicate ±1σ.
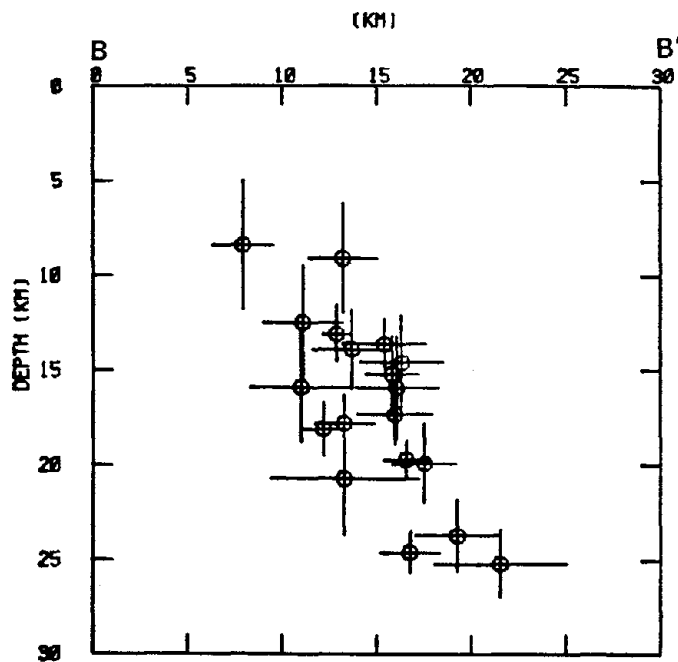
Figure 3.5 (b) Hypocenters of the event 5 sequence projected on an East-West cross section. The vertical and horizontal lines indicate ±1σ.
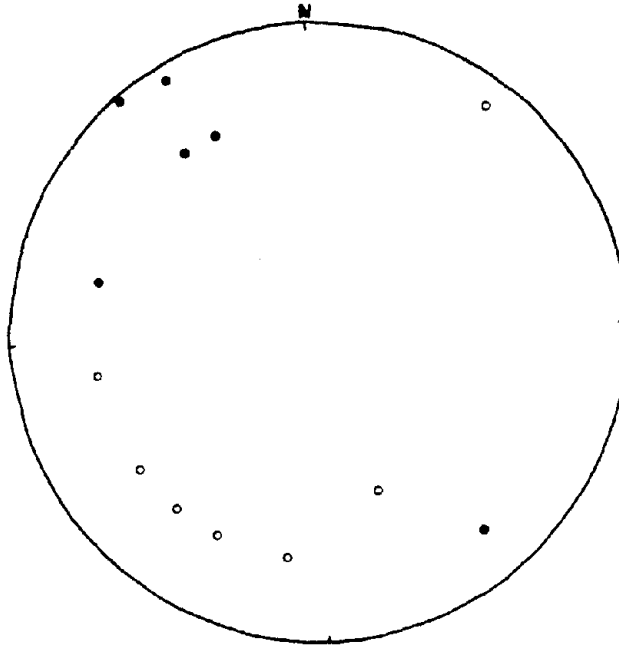
Figure 3.6 Regional first motion data from the mainshock. Solid circles represent compressions and open circles represent dilations.
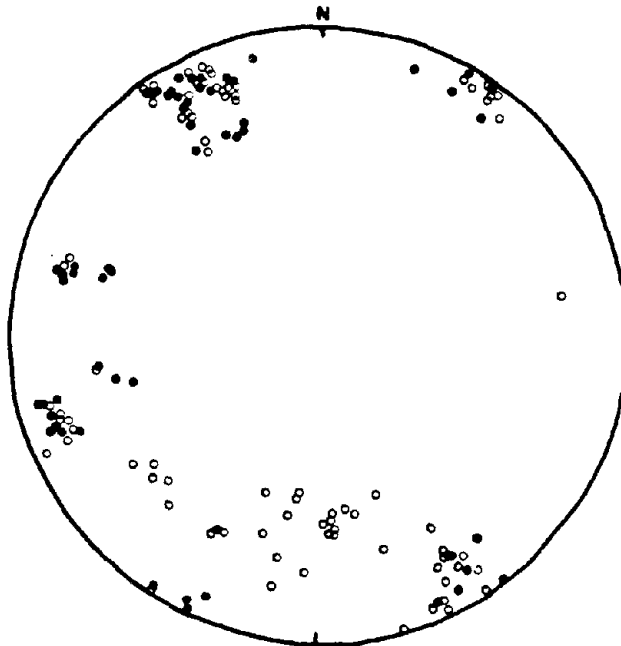
Figure 3.7 Regional first motion data from 19 events in the earthquake sequence.

36
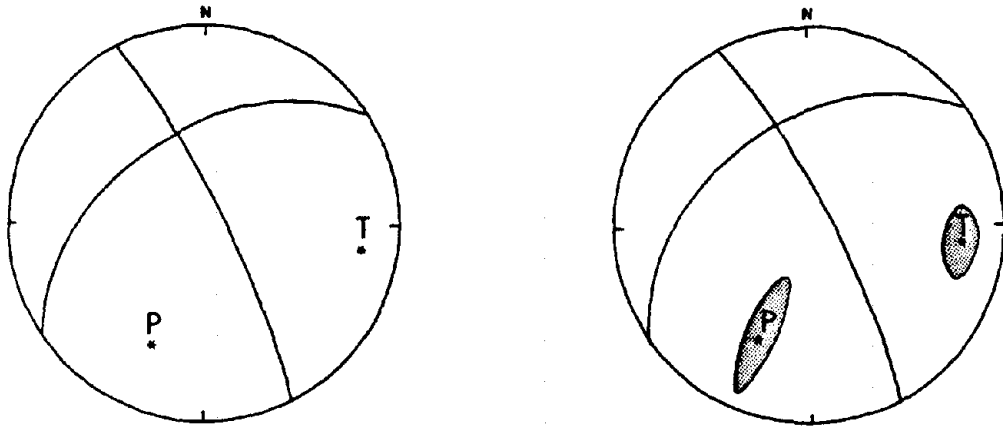
Figure 3.8(a) Initial solution 1 (left) and (b) Final solution 1 (right) of the group focal mechanism. The shaded region around the P and T axes are the 95% confidence intervals.
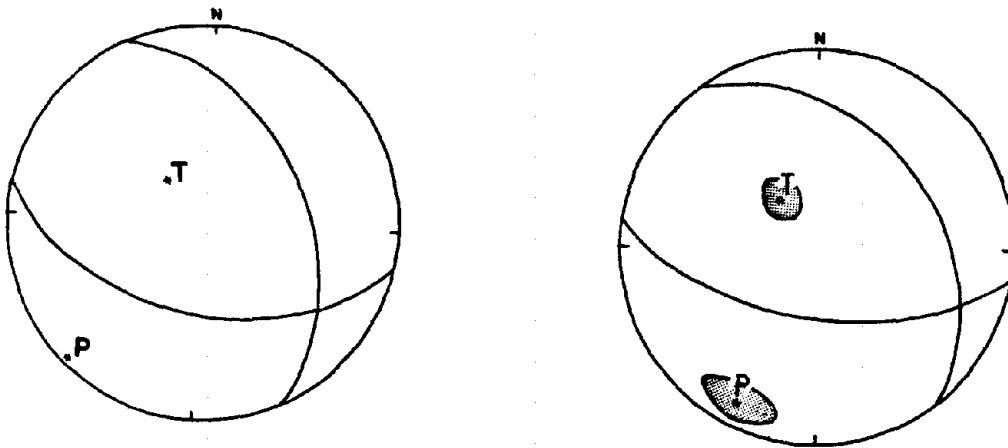
Figure 3.9(a) Initial solution 2 (left) and (b) Final solution 2 (right) of the group focal mechanism. The shaded region around the P and T axes are the 95% confidence intervals.
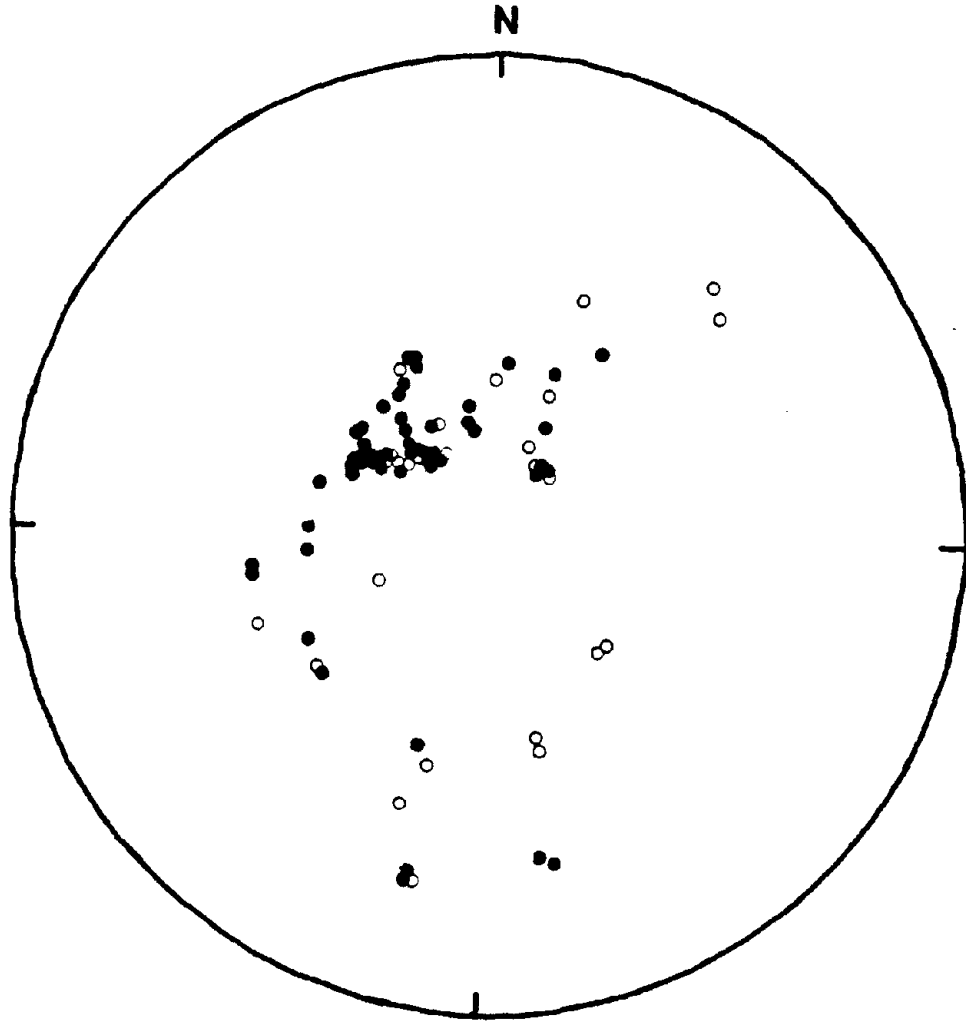
Figure 3.10 Teleseismic first motion data from the ISC catalog.
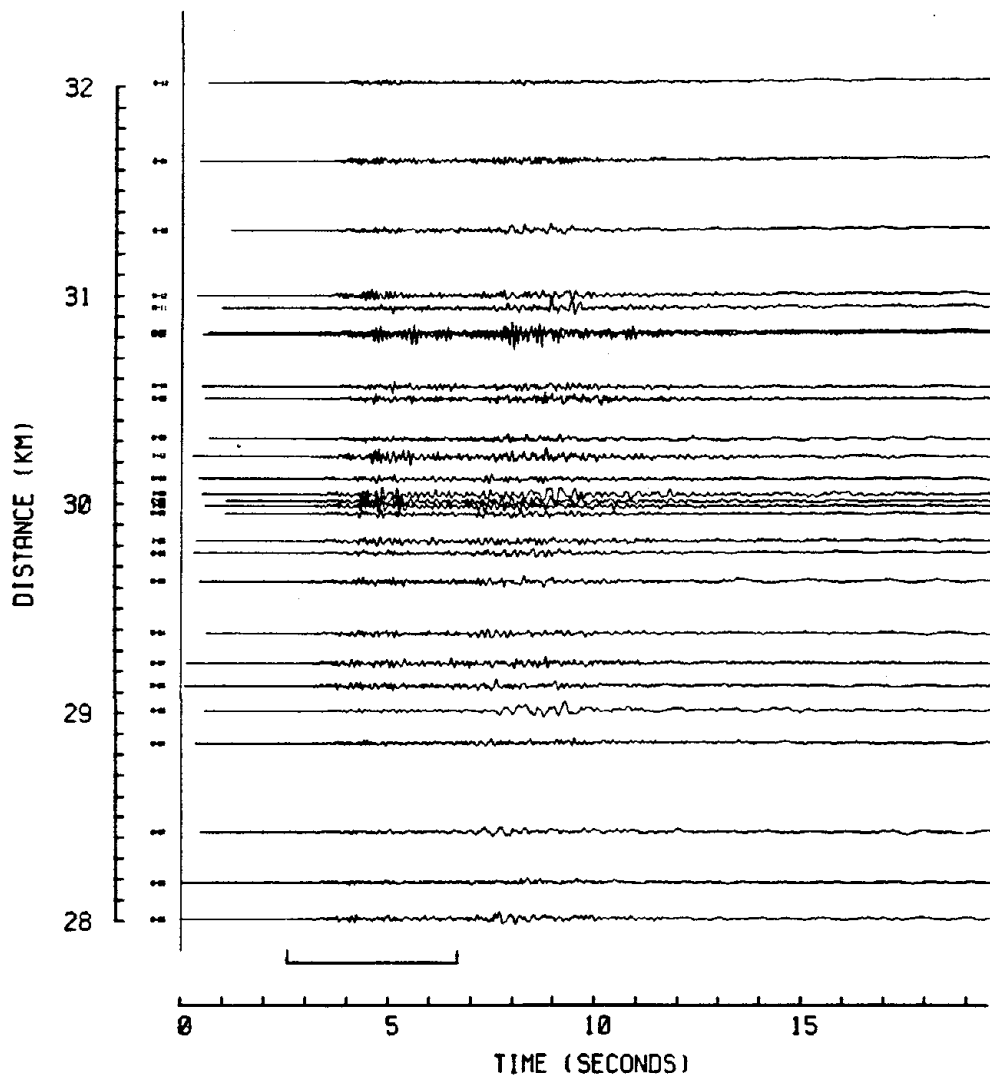
Figure 3.11(a) Vertical component accelerograms recorded at the array during the January 29, 1981 event. The records are aligned on absolute time and are plotted according to increasing epicentral distance.
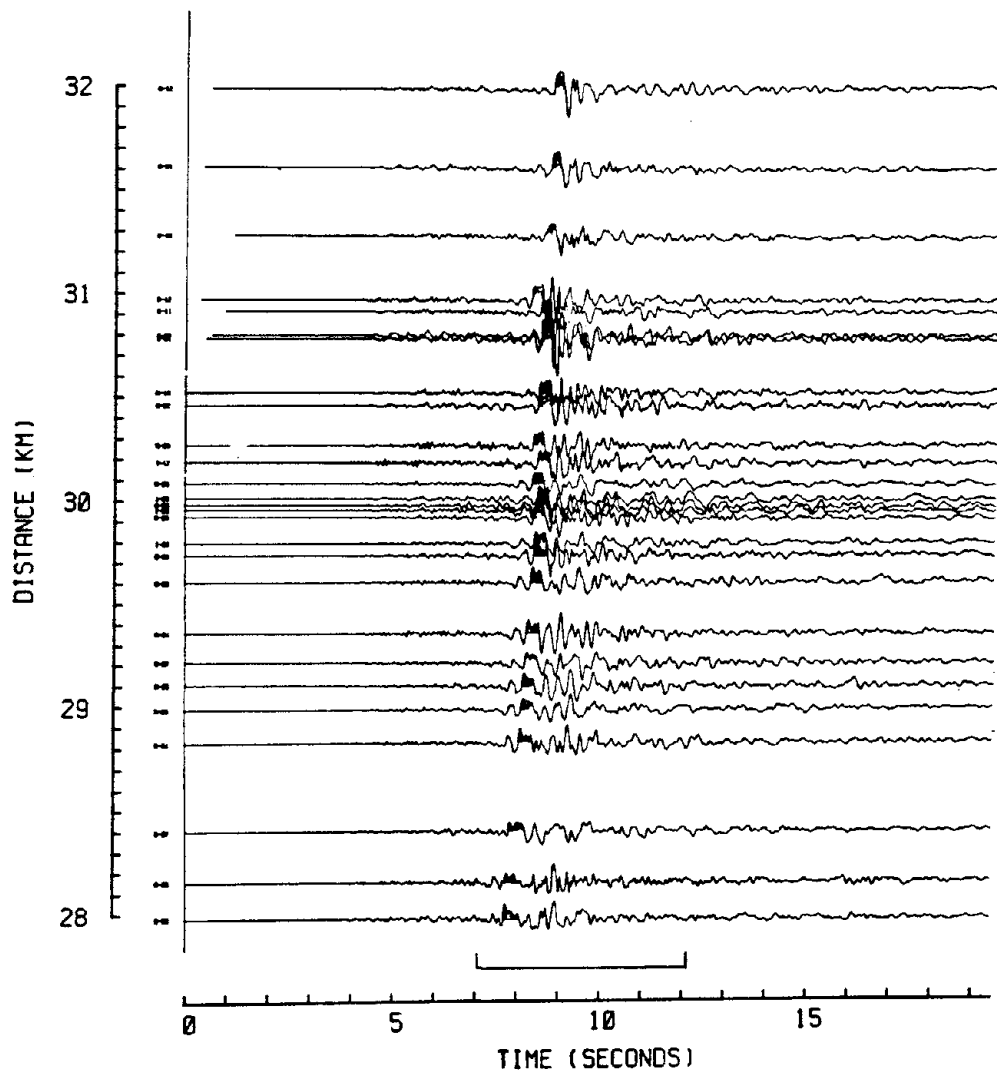
Figure 3.11(b) North-South component accelerograms recorded at the array during the January 29, 1981 event. The records are aligned on absolute time and are plotted according to increasing epicentral distance.

40
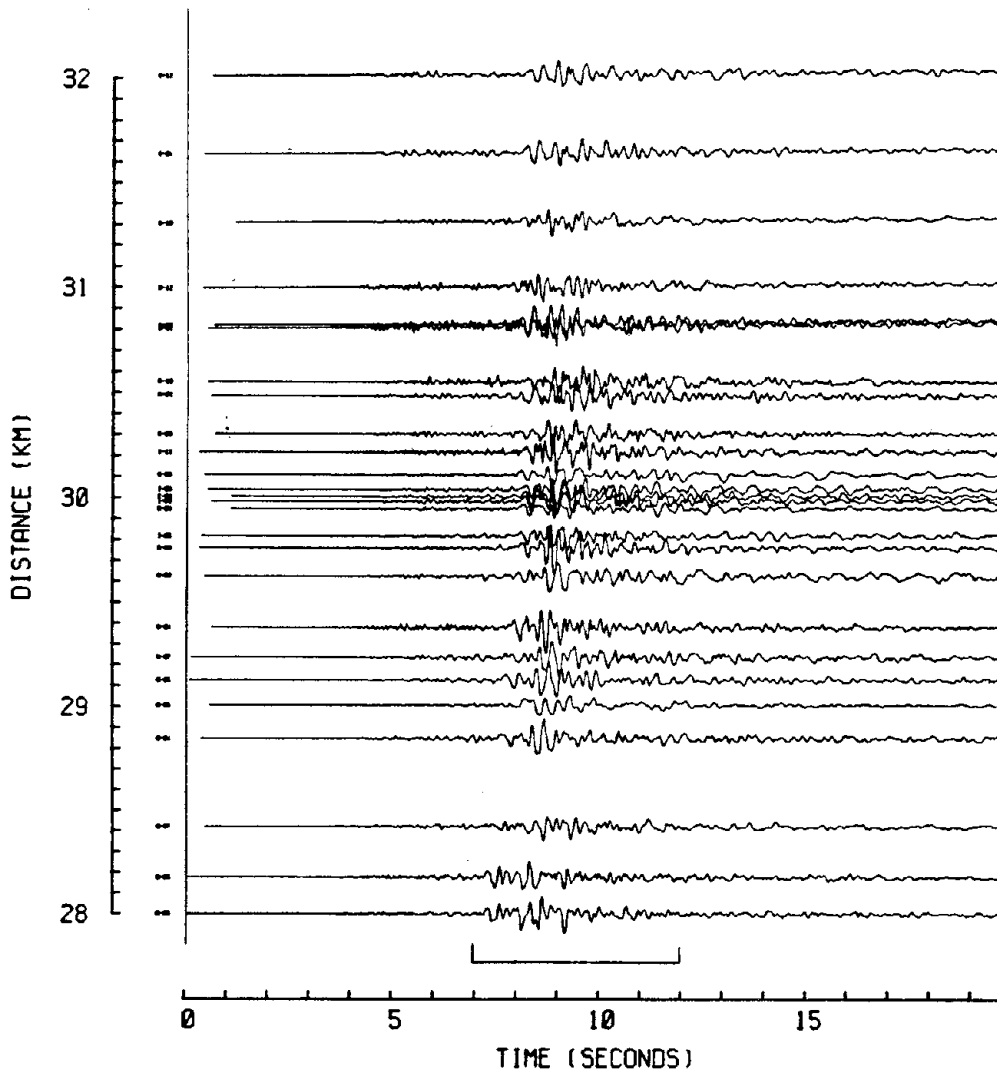
Figure 3.11(c) East-West component accelerograms recorded at the array during the January 29, 1981 event. The records are aligned on absolute time and are plotted according to increasing epicentral distance.

41
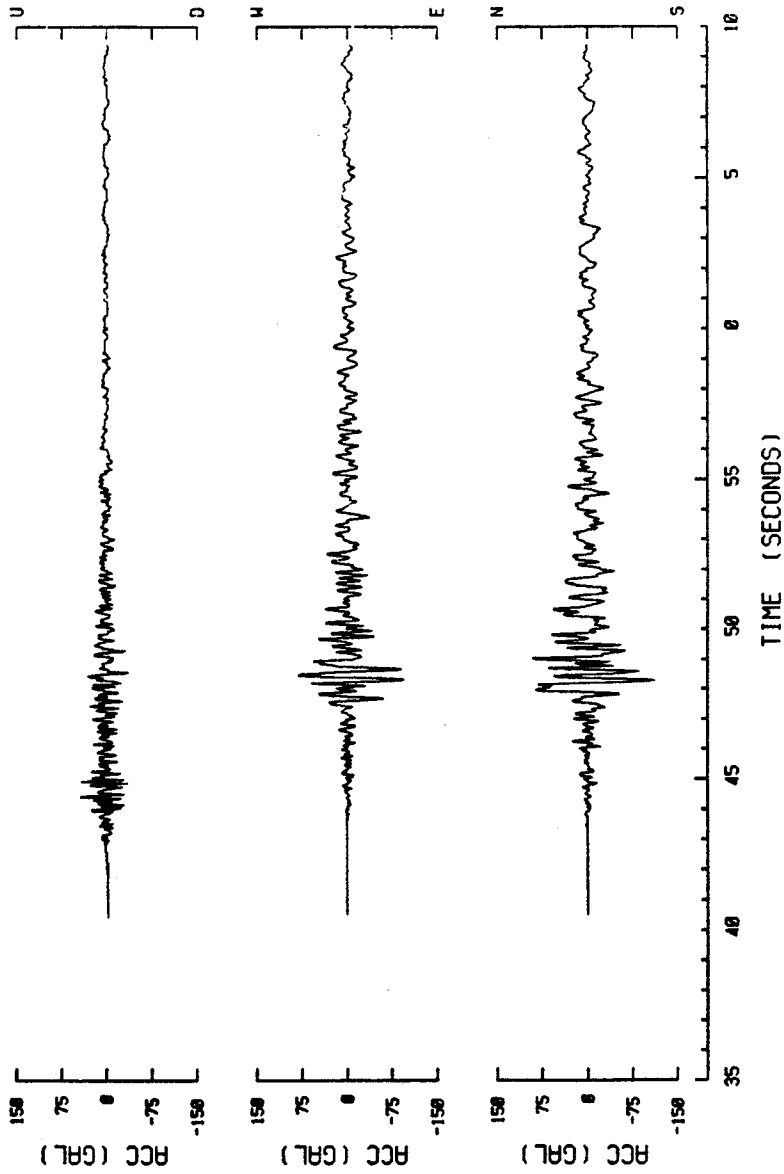
Figure 3.12 The three components of acceleration recorded at station C-00.

Chapter 4

Array Analysis

4.1 Introduction

Some of the advantages of array recordings over single station recordings are that they can be used to improve the signal-to-noise ratio, correlate waveforms, measure the coherency of the waves and measure the azimuth and velocity of coherent waves as they propagate across the array. The wave coherency is examined in chapter 5 and the time dependent wave azimuth will be used to study the details of the rupture process in chapter 6. In general, array analysis can be expressed as filtering followed by a summation as shown in figure 4.1.
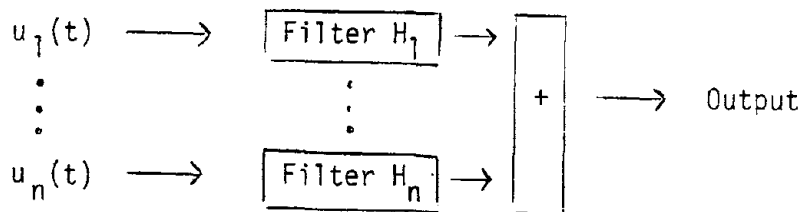
Figure 4.1 General linear array processing

A standard assumption in array analysis is that the recorded signal consists of a deterministic signal plus noise. For example

$$u_j(t) = s(t) + \epsilon_j(t) \qquad j=1,2,...N \qquad (4.1.1)$$

where $s(t) = t^{th}$ *time sample of the signal*,

$\epsilon_j(t) = t^{th}$ *time sample of the noise at station j*,

and $u_j(t) = t^{th}$ *time sample of the output at station j*.

In matrix notation this becomes $\vec{u}(t) = s(t)\vec{\zeta} + \vec{\epsilon}(t)$ where $\vec{\zeta} = \text{col } [1,1,...1]$. Note that this form assumes that the signals arrive simultaneously. This condition can be satisfied by introducing a delay of η_j to the output of the jth seismometer.

4.2 Estimation of Fourier Spectra

As most of the work in this and succeeding chapters is done in the frequency domain, a clear understanding of the Fourier spectrum is necessary. The notation here follows Brillinger (1980).

Dropping the station subscript, define the T length discrete Fourier transform of $u(t)$ as

$$d_u^T(\omega) = \Delta t \sum_{t=0}^{T-1} u(t)e^{-i\omega t} \qquad (4.2.1)$$

where Δt is the sample interval in seconds. The estimated power spectrum of $u(t)$ is found by averaging the amplitudes of the near neighbor frequencies:

$$f_{uu}^T(\omega) = \frac{1}{2M+1} \sum_{j=-M}^{M} |d_u^T(\omega + \frac{2\pi j}{T})|^2. \qquad (4.2.2)$$

By linearity of the Fourier transform

$$d_u^T(\omega) = d_s^T(\omega) + d_\epsilon^T(\omega), \qquad (4.2.3)$$

where $d_\epsilon^T(\omega)$ is distributed as complex normal $N^c(0, f_{\epsilon\epsilon}^T(\omega))$ (Brillinger, 1980) and $d_s^T(\omega)$ is deterministic, so that $d_u^T(\omega)$ is distributed $N^c(d_s^T(\omega), f_{\epsilon\epsilon}^T(\omega))$. The distribution of the power spectrum for the noise is chi-square with $4M+2$ degrees of freedom, i.e.

$$\frac{f_{\epsilon\epsilon}^T(\omega)}{4M+2} \chi_{4M+2}^2 \qquad (4.2.4)$$

(It should be noted that these results are approximate, with the approximation better the larger T and the less correlated $\epsilon_j(t)$.) Much of the work in this and following chapters concerns itself with the Fourier phase. The phase angle is much more difficult to work with than the power spectrum because it has zero mean and smoothing over an arbitrary frequency band may result in a zero phase estimate.

44

4.3 Beamforming

The standard method in array analysis for improving the signal-to-noise ratio (SNR) is beamforming. Beamforming introduces a delay η_j to $u_j(t)$ such that equation 4.1.1 is satisfied. The time shifted signals are then averaged to increase the SNR. The estimate of the signal is called the **beam** and is given by

$$\hat{s}(t) = \frac{1}{N}\sum_{j=1}^{N} u_j(t+\eta_j) = s(t) + \frac{1}{N}\sum_{j=1}^{N}\epsilon_j(t). \tag{4.3.1}$$

For independent Gaussian noise with zero mean, this estimate for $\hat{s}(t)$ is unbiased. Beamforming reduces the variance of $\hat{s}$ from σ_ϵ^2 to $\frac{1}{N}\sigma_\epsilon^2$ assuming $\epsilon_j(t)$ are uncorrelated.

Capon (1967) shows that this estimate also gives both the linear unbiased minimum variance estimate and the maximum likelihood estimate for independent, Gaussian, zero mean noise. The output of the array processor shown in figure 4.1 is

$$\hat{s}(t) = \vec{u}^{\tau}(t)\vec{H}. \tag{4.3.2}$$

where $\vec{H}$ is the vector of filters and τ denotes the transpose. If the filters are normalized so that they sum to unity (e.g. $\vec{H}^{\tau}\vec{\zeta} = 1$) then the estimate is unbiased. The variance is given by

$$Var[\hat{s}] = \vec{H}^{\tau}\mathbf{C}_{\epsilon\epsilon}\vec{H}. \tag{4.3.3}$$

where $\mathbf{C}_{\epsilon\epsilon}$ is the covariance matrix of the noise. Minimizing the variance with respect to $\vec{H}$ can be solved using Lagrange multipliers. The solution is

$$\hat{H} = \frac{\mathbf{C}_{\epsilon\epsilon}^{-1}\vec{\zeta}}{\vec{\zeta}^{\tau}\mathbf{C}_{\epsilon\epsilon}^{-1}\vec{\zeta}}. \tag{4.3.4}$$

If the noise is independent ($\mathbf{C}_{\epsilon\epsilon} = \mathbf{I}\sigma_\epsilon^2$) then $\hat{H} = \frac{1}{N}\vec{\zeta}$ which is the beamforming estimate.

For the maximum likelihood estimate, $\hat{s}$ is chosen such that the probability density function of $\vec{u} = \hat{s}\vec{\zeta} + \vec{\epsilon}$ is a maximum. Assuming Gaussian, zero mean noise, the likelihood function is given by

$$L = (2\pi)^{T/2} |\mathbf{C}_{\epsilon\epsilon}|^{-\frac{1}{2}} \exp\{-\frac{1}{2}(\vec{\epsilon}^{\tau}\mathbf{C}_{\epsilon\epsilon}^{-1}\vec{\epsilon})\}, \quad \text{where } T = dim(\vec{\epsilon})$$

$$= (2\pi)^{T/2} |\mathbf{C}_{\epsilon\epsilon}|^{-\frac{1}{2}} \exp\{-\frac{1}{2}(\vec{u}-s\vec{\zeta})^{\tau}\mathbf{C}_{\epsilon\epsilon}^{-1}(\vec{u}-s\vec{\zeta})\}. \tag{4.3.5}$$

45

Setting $\dfrac{d(\log L)}{ds} = 0$ yields

$$\hat{s} = \frac{\vec{u}^T \mathbf{C}_{\epsilon\epsilon}^{-1} \vec{\zeta}}{\vec{\zeta}^T \mathbf{C}_{\epsilon\epsilon}^{-1} \vec{\zeta}}, \tag{4.3.6}$$

which is identical to the linear unbiased minimum variance estimate and corresponds to beam-forming if $\mathbf{C}_{\epsilon\epsilon} = \mathbf{I}\sigma_{\epsilon}^2$.

These estimates were derived in the time domain, however, Capon gives three problems with actual computations in the time domain:

[1] The method requires a large amount of computer time,

[2] The method is too sensitive to the assumption that the noise is stationary, and

[3] The method is at times sensitive to the assumption that the signal is identical across the array.

Both problems 2 and 3 commonly occur with seismic array data. To correct these difficulties, Capon suggests that the analysis be carried out in the frequency-wavenumber domain.

4.4 Frequency-Wavenumber Analysis

The recorded signals $u_j(t)$ represent a time dependent, two-dimensional wave field $u(\vec{r}_j, t)$ where $\vec{r}_j = (x_j, y_j)$ and may be written as the triple Fourier transform

$$u(\vec{r}, t) = \int_{-\infty}^{\infty} \int_{-\infty}^{\infty} d_u^T(\vec{k}, \omega) \exp\{-i(\vec{k}\cdot\vec{r} - \omega t)\} \, d\vec{k} \, d\omega \tag{4.4.1}$$

where $\vec{k}$ is the horizontal wavenumber vector and ω is frequency. The inverse relation is

$$d_u^T(\vec{k}, \omega) = \int_{-\infty}^{\infty} \int_{-\infty}^{\infty} u(\vec{r}, t) \exp\{i(\vec{k}\cdot\vec{r} - \omega t)\} d\vec{r} \, dt. \tag{4.4.2}$$

The power spectrum is given by

$$f_{uu}^T(\vec{k}, \omega) = |d_u^T(\vec{k}, \omega)|^2. \tag{4.4.3}$$

To estimate $d_u^T(\vec{k}, \omega)$, the spatial integral in equation (4.4.2) is replaced by a weighted sum over the sampled station distribution. After performing the discrete Fourier transform on the sam-

46

pled time series, the spectral estimate becomes

$$f_{uu}^T(\vec{k},\omega) = |\sum_{j=1}^{N} W_j\, d_u^T(\vec{r}_j,\omega)\, \exp\{i\,(\vec{k}\cdot\vec{r}_j)\}|^2 \qquad (4.4.4)$$

$$= \sum_{j=1}^{N} \sum_{l=1}^{N}\, W_j\overline{W_l}\, d_u^T(\vec{r}_j,\omega)\, \overline{d_u^T(\vec{r}_l,\omega)}\, \exp\{i\vec{k}\cdot(\vec{r}_j-\vec{r}_l)\}$$

$$= \vec{W}\, \overline{U}^\tau(k)\, S(\omega)\, \vec{U}(\vec{k})\, \overline{\vec{W}^\tau}, \qquad (4.4.5)$$

where the overbar indicates the complex conjugate. The elements of the **beamsteering vector** are

$$U_j(\vec{k}) = \exp\{i\vec{k}\cdot\vec{r}_j\} \qquad (4.4.6)$$

and have the effect of advancing the phase of the sinusoid observed at station j by an amount corresponding to the time delay with respect to the array origin of a plane wave propagating with wavenumber $\vec{k}$. The estimation of the **cross-spectral matrix** $S(\omega)$ for stationary signals is typically preformed by averaging over several time windows (Capon, 1969). This is unsatisfactory for non-stationary seismic data where we are often restricted to only a single time window. As an alternative, the smoothing is performed over near-neighbor frequencies rather than over multiple time windows. The elements of the cross spectral matrix are

$$S_{jl}(\omega) = \sum_{k=-M}^{M} d_u^T(\vec{r}_j,\omega + \frac{2\pi k}{T})\, \overline{d_u^T(\vec{r}_l,\omega + \frac{2\pi k}{T})}. \qquad (4.4.7)$$

The two methods of estimating $S(\omega)$ have similar statistical properties. In both cases, the values smoothed are assumed to be independent identically distributed complex normal variates. Note that the smoothing over the near-neighbor eigenfrequencies is applied to the individual cross-spectra estimates and not to the Fourier spectral estimates. This is because the complex Fourier transform values have mean zero but the product in equation (4.4.7) has a non-zero mean.

To remove any site amplification effects, the Fourier spectral estimates are normalized to unit amplitude. With this normalization, the cross spectral matrix becomes simply the matrix

47

of exponential phase differences

$$S_{jl}(\omega) = \exp\{i \sum_{k=-M}^{M} [\phi_u^T(\vec{r}_j, \omega + \frac{2\pi k}{T}) - \phi_u^T(\vec{r}_l, \omega + \frac{2\pi k}{T})] \ W_k\}, \qquad (4.4.8)$$

$$where \qquad \phi_u^T(\vec{r}, \omega) = \tan^{-1}\left|\frac{\text{Im}\{d_u^T(\vec{r}, \omega)\}}{\text{Re}\{d_u^T(\vec{r}, \omega)\}}\right| \qquad (4.4.9)$$

and W_k are the weights. By normalizing we also assume that the amplitude of the signal is constant across the frequency band $(\omega - \frac{2\pi M}{T})$ to $(\omega + \frac{2\pi M}{T})$. The choice of the number of frequencies to smooth, $2M+1$, will be discussed below. The choice of the weighting scheme used in equation (4.4.8) is the only difference between two commonly used techniques called the "conventional" and "high resolution" frequency-wavenumber methods.

As shown in equation (4.3.4), the beamforming estimate uses a weighting $W_j = \frac{1}{N}$ for independent noise. This yields the beamforming or "conventional" estimate of the power spectrum

$$P^C(\vec{k}, \omega) = \frac{1}{N^2} \ | \ \overline{U^T}(\vec{k}) \ \mathbf{S}(\omega) \ \vec{U}(\vec{k}) \ | \ . \qquad (4.4.10)$$

The statistical properties of this spectral estimate are given in Capon and Goodman (1970). Assuming the recordings comprise a stationary multi-dimensional Gaussian process with zero mean and $d_u^T(\vec{r}_j, \omega_m)$ is independent of $d_u^T(\vec{r}_k, \omega_n)$, $m \neq n$, the spectral estimate $P^c(\vec{k}, \omega)$ is shown to be a multiple of a chi-square variable with $4M+2$ degrees of freedom with mean and variance

$$E[P^c(\vec{k}_o, \omega)] = \int_{-f_n}^{f_n} \int_{-\infty}^{\infty} \int_{-\infty}^{\infty} P(\vec{k}, \lambda) \ |B(\vec{k} - \vec{k}_o) \ Y_L(\lambda - \omega)|^2 \frac{d\lambda}{2\pi} \ d\vec{k} \qquad (4.4.11)$$

$$Var[P^c(\vec{k}_o, \omega)] = \frac{1}{2M+1} \ \{E[P^c(\vec{k}_o, \omega)]\}^2, \qquad (4.4.12)$$

where $|B(\vec{k})|^2$ is the beamforming array response given by

$$B(\vec{k}) = \frac{1}{N} \sum_{n=1}^{N} \exp(i\vec{k} \cdot \vec{r}_n), \qquad (4.4.13)$$

48

and $|Y_L(\lambda)|^2$ is the frequency window function. In the following analysis, a triangle window is used. If the wave field consists only of a plane wave with wavenumber $\vec{k}_o$, then $P^c(\vec{k}_o,\omega)=1$. If the wave field is white noise then the phase differences will be distributed uniformly on $-[\pi,\pi]$ and the expected value of the peak will be dependent on the amplitude of the side lobes in the beam pattern.

Using singular value decomposition (SVD) on $S(\omega)$, McLaughlin (1983) shows that

$$P^C(\vec{k},\omega) = \frac{1}{N^2} \mid \overline{\overline{U^T}}(\vec{k}) \; V \; \Lambda \; \overline{\overline{V^T}} \overline{U}(\vec{k}) \mid \qquad (4.4.14)$$

where V is the matrix of eigenvectors of S and Λ is the matrix of eigenvalues of S. This can be written as

$$P^c(\vec{k},\omega) = \frac{1}{N^2} \mid \sum_{j=1}^{N} \lambda_j \; \overline{\overline{U^T}}(\vec{k}) \; \vec{V}_j \; \overline{\overline{V_j^T}} \; \overline{U}(\vec{k}) \mid, \qquad (4.4.15)$$

where λ are the eigenvalues and $\vec{V}_j$ are the columns of V. This decomposition provides a convenient comparison with the high resolution frequency-wavenumber method discussed in the following section.

4.4.1 High Resolution Frequency-Wavenumber Analysis

The high resolution (HR) method proposed by Capon (1969) uses a more complex weighting scheme than beamforming. The weights W_j are chosen such that they satisfy two conditions:

[1]   Pass a pure plane wave with wave number $\vec{k}_o$ undistorted.

[2]   Minimize in a least-squares sense the variance of the noise (signals with wavenumbers $\vec{k} \neq \vec{k}_o$).

The weights which satisfy these conditions are different for each frequency and wavenumber. Capon shows that these weights are equivalent to estimating the power spectrum by

$$P^{HR}(\vec{k},\omega) = \left[\mid \overline{\overline{U^T}}(\vec{k}) \; S^{-1}(\omega) \; \overline{U}(\vec{k}) \mid \right]^{-1}. \qquad (4.4.1.1)$$

The statistical properties of this power spectral estimate are also discussed by Capon and

Goodman (1970) who show that $P^{HR}(\vec{k},\omega)$ has a distribution of $(\overline{U}^\tau \, C_{\epsilon\epsilon}^{-1} \, U)^{-1} \, \chi^2_{2(2M-N+2)}$ where χ^2 denotes the chi-squared variate and $C_{\epsilon\epsilon}$ is the covariance matrix of the noise. They also show that $P^{HR}(\vec{k},\omega)$ is biased, however, this bias is removed when the wavenumber spectrum is normalized by the amplitude of the largest peak.

Using SVD, equation (4.4.1.1) becomes

$$P^{HR}(\vec{k},\omega) = \left[\; \left| \; \sum_{j=1}^{N} \frac{1}{\lambda_j} \, \overline{U}^\tau \, \overline{V}_j(\omega) \, \overline{V}_j^\tau(\omega) \, \overline{U}(\vec{k}) \; \right| \; \right]^{-1} . \qquad (4.4.1.2)$$

Comparing equations (4.4.15) and (4.4.1.2), McLaughlin (1983) shows that the difference between the beamforming and HR methods is the weights given to the eigenvectors. Beamforming applies weights that are linearly proportional to the associated eigenvalue while the HR method applies weights that are inversely proportional to the associated eigenvalue. The weighting used in the HR method is a numerical technique that takes advantage of the statistical properties of the noise to increase the resolution.

Note that the number of degrees of freedom in the high-resolution distribution is 2M-N+2. For the chi-squared distribution to be valid, the cross-spectral matrix must be smoothed over at least as many frequencies as there are stations $(2M+1 \geqslant N)$. For example, if all 27 stations which triggered the SMART 1 array during event 5 are used in the frequency-wavenumber analysis, then the cross-spectral matrix must be smoothed over at least 27 frequencies. The P and S wave windows used from event 5 are each approximately 5 seconds long and a 512 point FFT ($\Delta t = 0.01$ seconds) gives a frequency sample interval of ≈ 0.2 Hz. Smoothing over 27 frequencies thus results in a frequency bandwidth of 5.4 Hz. This bandwidth is much too large for the frequency resolution required in this study where bandwidths on the order of 0.5 - 1.0 Hz are required.

To achieve a smaller bandwidth requires either increasing the window length or decreasing the number of stations used in the analysis. The window length could be increased by padding the recorded time series with zeros, but then the Fourier values would no longer be

50

independent which was an assumption in the derivation of the distribution of $P^{HR}(\vec{k},\omega)$. Therefore, padding with zeros will not help to obtain a smaller bandwidth. Again, in the case of event 5 and SMART 1, achievement of a 1.0 Hz bandwidth requires reducing the number of stations used in the analysis to six. This reduction is inadequate because it would result in severe spatial aliasing.

Estimates of $P^{HR}(\vec{k},\omega)$ can be made using smoothing over fewer frequencies than stations, but the statistical distributions given above will not be valid. Furthermore, the cross-spectral matrix will become singular because its dimension is N but the rank is only $2M+1$ with $N>2M+1$. A common numerical technique is to pre-whiten $S(\omega)$ by adding a small constant to the diagonal of $S(\omega)$ to shift the eigenvalues away from zero. This technique is known as Levenburg-Marquardt stabilization (Lawson and Hanson, 1974, chapter 25).

In a detailed comparison of the conventional and high resolution methods, Liaw (1977) showed that in general, the high resolution method yields sharper peaks in the power spectrum than the conventional method because the HR method produces much smaller sidelobes in the impulse response of the array than the conventional method. Note the relatively large rings around the central peak in the impulse response of the conventional method (figure 4.2a) compared to the very small sidelobes of the high resolution method (figure 4.2b). For this study, however, the distribution for the HR method is invalid for the frequency bandwidths required. The approach used here will be to apply the high resolution method for qualitative measures of the coherency and the conventional method for quantitative measures of the wave coherency.
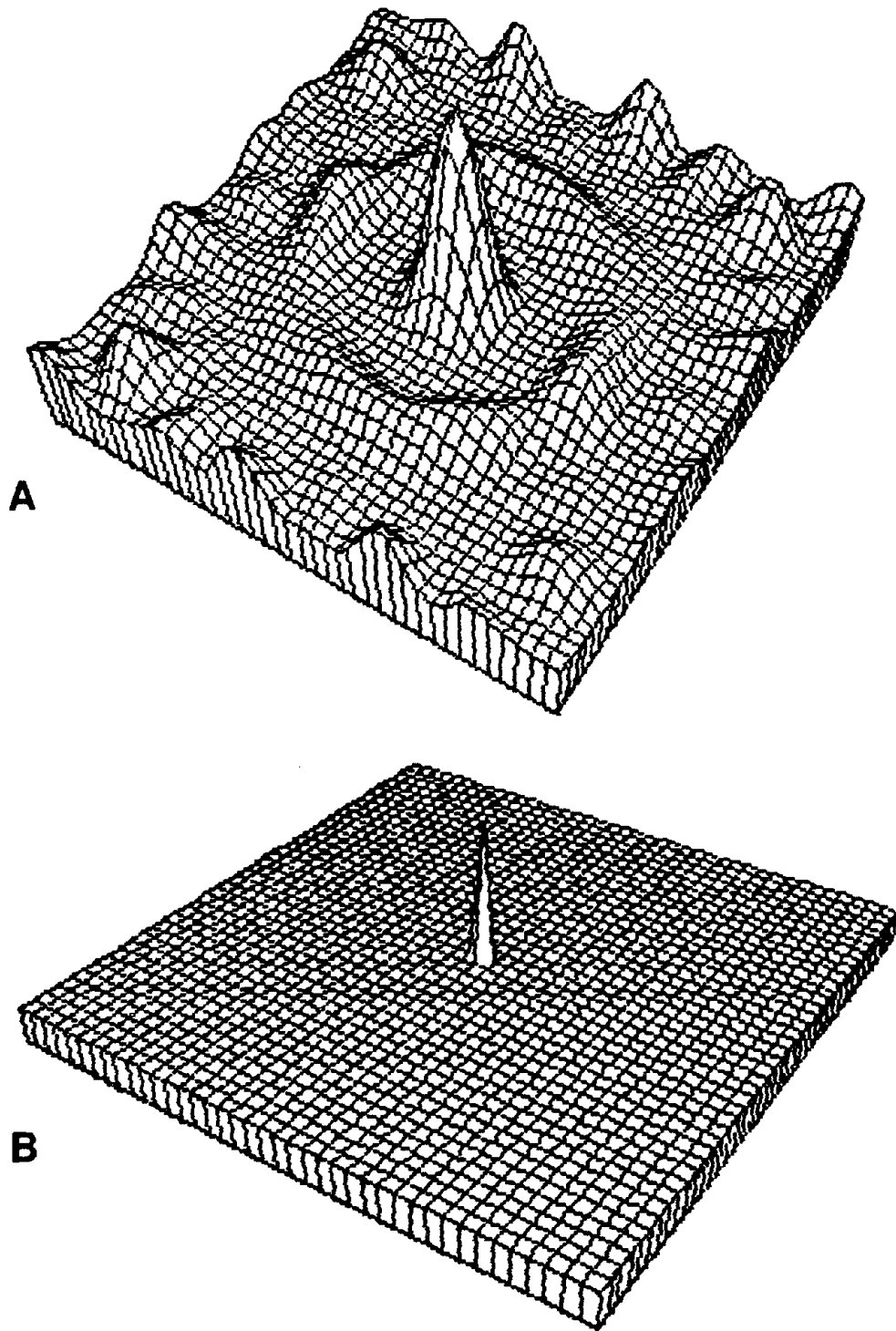
Figure 4.2 Beam pattern of the SMART 1 array for the 27 stations operational during the January 29,1981 event. (a) Conventional method. (b) High resolution method.

Chapter 5

Wave Coherency

5.1 Introduction

The resolution of the details of the moving seismic source requires analyzing waves with as high frequency as possible, but the waves must also be direct arrivals from the source region and not scattered or incoherent energy. The goal of this chapter is to determine the frequency bands of coherent energy from the source region for the event 5 accelerograms.

In the previous chapter, frequency-wavenumber $(\omega-k)$ spectral analysis was discussed. The wavenumber spectrum provides an estimate of the speed and azimuth of a plane-wave fit to the recorded wave field. The various wave types (e.g. P, S and surface waves) will have different apparent velocities across the array, so $\omega-k$ analysis can be used to separate the wave types through velocity filtering, but for coherency estimates, it is simpler to separate each wave type through temporal windowing when possible before applying the $\omega-k$ analysis. In the study of event 5, both conventional and high resolution wavenumber spectra are generated for comparison.

Visual inspection of the wave number spectra provides a simple qualitative measure of the wave coherence. If there is a single large peak or "mountain" dominating the spectrum, then the wave field can be described quite well by a single plane wave, but if there are no dominant peaks in the wavenumber spectrum, then the wave field is more complex than simple plane waves. Spherical wavefronts can smear the wavenumber spectrum, however, this effect is not significant for the event 5 recordings because the largest dimension of the

53

SMART 1 array is 4 km which results in a curvature across the array of the spherical wave-front from the hypocenter region of only 8°. This small amount of curvature produces a max-imum deviation of 67 meters from the plane wave approximation while the wavelengths of the P and S waves are greater than 1000 meters at frequencies below 10 Hz and 5 Hz respec-tively. If the source was closer to the array, then a correction for spherical waves would be necessary. In this case, however, the absence of a dominant peak in the wavenumber spec-trum is not due to spherical wavefronts but rather to incoherent waves. Three possible causes of incoherent waves are

[1]   Quantization noise due to small Fourier amplitudes,

[2]   Scattering of the waves near or within the array, and

[3]   Multiple diffraction and refraction of the waves as they pass through complex velocity structures below the array.

The first possibility can be eliminated if the analysis is restricted to the frequency band with amplitudes well above the quantization noise level.

A quantitative measure of the relative wave coherency at various frequencies is the amplitude of the peak power of the conventional wavenumber spectrum (see equation 4.4.10). A coherence function $C(\omega)$ can be defined as

$$C(\omega) = \max_{i,j} (P^C(k_{i,j},\omega)). \qquad (5.1.1)$$

where $P^C(k_{i,j},\omega)$ is the conventional estimate of the power in the wavenumber spectrum. A pure plane wave results in $C(\omega)=1$ while white noise gives a $C(\omega)$ that is dependent on the beam pattern and the number of eigenfrequencies used in the frequency smoothing. In the case of SMART 1, using only the middle ring stations, inner ring stations and central station (17 total), the wavenumber spectrum of white noise has an expected maximum value of 0.23 for 7 point smoothing ($M=3$ in equation (4.4.8), bandwidth$=0.6$ Hz for 512 point FFT). Using all 27 stations with 7 point smoothing gives an expected maximum in the wavenumber

54

spectrum of 0.15. The variances of these estimates are given by equation (4.4.12) and are 0.0076 and 0.0032 respectively for these two cases. If $C(\omega) > 0.40$ for the 17 station configuration or $C(\omega) > 0.26$ for the 27 station configuration, then the peak in the spectrum is significant at the 95% confidence level.

5.2 P Wave Coherency

The mean Fourier amplitude spectrum normalized at 1 Hz and averaged over all 27 vertical component recordings for the 4 second P wave window from event 5 (see figure 3.11a) is shown in figure 5.1. Note that there is high power over the frequency band 1-10 Hz. The scalloping between 4 and 10 Hz is due to the resonance of the soils beneath the array (see section 2.2). The relative coherency is measured over this frequency band. Figures 5.2a-5.2j show the conventional wavenumber spectra at frequencies 1-10 Hz using the 17 station configuration consisting of the middle and inner rings and the central station. The frequency bandwidth is $\pm 0.6 (M=3)$ Hz in each case. These spectra are all plotted at the same scale and the view is looking down from the southeast which is the epicentral direction. The horizontal axes are wavenumber in cycles/km so the slowness s and azimuth $\theta(t)$ are given by

$$s = \frac{[k_x^2 + k_y^2]^{\frac{1}{2}}}{f},$$

$$\theta(t) = 90 - \tan^{-1}[\frac{k_y}{k_x}],$$

(5.2.1)

where f is the center frequency in Hz and k_x and k_y are the horizontal components of the wavenumber vector. The center of each plot is zero slowness or infinite velocity. The rings around the central peak are the array response (see figure 4.2a). A dominant peak in the source region direction is evident up to 3 Hz (figures 5.2a-5.2c). At 4 Hz, there is a sharp decay in the peak but the dominant peak returns at 5 Hz. Above 7 Hz, there are no dominant peaks in the spectra.

Figures 5.3a-5.3j show the high resolution wavenumber spectra over the same

bandwidths for the 17 station configuration. These spectra have been normalized such that the largest peak in each spectrum has unit amplitude. For these high resolution plots, the background noise is scaled larger as the coherence decreases. The increase in resolution using the high resolution method is obvious. At 1 and 2 Hz, there is a single peak dominating the spectrum, but at 4 Hz, there is a clear decay in the coherence. The peak becomes dominant again at 5 Hz. Above 7 Hz, there is still a peak in the epicentral direction but the background amplitude becomes substantial.

The relative coherency function defined using the conventional wavenumber spectra is shown in figure 5.4. The horizontal lines indicates the 95% confidence level of the noise for the 17 and 27 station configurations (maximum distances of 2 km and 4 km respectively). Values in the coherency function above these levels are significant at the 95% confidence level. The decay in the coherence near 4 Hz is evident. The coherence increases between 4 and 5 Hz before finally decaying below the 95% confidence level at frequencies above 7 Hz for the 17 station sub-array and above 6.5 Hz for the 27 station full array.

There is no simple physical reason for the gap in the coherence at 4 Hz. The amplitude in the Fourier spectrum at 4 Hz is well above the quantization noise level. so poor resolution of the signal is not the cause of the loss of coherency. If the loss of coherency is due to rigid scattering of the seismic waves, then the energy at higher frequencies should also show a similar loss of coherency. A possible explanation is that the scatterers have a resonance at 4 Hz, however, it is unlikely that all of the scatterers resonate over a narrow (1 Hz) frequency band.

The analysis of the P wave coherence has been on the four second P window before the S wave arrival. The analysis could be applied to windows after the S arrival. An example of the wavenumber spectrum at 2 Hz for the vertical component during the S arrival is shown in figure 5.5. There are two distinct peaks in the spectrum, one at the P wave slowness ($s = 0.09$ sec/km) and one at the S wave slowness ($s = 0.3$ sec/km). The P wave peak is approximately

3 db below the the S wave peak, indicating that at 2 Hz, there is slightly more S energy than P energy during this window. Figure 5.5 demonstrates that frequency-wavenumber analysis can be used to determine the percentage of energy that is coherent P or S waves as a function of frequency and time in the record. A detailed study of the separation of wave types is left to future work.

5.3 S Wave Coherency

The mean Fourier amplitude spectrum normalized at 1 Hz and averaged over all 27 radial components for the 5 second S wave window from event 5 (see figure 3.11b) is shown in figure 5.6a. There is good resolution over the frequency band 0.5-6 Hz.

Figures 5.7a-h show the conventional wavenumber spectra for the radial component at 0.5 to 6 Hz using the 17 station configuration (maximum separation of 2 km). A dominant peak at the azimuth of the source region is evident up to 1.5 Hz (figures 5.7a-c). At 2 Hz, there is a rapid decay in the peak and the coherence remains low at the higher frequencies. The relative coherency function is shown in figure 5.8. The rapid decay in the coherency at 2 Hz is evident. Above 4 Hz, the peaks are not significant at the 95% confidence level.

Figures 5.9a-h show the high resolution wavenumber spectra over the same bandwidths. Again, the increase in resolution using the high resolution method is obvious. There is a dominant peak in the spectrum up to 2.0 Hz, but then the background quickly dominates the spectrum above 3 Hz. The transverse component wavenumber spectra (not shown) exhibit a similar pattern of coherency with frequency.

5.4 Implications for Synthetic Seismograms

The coherence of strong ground motions over short distances has important implications for waveform modeling and the generation of synthetic strong motion seismograms. In previous studies, (Olson and Apsel, 1982 and Hartzell and Heaton, 1983) waveform modeling could not match the observed high frequency waves. This can be explained in part by a loss

of coherency at the high frequencies. The velocity models are not precise enough to describe the behavior of the high frequency waves. Small variations in the velocity structure can produce significant phase shifts in the high frequency energy.

The coherency estimates from the previous sections indicate that waveform modeling should be able to match the Event 5 P waves at frequencies up to 3 Hz and the S waves at frequencies up to 1.5 Hz. Above these frequency levels, the accelerograms contains significant amounts of incoherent energy so that any attempt at deterministic waveform modeling is impractical.

These results suggest the following method for generating synthetic strong motion seismograms. The low frequency part of the accelerogram can be generated using deterministic methods such as convolving a source time function with a Green's function (Aki and Richards, 1980, chapter 4). As the frequency increases, the percentage of incoherent or random energy also increases. At high frequencies, the recorded motion may be dominated by the random energy. A suite of ground motions at a single site can be generated, with only one convolution of the source with the Green's function, by resampling the random energy while keeping the coherent energy constant.
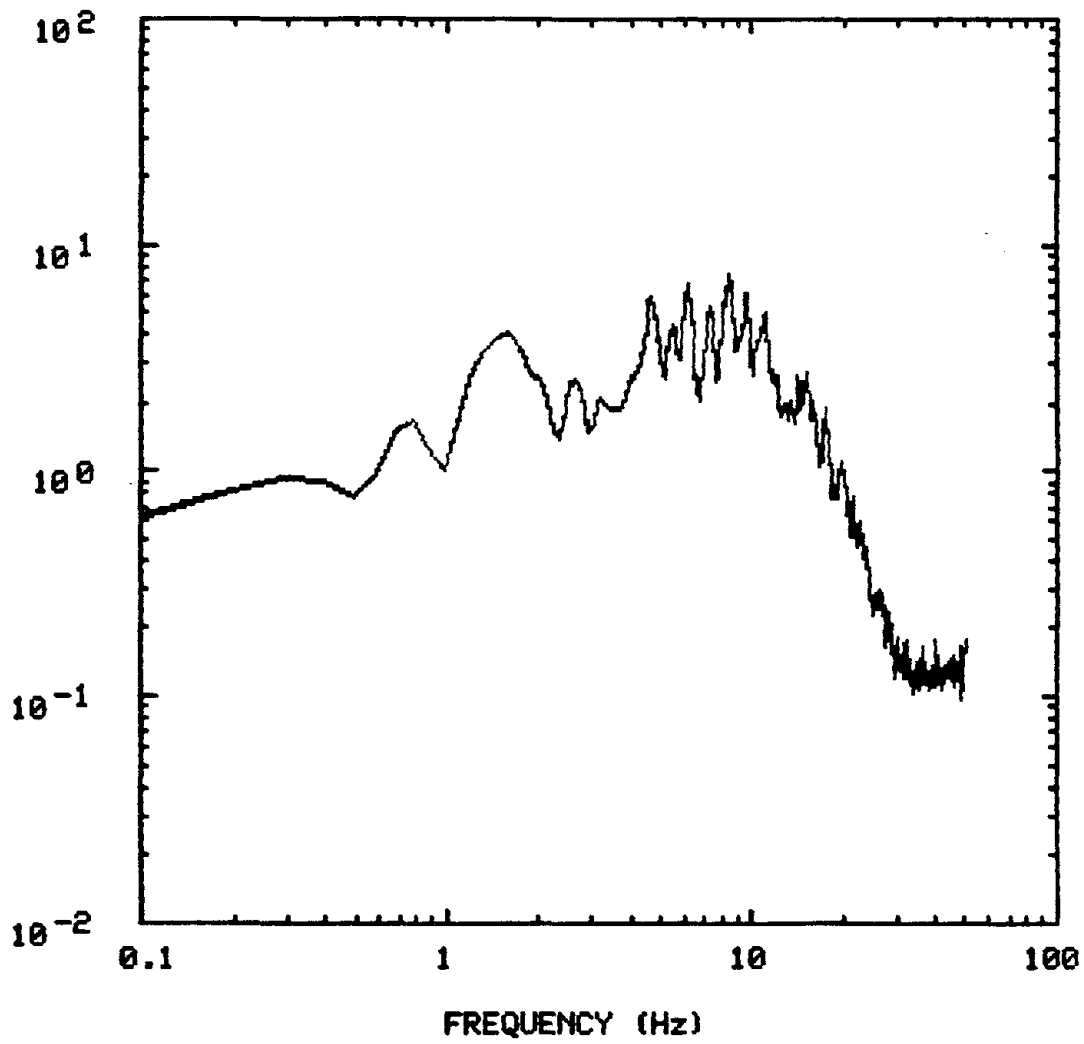
Figure 5.1 The mean Fourier amplitude spectrum normalized at 1 Hz and averaged over all 27 vertical components for the P wave window during event 5.
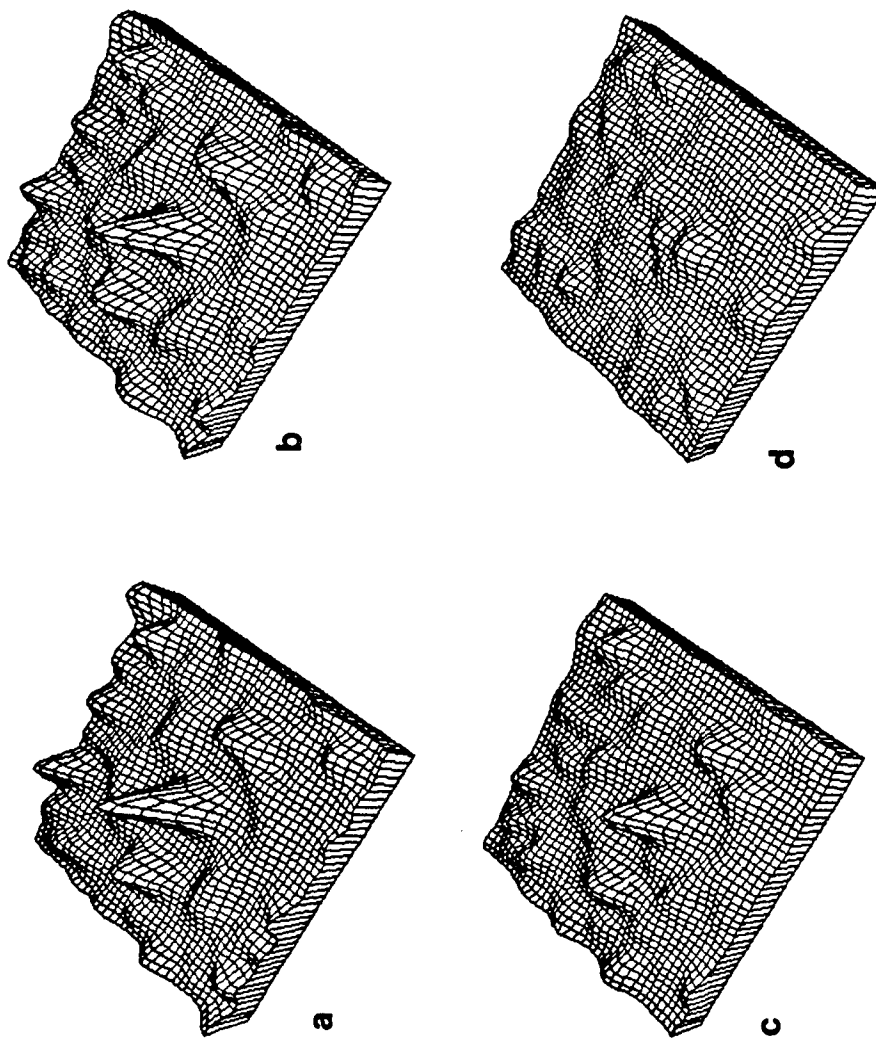
Figure 5.2 Conventional wavenumber spectra of the vertical component for the P wave window during event 5. The view is looking down from the southeast. All of the plots are at the same scale.

(a) 1 Hz. (b) 2 Hz. (c) 3 Hz. (d) 4 Hz.
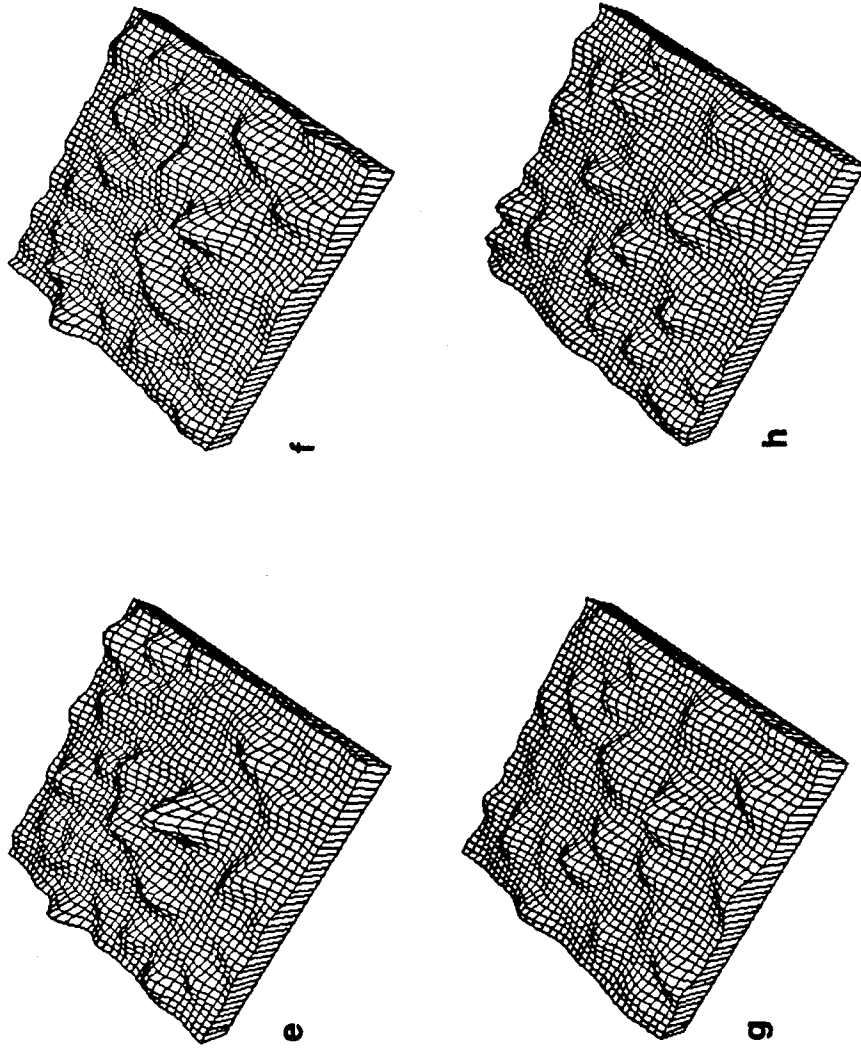
Figure 5.2 Conventional wavenumber spectra of the vertical component for the P wave window during event 5. The view is looking down from the southeast. All of the plots are at the same scale.
(e) 5 Hz. (f) 6 Hz. (g) 7 Hz. (h) 8 Hz.
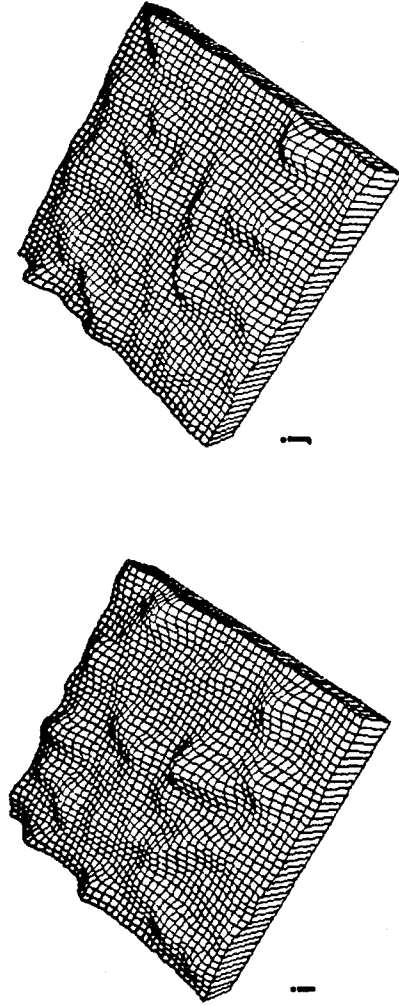
61

Figure 5.2 Conventional wavenumber spectra of the vertical component for the P wave window during event 5. The view is looking down from the southeast. All of the plots are at the same scale.

(i) 9 Hz. (j) 10 Hz
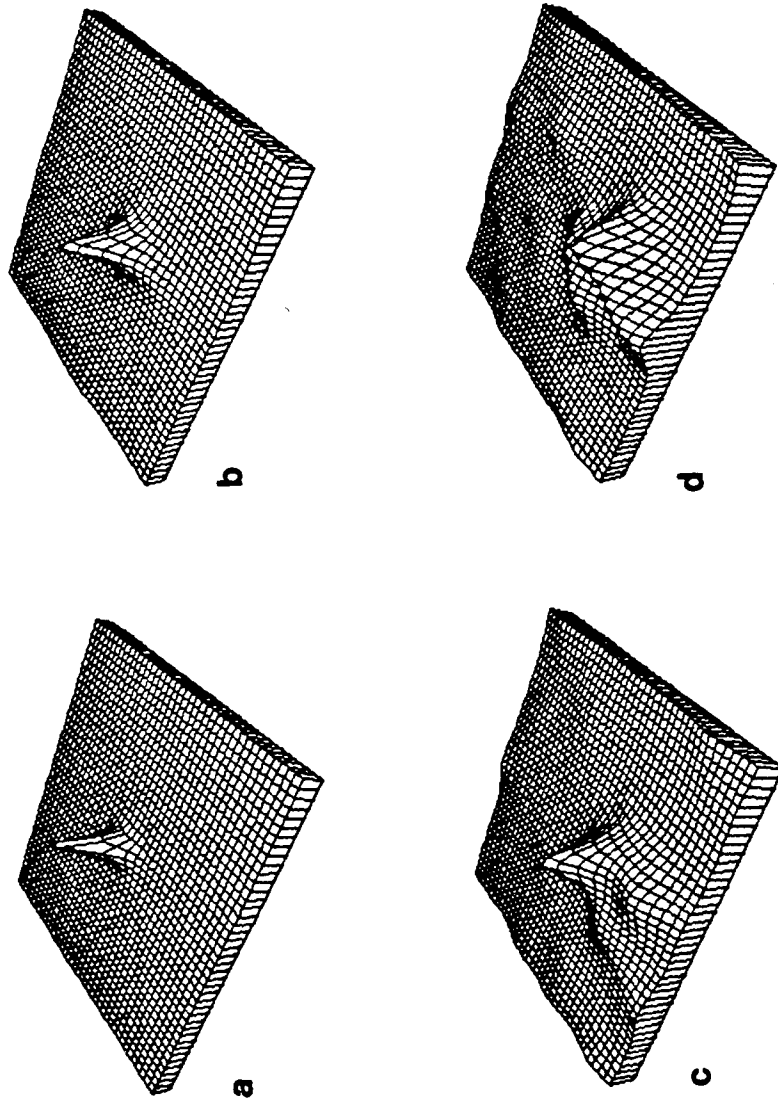
Figure 5.3 High resolution wavenumber spectra of the vertical component for the P wave window during event 5. The view is looking down from the southeast. The maximum peak in each plot is scaled to unit amplitude.
(a) 1 Hz. (b) 2 Hz. (c) 3 Hz. (d) 4 Hz.
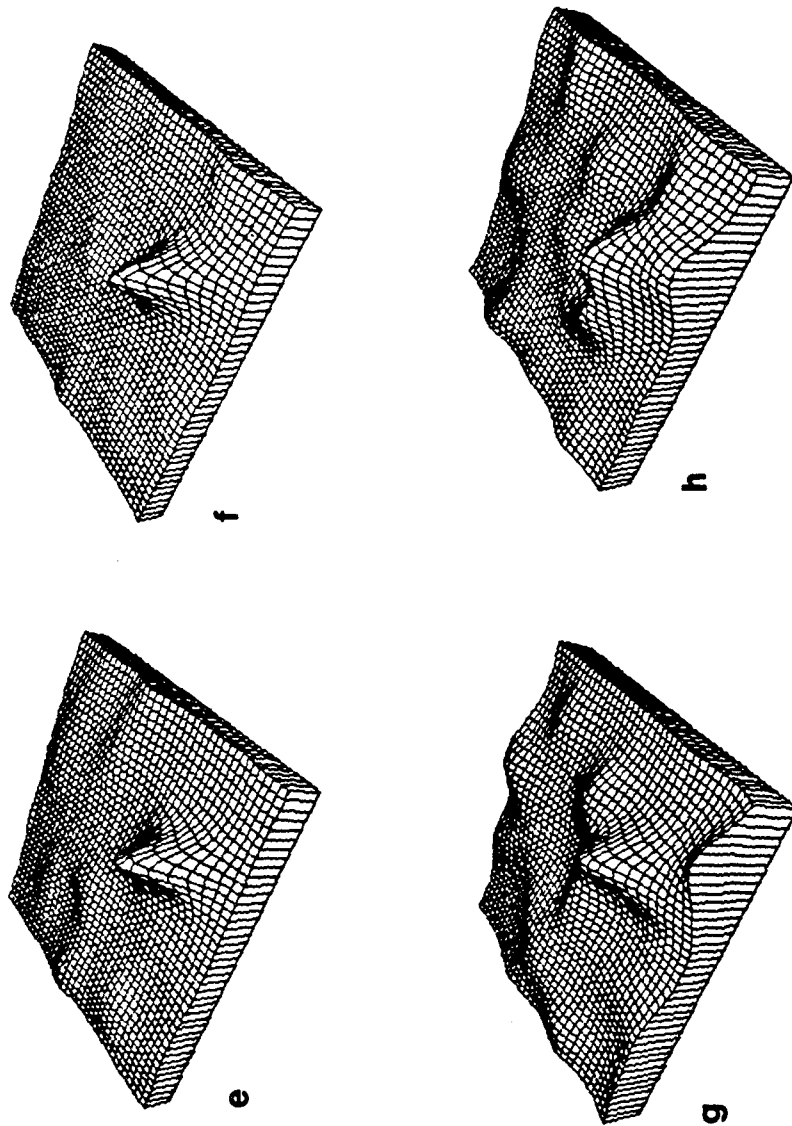
Figure 5.3 High resolution wavenumber spectra of the vertical component for the P wave window during event 5. The view is looking down from the southeast. The maximum peak in each plot is scaled to unit amplitude.
(e) 5 Hz. (f) 6 Hz. (g) 7 Hz. (h) 8 Hz.
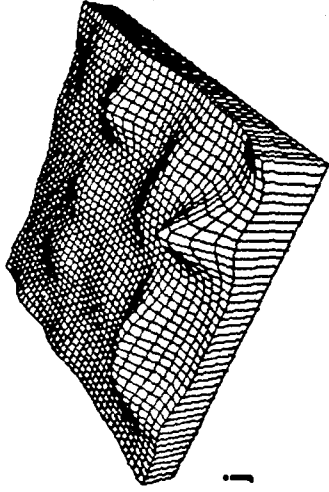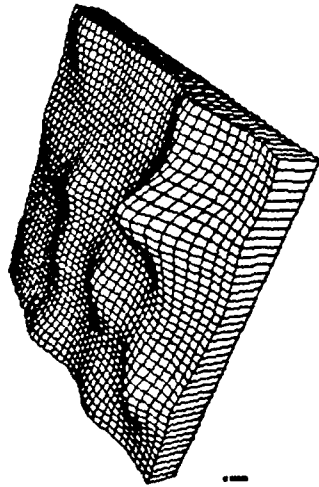
Figure 5.3 High resolution wavenumber spectra of the vertical component for the P wave window during event 5. The view is looking down from the southeast. The maximum peak in each plot is scaled to unit amplitude.
(i) 9 Hz. (j) 10 Hz.
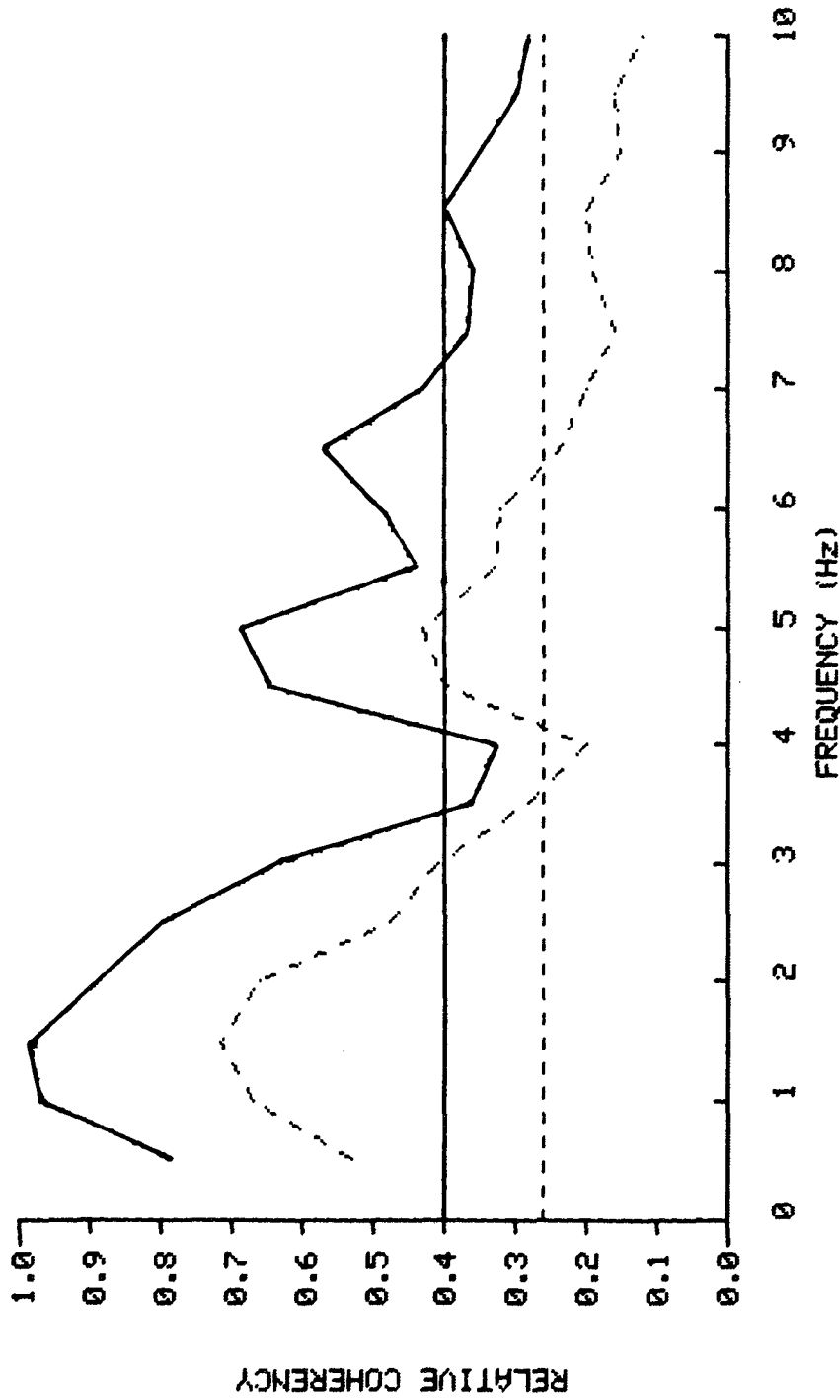
Figure 5.4 The relative coherency of the vertical component for the P wave window during event 5. The solid line is for the 17 station configuration and the dashed line is for the 27 station configuration. The horizontal lines indicate the 95% confidence level of white noise for the two station configurations.
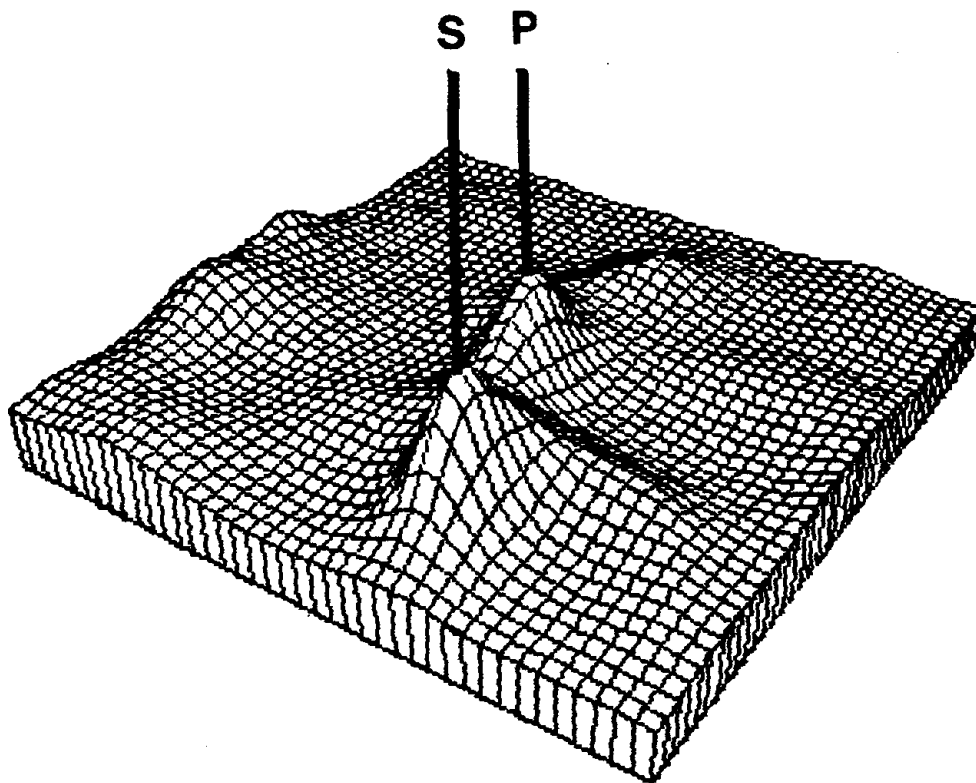
Figure 5.5 High resolution wavenumber spectrum of the vertical component during the first 2 seconds of the S window during event 5. This time window during event 5 contains both P and S waves. The two wave types show up as two large peaks in the spectrum.
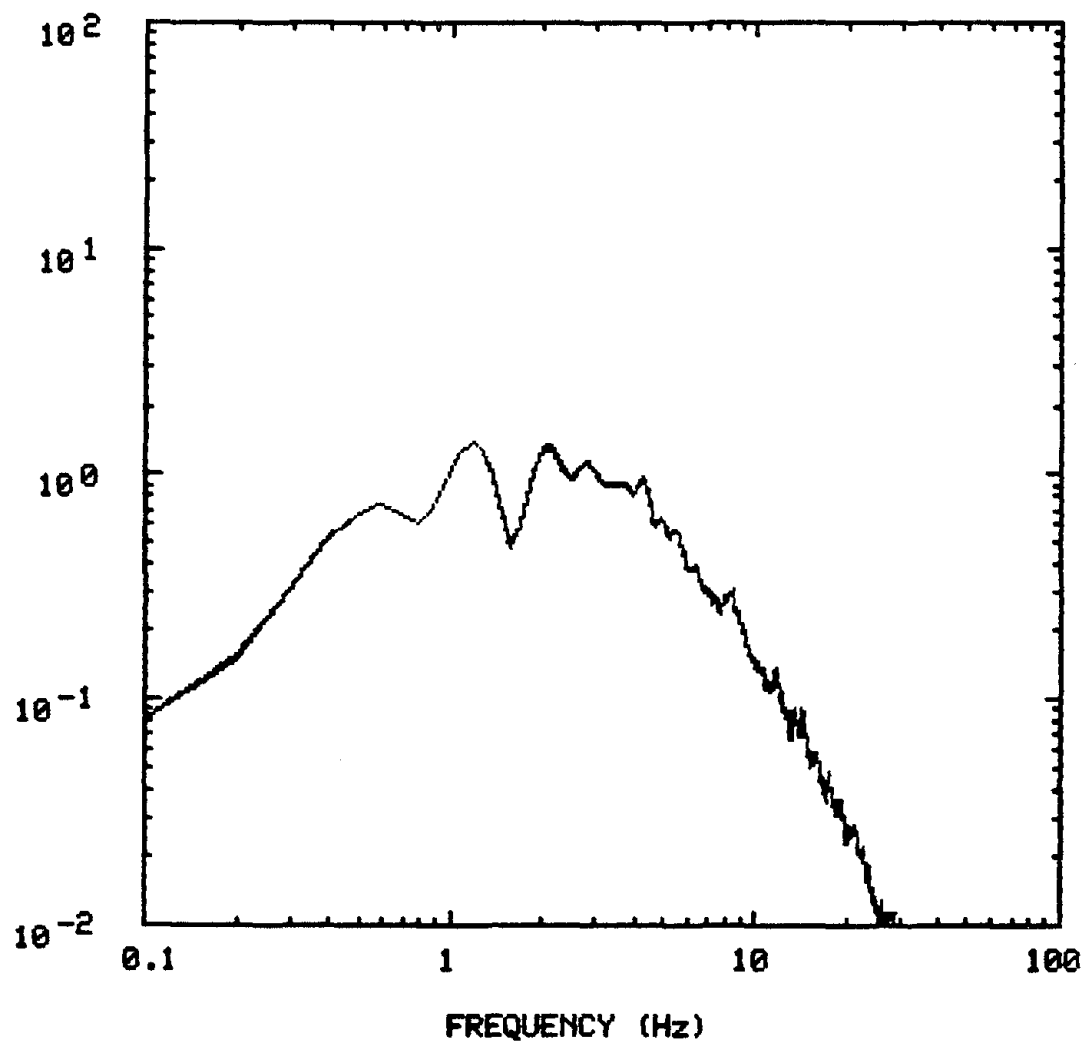
Figure 5.6 The mean Fourier amplitude spectrum normalized at 1 Hz and averaged over all 27 radial components for the S wave window during event 5.
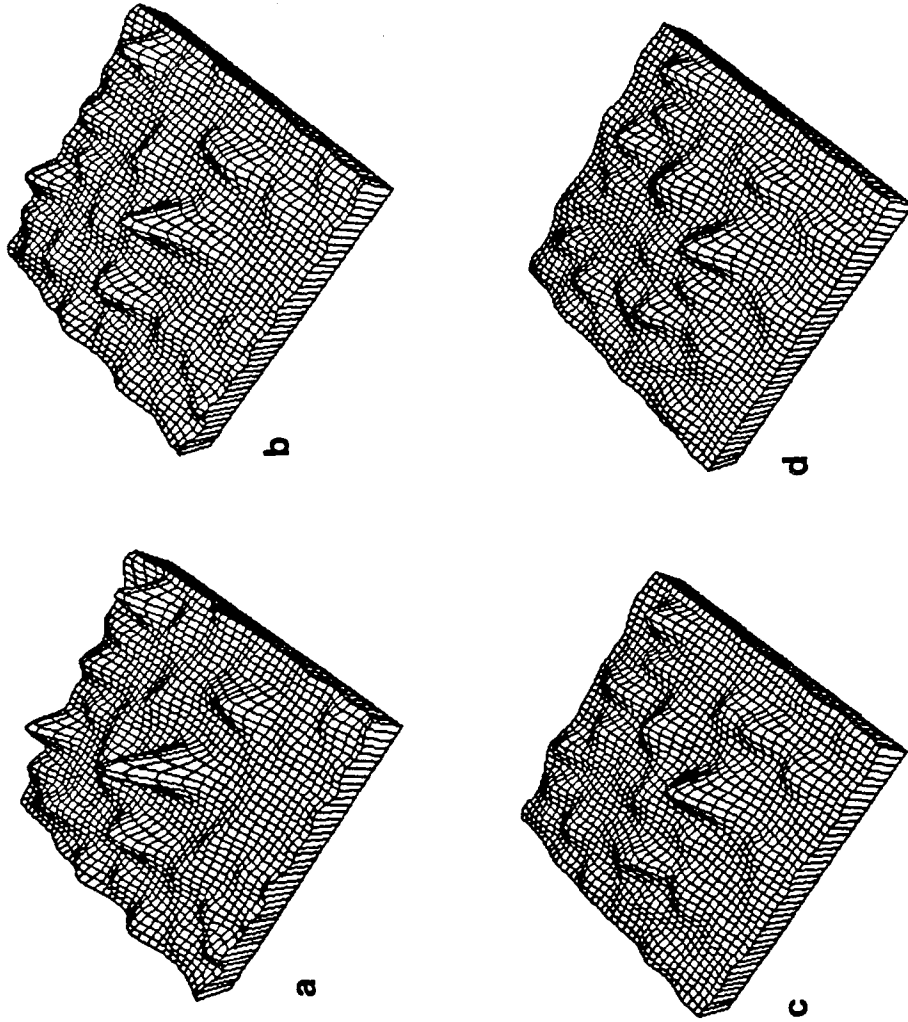
Figure 5.7 Conventional wavenumber spectra of the radial component for the S wave window during event 5. The view is looking down from the southeast. All of the plots are at the same scale.
(a) 1.0 Hz.   (b) 1.5 Hz.   (c) 2.0 Hz.   (d) 2.5 Hz.
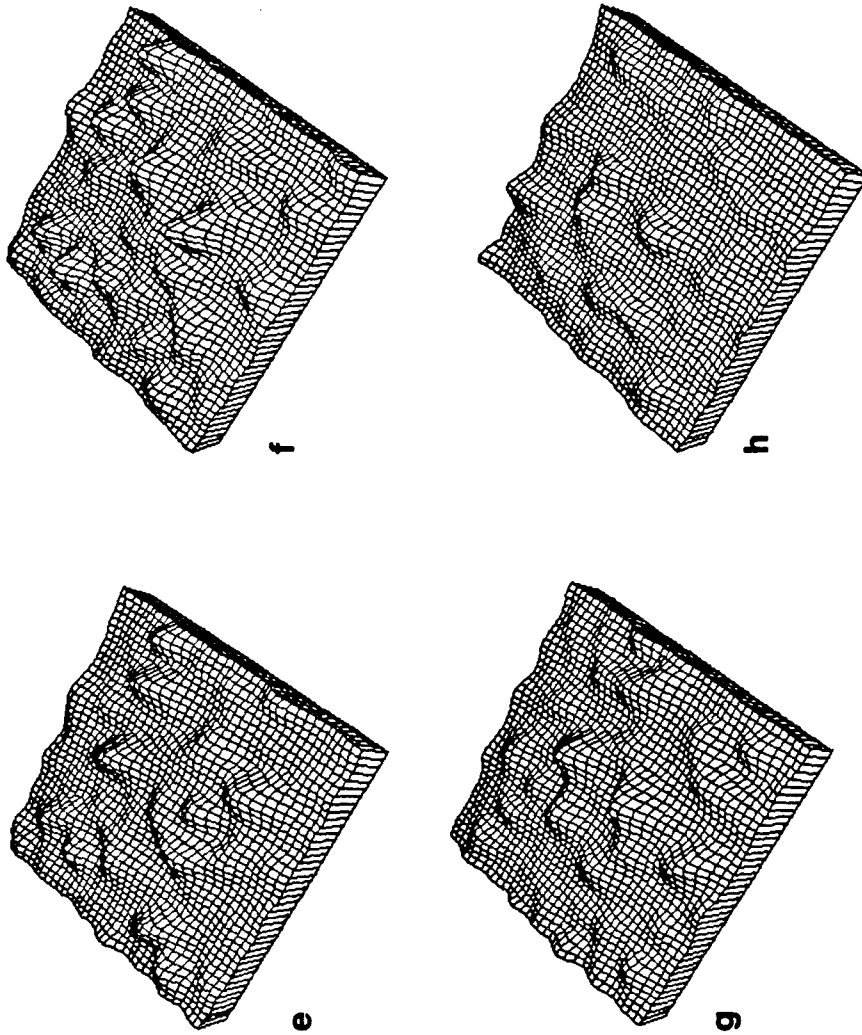
Figure 5.7 Conventional wavenumber spectra of the radial component for the S wave window during event 5. The view is looking down from the southeast. All of the plots are at the same scale.
(e) 3 Hz. (f) 4 Hz. (g) 5 Hz. (h) 6 Hz.
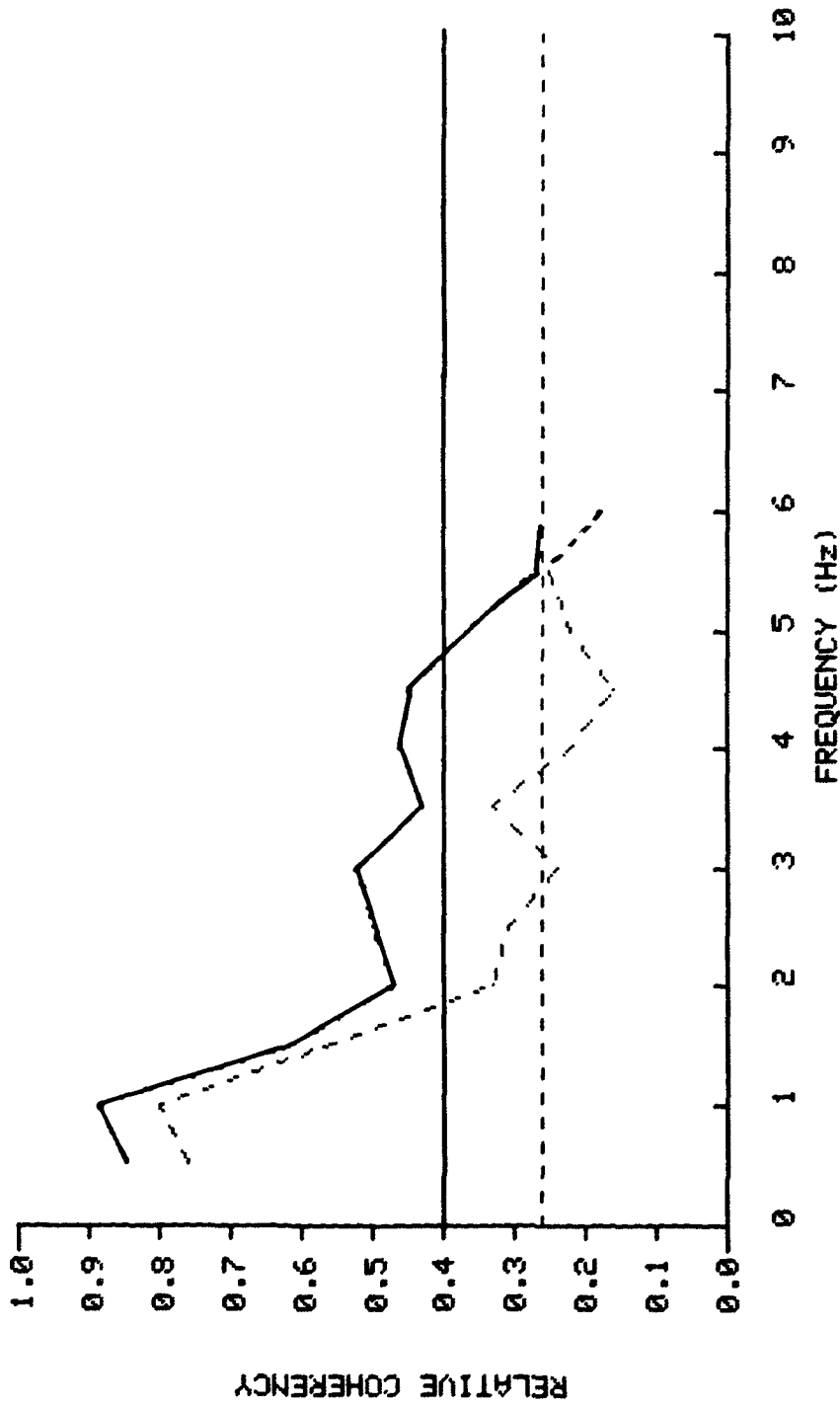
Figure 5.8 The relative coherency of the radial component for the S wave window during event 5. The solid line is for the 17 station configuration and the dashed line is for the 27 station configuration. The horizontal lines indicate the 95% confidence level of white noise for the two station configurations.
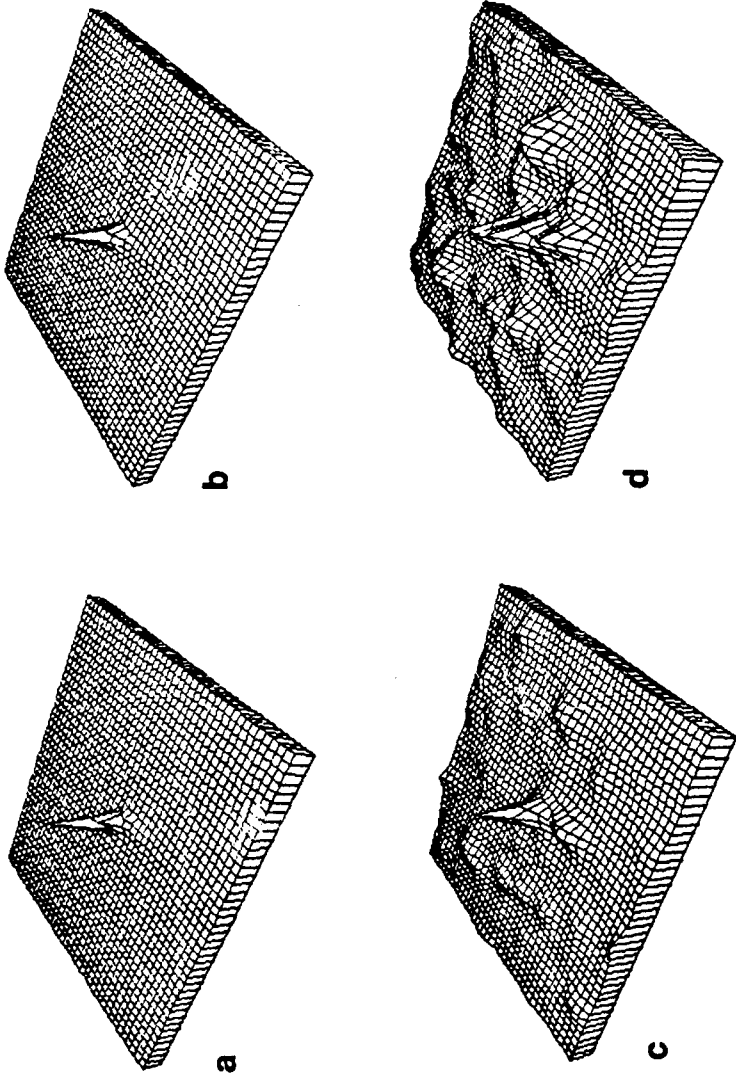
Figure 5.9 High resolution wavenumber spectra of the radial component for the S wave window during event 5. The view is looking down from the southeast. The maximum peak in each plot is scaled to unit amplitude.
(a) 1.0 Hz. (b) 1.5 Hz. (c) 2.0 Hz. (d) 2.5 Hz.
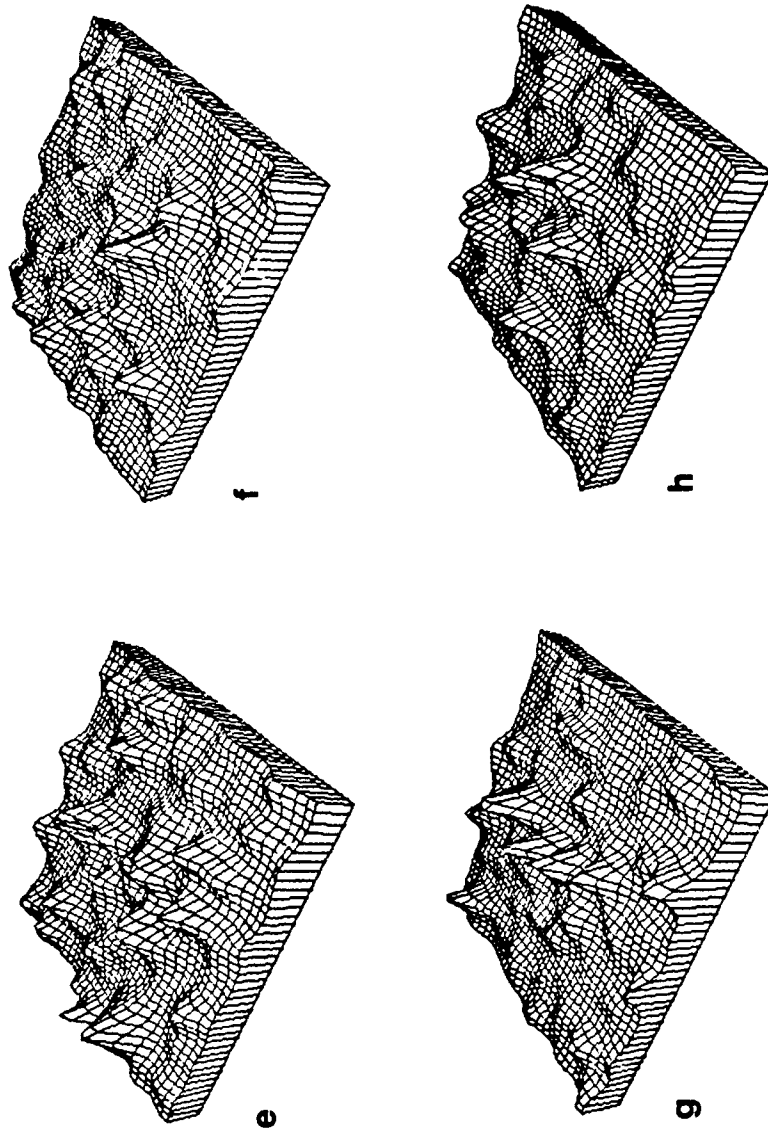
Figure 5.9 High resolution wavenumber spectra of the radial component for the S wave window during event 5. The view is looking down from the southeast. The maximum peak in each plot is scaled to unit amplitude. (e) 3 Hz. (f) 4 Hz. (g) 5 Hz. (h) 6 Hz.

73

CHAPTER 6

Rupture Velocity

6.1 Introduction

In this chapter, estimates are found for the rupture velocity during the earthquake called event 5. Both single station and array estimates are calculated.

One of the simpliest estimates of the average rupture velocity is found using the ω^2 or "Brune" spectral model (see chapter 1). The average rupture velocity is given by

$$V_r = \frac{\beta}{\dfrac{2\beta}{L\omega_c} + \cos\theta_o},$$

where β is the shear wave velocity, L is the fault length, ω_c is the corner frequency of the Fourier displacement spectrum of the SH pulse and θ_o is the angle between the rupture direction and the station azimuth from the epicenter. A typical SH wave (transverse component) displacement spectrum from event 5 is shown in figure 6.1. The estimated DC level and high frequency asymptote are drawn. The corner frequency is estimated at 0.7 Hz. As explained in chapter 3, the fault length defined by the aftershock distribution is approximately 25 km and the shear wave velocity is approximately 3.5 km/sec in the source region. The strike of the fault is N109E $\pm 8.2°$ (see page 28, chapter 3) giving $\theta_o = 41°\pm 8.2°$. These parameters give an average rupture velocity $V_r = 3.0 \pm 0.2$ km/sec where the standard error represents only the uncertainty in the angle θ_o. The mean rupture velocity found using the SH spectra of all 27 transverse components is 3.05 km/sec with a standard error of 0.27 km/sec based on the uncertainty in the angle θ_o and the corner frequency ω_c.

In the previous chapter, the recorded accelerograms were seen to contain predominantly coherent energy propagating from the the source region at frequencies up to 3 Hz during the P wave window and at frequencies up to 1.5 Hz during the S wave window. The SMART 1 accelerograms are now studied in detail over these two frequency bands for evidence of a moving source.

In this chapter, the words "rupture" and "rupture front" refer to the position of the source centroid of coherent high frequency (> 1.0 Hz) energy. This is similar to the meaning used by Spudich and Cranswick (1984). They note that based on the conclusion of Madariaga (1977, 1983), the high frequency energy radiated by a crack originates at the crack tip so the position of the rupture corresponds to the crack tip.

Near-source array recordings have been used by Spudich and Cranswick (1984) to study the details of the source mechanism of the 1979 Imperial Valley earthquake. They applied a cross-correlation technique to measure the slowness of the waves across the El Centro Differential Array. A major difficulty in the data was the restriction to a scalar slowness rather than a vector slowness caused by the uni-dimensional array. The absence of a second dimension to the array made it impossible to determine uniquely the rupture velocity. Determination of a rupture velocity requires an estimate of the azimuth as well as the slowness of the waves. The velocity structure must also be well known in order to correlate the observed slowness to a point on the fault plane.

Although the velocity structure off the coast in north-east Taiwan is not nearly as well known as in the Imperial Valley, the added dimension of the SMART 1 array allows estimation of the wave azimuths. By analyzing the accelerograms over narrow frequency bands, the high frequency scattered energy seen in chapter 5 can be separated from the lower frequency energy that is directly from the source region. Spudich and Cranswick made no attempt to separate the scattered energy from the coherent energy in their cross correlation technique.

Temporal changes in the Fourier phase differences between stations are examined through frequency-wavenumber spectra estimated as a function of time through the record. The change

in azimuth of the peak power is a direct measurement of the moving rupture front. The method requires an independent estimate of the rupture direction. This independent estimate of the rupture direction is found using the focal plane solution and the distribution of aftershock hypocenters given in chapter 3.

6.2 Time dependent Rupture Velocity Estimate

Frequency-wavenumber analysis was discussed in detail in chapter 4. Here, a local form of the Fourier transform is used to obtain local wavenumber spectra. The temporal Fourier transform at station j is written as

$$u_j(\omega) = \int_{-\infty}^{\infty} u_j(t) \; W^T(t-\eta_j) \; e^{-i\omega t} dt \qquad (6.2.1)$$

where $W^T(t-\eta_j)$ is a window function of length T centered at time $t=\eta_j$. The lag η_j is introduced because the recorded accelerograms are nonstationary. By applying the appropriate time delay to the recorded signal at each station, we can follow a particular seismic phase across the array. To follow a seismic phase, we assume a wavenumber then the time delay at each station is a function of the assumed wavenumber and is given by

$$\eta_j = \eta_0 - \frac{\vec{s}_j \cdot \vec{k}}{\omega}, \qquad (6.2.2)$$

where $\vec{s}_j$ is the position vector of station j relative to the center of the array and η_0 is the time delay at the central station C00. The time delay (beamsteering) is applied before estimating the cross-spectral matrix S so the estimate of the power in the high resolution method becomes

$$P^{HR}(\omega,\vec{k}) = \frac{1}{\vec{\zeta} \, \mathbf{S}^{-1}(\omega,\vec{k}) \, \vec{\zeta}^{T}} \qquad (6.2.3)$$

$$where \quad \mathbf{S}(\omega,\vec{k}) = \frac{u_j(\omega) \; \overline{u_k^T(\omega)}}{|u_j(\omega)| \; |u_k(\omega)|}.$$

A drawback of this technique is that it is computationally expensive because it requires estimating and inverting $\mathbf{S}(\omega,\vec{k})$ for each point in the wavenumber grid.

77

The time-dependent phase of the local Fourier transform in equation (6.2.1) can be estimated by complex demodulation.[1] The normalization used in equation (4.4.8) removes the amplitude dependence from the ω-k analysis so only a phase estimate is required. Complex demodulation gives an estimate of the instantaneous phase over each frequency band.

The elements of the time-dependent normalized cross-spectral matrix can be estimated by

$$S_{jk}(\omega,\vec{k},t) = \exp\{i(\phi_j(\omega,t+\eta_j) - \phi_k(\omega,t+\eta_k))\},\qquad(6.2.4)$$

where $\phi_j(\omega,t)$ is the instantaneous phase at station j found by complex demodulation. The variance of $S(\omega,\vec{k},t)$ can be reduced by averaging over the frequencies in the neighborhood of ω. The elements of the cross spectral matrix become

$$S_{jk}(\omega,\vec{k},t) = \frac{1}{2M+1} \sum_{l=-M}^{M} \exp\{i(\phi_j(\omega+\frac{2\pi l}{T},t+\eta_j) - \phi_k(\omega+\frac{2\pi l}{T},t+\eta_k)) W_l\}.\qquad(6.2.5)$$

As mentioned in chapter 4, 2M+1 should be greater than the number of stations in order to apply the statistics to the high resolution power spectrum, but the frequency resolution needed here requires a smaller M. This method of estimating the cross spectral matrix is used to run time dependent frequency-wavenumber analysis on the P and S waves. For each window selected, the azimuth of the peak power is measured yielding a time dependent azimuth $\theta(t)$ of the rupture front.

The time dependent rupture speed can be estimated from the time dependent azimuth $\theta(t)$ through simple geometry. Time at the source is denoted τ and time at the receiver is denoted t. Setting the center of coordinates at the array center, t and τ are related by

$$t = \tau + t_o + \frac{|\vec{x}(\tau)|-|\vec{x}(0)|}{c},\qquad(6.2.6)$$

where t_o is the propagation time from the hypocenter to the array center, $\vec{x}(\tau)$ is the position of the rupture front at time τ and c is the average wave velocity (P or S) at the source region. For example, a wave leaving the source at time τ_o from position $\vec{x}(\tau)+\vec{x}(0)$ arrives at the

---

[1] Complex demodulation is discussed in appendix A

center of the array at time t_o. Assuming a unilateral rupture in direction $\vec{r}$ and a laterally homogeneous velocity structure, then by simple geometry (figure 6.2)

$$\vec{x}(\tau) = \frac{|\vec{x}(0)| \, \sin(\theta(t)-\theta_o)}{\sin(\theta(t)-\theta_o+\phi)} \, \vec{r} + \vec{x}(0), \qquad (6.2.7)$$

$$where \quad \phi = \cos^{-1}\left[\frac{\vec{x}(0)\cdot\vec{r}}{|\vec{x}(0)|}\right].$$

The rupture direction $\vec{r}$ can be estimated from the aftershock hypocenter distribution given in chapter 3. For the case of a constant rupture direction, the relation between t and τ is

$$\frac{\partial t}{\partial \tau} = 1 + \frac{1}{c}\frac{\partial|\vec{x}(\tau)|}{\partial L}\frac{dL}{d\tau}, \qquad (6.2.8)$$

where $L(t)$ is the rupture length at time t and is given by

$$L(t) = \frac{|\vec{x}(0)| \, \sin(\theta(t)-\theta_o)}{\sin(\theta(t)-\theta_o+\phi)}. \qquad (6.2.9)$$

The frequency-wavenumber analysis gives the azimuth $\theta(t)$ as a function of time at the array. This azimuth must be converted to a function of time at the source $\theta(\tau)$. This can be accomplished numerically in a stepwise manner using the approximation

$$\tau_j = t_j - t_0 - \frac{1}{c}\{[|\vec{x}(0)|^2 + L_j^2 - 2|\vec{x}(0)|L_j\cos\phi]^{1/2} - |\vec{x}(0)|\}, \qquad (6.2.10)$$

where

$$L_j = \frac{|\vec{x}(0)| \, \sin(\theta_j - \theta_o)}{\sin(\theta_j - \theta_o + \phi)} \qquad (6.2.11)$$

and $L_o = 0$. The estimate of the rupture speed is simply

$$\gamma(\tau_i) = \frac{L_j - L_{j-1}}{\tau_j - \tau_{j-1}}. \qquad (6.2.12)$$

These approximations are used for both the P and S waves recorded by the SMART 1 array during the January 29, 1981 earthquake.

79

6.2.1 P Waves

For event 5, the S-P interval is approximately 4 seconds. The source depth was estimated at 25 km and for this depth there are no major seismic phase arrivals such as pP between the P and the S arrivals. This suggests that temporal changes in the phase differences during this 4 second window can be attributed to the moving source. As an example, the wavenumber spectra for the P wave portion estimated at 2 Hz is shown in figure 6.3. The azimuth of the peak power is 155°. In this manner, the azimuths are measured for a one second sliding time window with a 10% double cosine taper.

The azimuths of the peaks in the wavenumber spectra are plotted as a function of time in figure 6.4. The curve is for a 0.6 Hz frequency band centered at 2.5 Hz. The time-dependent azimuths expected for various constant rupture velocities are shown for reference in figure 6.4. During the first 3 seconds, the azimuth increases with time. The observed azimuths best follow the curve expected for a constant velocity of 2.5 km/sec. Beyond 3 seconds, the azimuths are not shown because they became much more scattered.

It should be noted that part of the difficulty in measuring the velocity of the moving rupture in this particular case, can be attributed to the high apparent velocity of the P waves (10 km/sec) and the small variation of the source azimuth for event 5 relative to SMART 1 (30°, see figure 3.4). The maximum array dimension is 4 km so that the maximum differential arrival time of the P waves is approximately 0.40 seconds. As the source moves through 30° to the end of the rupture, this differential time changes by only 0.05 seconds which is only 5 samples (sample interval = 0.01 sec). For most station pairs, the change in the differential time will be much less. These small changes are difficult to resolve even with the present digital system, so that the phase difference estimates used in the frequency-wavenumber analysis may contain significant amounts of noise that obscure the moving rupture.

6.2.2 S Waves

The S waves have a slower apparent velocity (2-3 km/sec) than the P waves and are

better suited for estimating the time-dependent rupture speed for this particular source-array geometry. In chapter 5, the S waves were seen to contain predominately coherent energy at frequencies up to 1.5 Hz. The S waves are studied for evidence of a moving source using frequency-wavenumber analysis over a 0.8 Hz frequency band centered at 1 Hz. The estimates of the 1 Hz S wave azimuths smoothed over 1 second windows are also shown in figure 6.5 as a function of time at the array. The time dependent azimuths expected for various constant rupture velocities are shown for reference in figure 6.5. The shaded region indicates one standard error.

There is a clear clockwise (east to west) rotation of the azimuth of the peak power. The time-dependent rupture-speed is estimated from these azimuths using equations (6.2.10-6.2.12) and is plotted in figure 6.6. The (two-sided) standard error is shown by the shaded region. This estimate of the standard error is a measure of the reading error and does not include systematic uncertainties due to the method itself. For this reason, the standard error in figures 6.5 and 6.6 are minimum estimates.

Figure 6.6 is a transformation of Figure 6.5 to show the variations observed in the rupture speed. The initial acceleration of the rupture cannot be resolved in this case; the rupture speed near to its initiation is approximately 2.5 km/sec. The rupture appears to decelerate sharply after 2 seconds but this deceleration is not significant according to the range of the standard error. After 3.5 seconds, the rupture accelerates up to 4.9 ± 0.5 km/sec. The mean is thus above the shear wave velocity of 3.5 km/sec. At 5.5 seconds, the rupture decelerates down to 1.6 km/sec. This deceleration may indicate the end of the rupture. Beyond 5.5 seconds, the S wave amplitudes at 1 Hz decrease rapidly and surface waves dominate the wavenumber spectra obscuring the end of the rupture. The total inferred rupture length obtained by integrating the rupture velocity is about 19 km. This rupture length is slightly less than the 25 km long rupture indicated by the aftershock distribution in chapter 3.

Super-shear rupture speeds have been proposed by other authors. A short episode of super-shear rupture velocity has been postulated for the 1979 Imperial Valley earthquake

(Archuleta, 1984; Spudich and Cranswick, 1984). The infered super-shear rupture speed shown in Figure 6.6, however, may be due to violations of the assumptions of the method. For example, the rupture direction $\vec{r}$ is assumed to be constant. If the fault has any bending then the infered rupture velocities may be in error. Similarly, the velocity structure is assumed to be laterally homogeneous, however, this is clearly not the case in north-eastern Taiwan. The crust thickens rapidly from the west to the east. Both of these effects could be responsible for the apparent super-shear rupture velocity.

This analysis demonstrates that strong motion array recordings can be used to follow the moving rupture along the fault. With allowances for the various uncertainties, the average rupture velocity of about 3.1 km/sec estimated from the array analysis is consistent with the average rupture velocity estimated using Brune's spectral model. The P and S waves gave consistent rupture velocity estimates for the first few seconds. The array analysis would have benefited from larger azmuthal variations of the source that could come about by a source closer to the array or by a larger source. For a closer source, the P wave spectra would probably be more useful than the S wave spectra because of the coherence at higher frequencies.
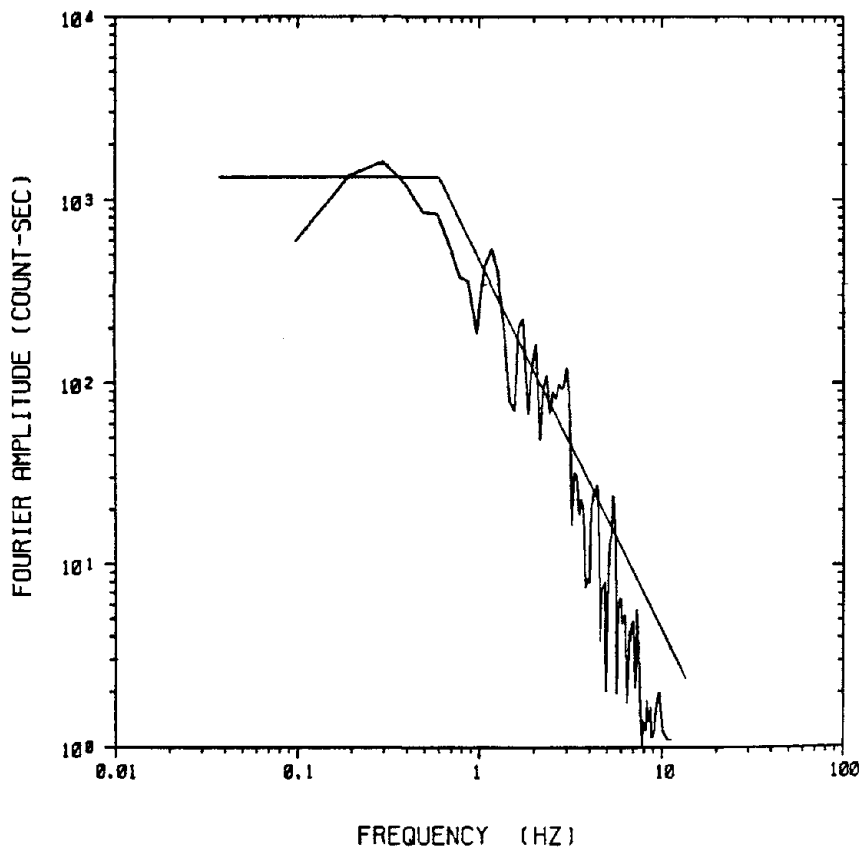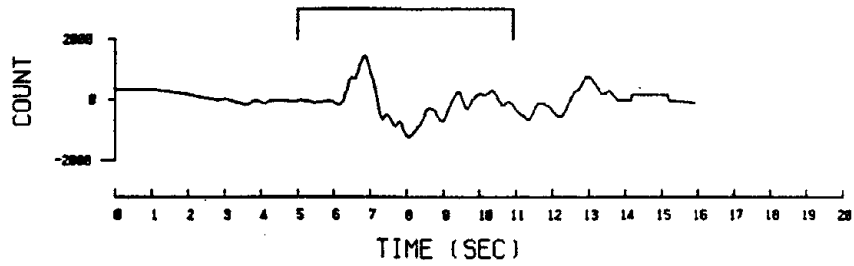
Figure 6.1 The Fourier displacement spectrum of the SH wave at station I-06. The two lines indicate the DC level and the high frequency asymptote.
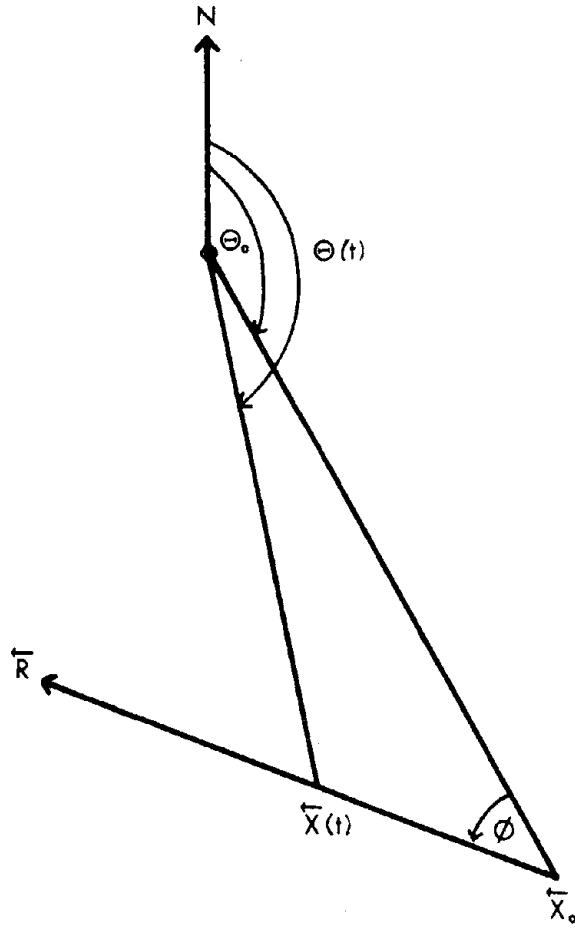
Figure 6.2 The fault-array geometry of event 5.
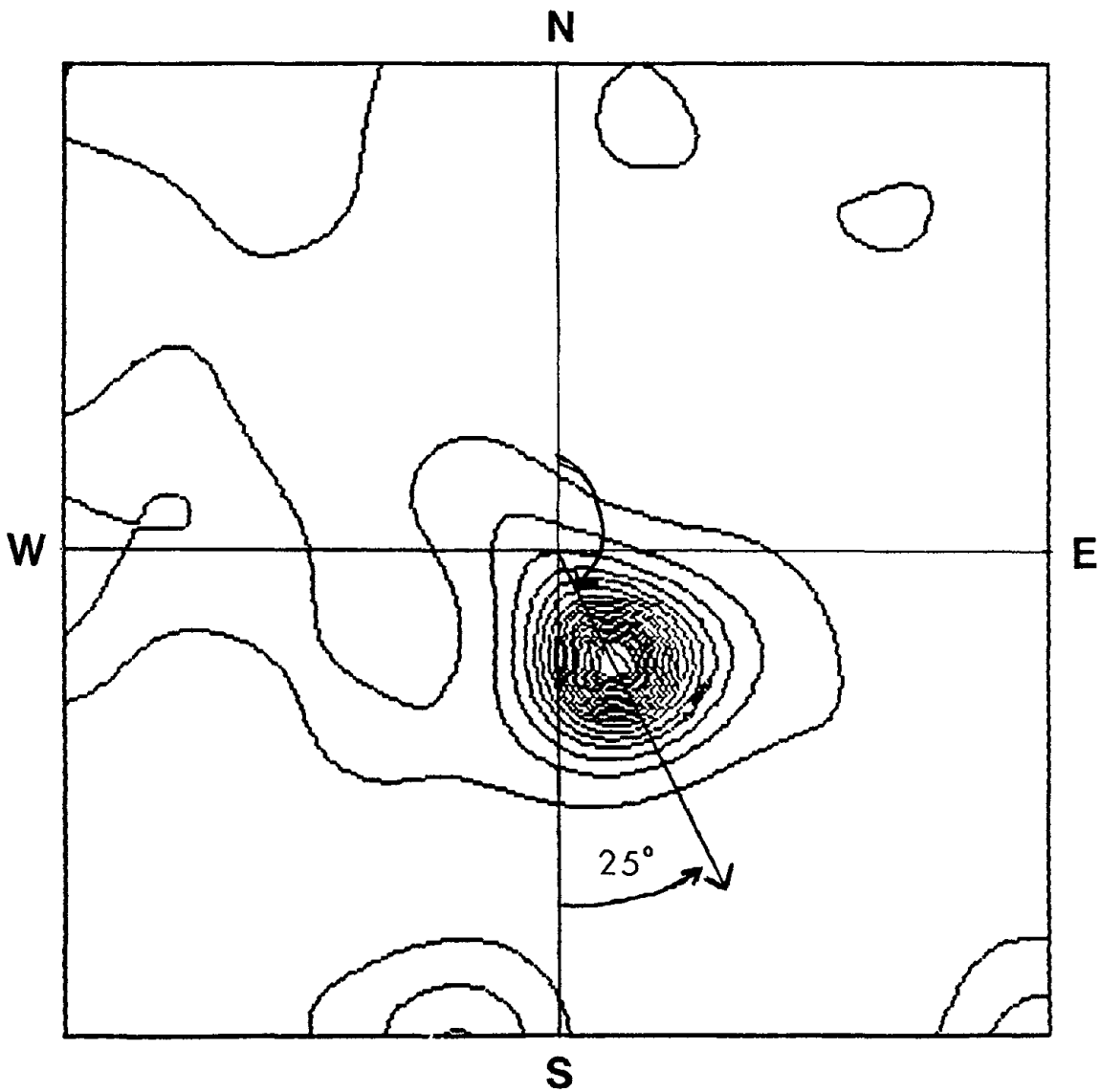
Figure 6.3 Contour plot of the wavenumber spectrum. The contours are in db down from the peak. In this case, the peak azimuth is at 155°.
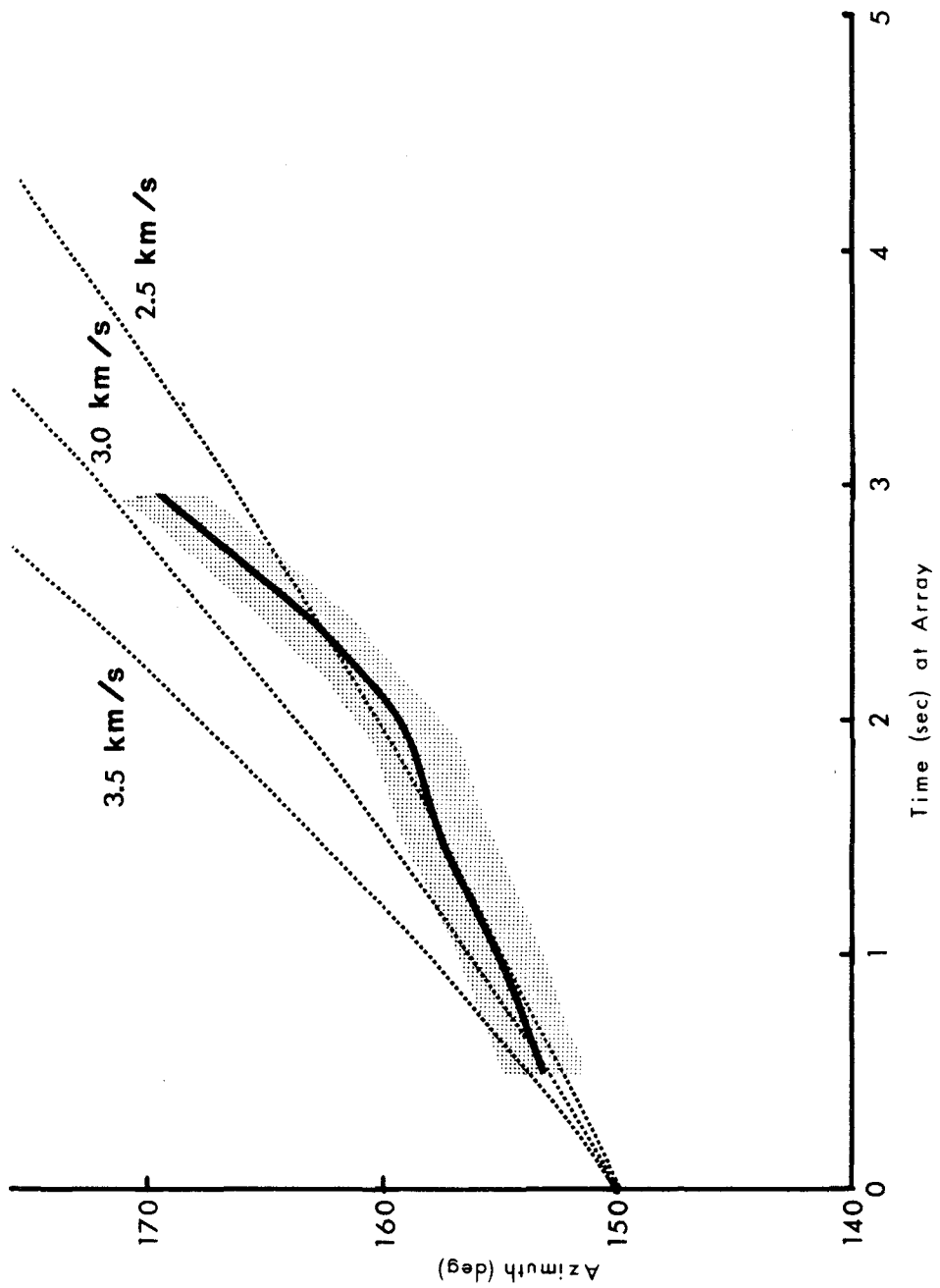
Figure 6.4 Time dependent azimuths estimated from the P wave spectra. The shaded region indicates one standard error and the dotted lines show the expected variation for various constant rupture velocities.
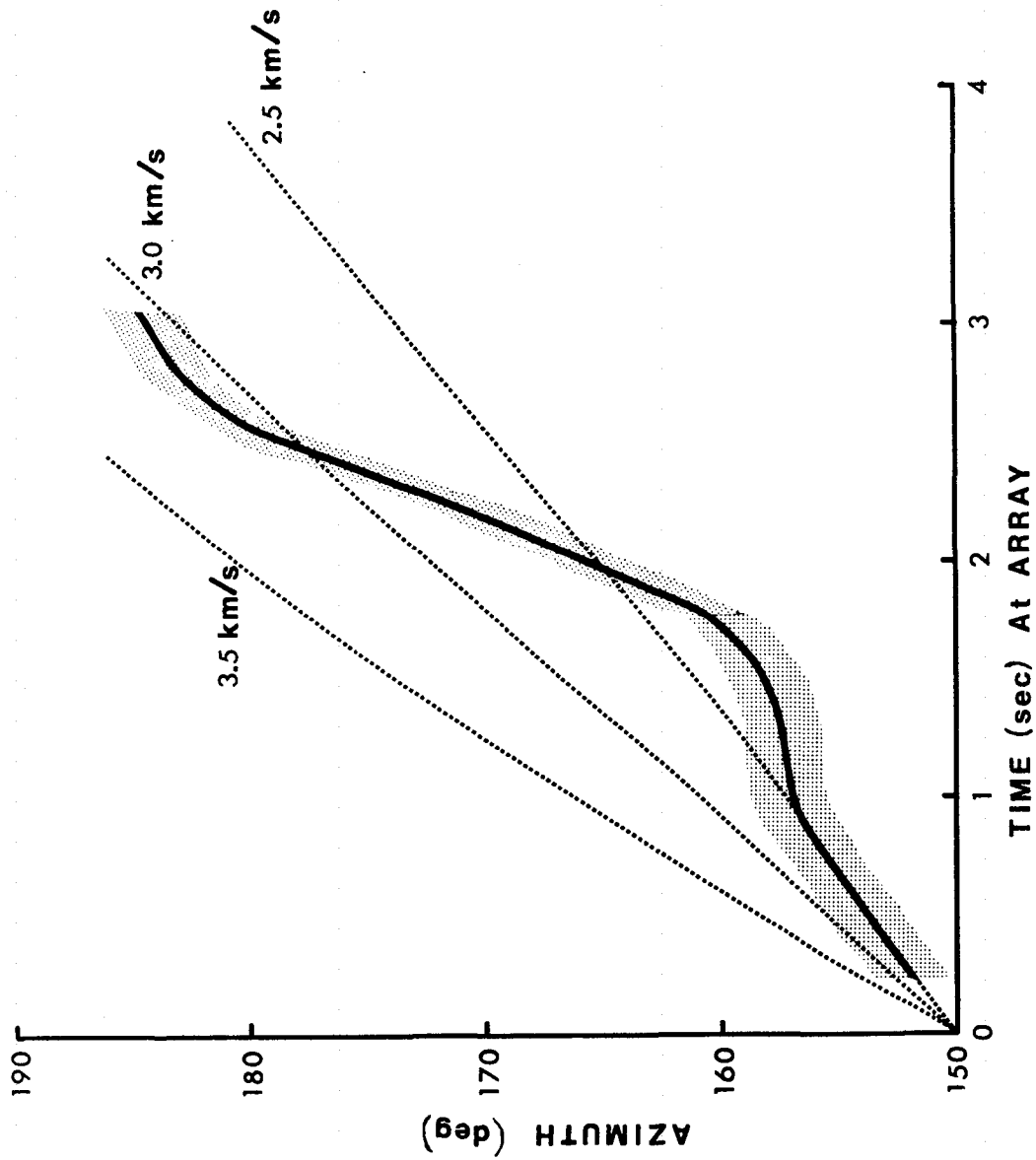
Figure 6.5 Time dependent azimuths estimated from the S wave spectra. The shaded region indicates one standard error and the dotted lines show the expected variation for various constant rupture velocities.
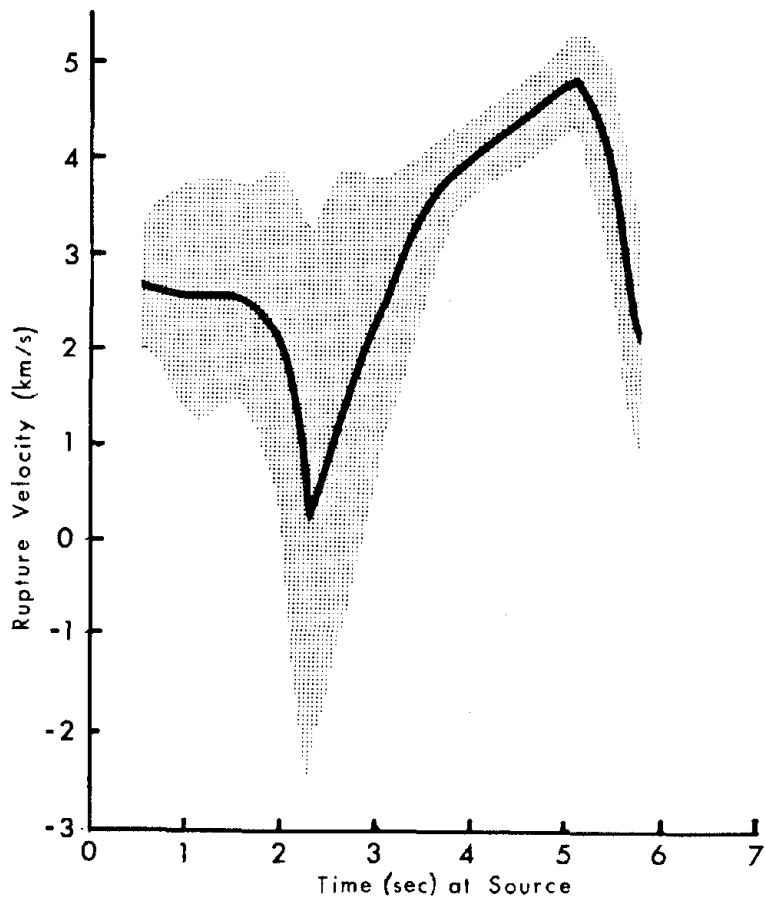
Figure 6.6 The time dependent rupture velocity estimated from the S wave azimuthal variation. The shaded region indicates one standard error. The initial acceleration of the rupture is not observed but the deceleration after 5.5 seconds may correspond to the stopping of the rupture.

88

Chapter 7

Implications of Wave Coherency to Engineering

7.1 Introduction

Response spectra are commonly used by engineers to approximate the response of a building to strong ground motion. In the seminal work, Housner *et al.* (1953) defined the value of the acceleration response spectrum at period T as the maximum acceleration of a simple damped oscillator with natural period T driven by the free-field acceleration. The spectrum defined in this manner describes the amplitude of the oscillator motion, but does not include information on its phase behavior. Nevertheless, for large structures, it is crucial to consider the phase because phase changes over short distances produce differential ground acceleration along the base of the structure. In chapter 5, the event 5 accelerograms were shown to contain coherent non-vertically propagating waves. Such a wave field produces systematic phase shifts in the accelerograms across the array leading to differential motion that reduces the average acceleration of a rigid base while exciting higher modes of a flexible structure.

Newmark suggested that a large structure with a rigid foundation would average the free-field accelerations over the foundation. It was expected that such averaging would lead to a reduction in the response spectrum (Newmark *et al.* 1978). Until recently, there was little observational verification of such an effect, but with strong motion array data now becoming available, the response spectrum for large structures can be estimated by spatial averaging of observed accelerograms from closely spaced instruments. For example, a spatial averaging technique was used by Smith *et al.* (1982) to estimate the reduction of the response spectrum along the El Centro differential array during the October 15, 1979 Imperial Valley earthquake.

89

The results were presented as a spectral ratio of the response spectrum from the spatially averaged accelerograms to the average response spectrum from the individual accelerograms. A similar measure was used by Bolt et al. (1984) for the SMART 1 array recordings. The method was generalized by Loh et al. (1982) to describe the effect of differential motion on higher modes of the structure as well as the fundamental mode.

7.2 The Response of Large Structures

Strong motion array data can be used to estimate the effect of spatial variations of the phasing of strong ground motion on large structures where multi-support inputs are appropriate. At a given node in the structure, the response due to the phase shifted inputs is divided by the mean response found using each of the individual support ground motions as rigid base inputs. This ratio, called the "dynamic response ratio" by Loh et al. (1982), indicates the effect of the spatial variation of the ground motion on the dynamic response of the structure. Consider a structure with N supports and M structural nodes. The total response of the structure can be separated into the quasi-static response and the dynamic response (Loh et. al., 1982). In this work, only the dynamic response is analyzed.

Assume that the normal modes of the structure are known and that for each structural mode, the weight or participation factor of the kth node to the lth input is also known. These weights, denoted w_{kl} will depend on the mass and stiffness of the structure as well as the structural mode. The equations of motion for the dynamic response of a discrete linear structural system are

$$\ddot{\vec{y}}(t) + 2\xi\omega\dot{\vec{y}}(t) + \omega^2\vec{y}(t) = \mathbf{W}\ddot{\vec{u}}(t) \qquad (7.2.1)$$

where ξ is the damping, ω is the natural frequency, $\vec{y}(t)$ is the M length vector of node displacements and $\ddot{\vec{u}}(t)$ is the N length vector of support input accelerations.

In this chapter, the special case of just one structural node with N inputs is considered. The dynamic response of the structure satisfies the differential equation

$$\ddot{r}(t) + 2\xi\omega\dot{r}(t) + \omega^2 r(t) = -w\cdot\ddot{u}(t) \qquad (7.2.2)$$

Let $R_{\xi,T}(t)$ be the unit impulse response of a single degree of freedom oscillator with period T and damping ξ. The dynamic acceleration response is usually characterized by the maximum of $\ddot{r}(t)$. The acceleration response spectrum for equation (7.2.2) is denoted $SA(\xi,T)$ and is given by

$$SA(\xi,T) = \max_{t} |R_{\xi,T}(t) * \vec{w}\cdot\vec{u}(t)|, \qquad (7.2.3)$$

where * indicates a convolution. This response spectrum is compared to the response spectra obtained by using rigid base inputs.

Using the lth input at all of the support nodes, the equation of motion becomes

$$\ddot{r}_l(t) + 2\xi\omega\dot{r}_l(t) + \omega^2 r_l(t) = (\sum_{k=1}^{N} w_k)\, \ddot{u}_l(t). \qquad (7.2.4)$$

Let $SA_l(\xi,T)$ be the acceleration response spectrum for the ground acceleration $\ddot{u}_l(t)$. Then the response spectrum for equation (7.2.4) is $(\sum_{k=1}^{N} w_k)\, SA_l(\xi,T)$ and the mean response spectrum of all the inputs is given by

$$\overline{SA}(\xi,T) = (\sum_{k=1}^{N} w_k)\, \frac{1}{N}\sum_{l=1}^{N} SA_l(\xi,T). \qquad (7.2.5)$$

The dynamic response ratio defined by Loh et. al., 1982, is given by

$$\Phi^d(\xi,T) = \frac{SA(\xi,T)}{\overline{SA}(\xi,T)}. \qquad (7.2.6)$$

Substituting for the response spectra, equation (7.2.6) becomes

$$\Phi^d(\xi,T) = \frac{\max\limits_{t} |R_{\xi,T}(t) * \vec{w}\cdot\vec{u}(t)|}{(\sum\limits_{k=1}^{N} w_k)\, \frac{1}{N}\sum\limits_{l=1}^{N} SA_l(\xi,T)} \qquad (7.2.7)$$

91

This ratio is influenced by both differential amplification of the ground motion due to site effects and differential phasing of the ground motion. The differential phasing may be due to either incoherent waves or non-vertically propagating waves or local site effects. To simplify the interpretation of the dynamic response ratio, site amplification effects are removed by normalizing each support acceleration $u_i(t)$ by the response $SA_i(\xi,T)$. With this normalization, the dynamic response ratio becomes

$$\tilde{\Phi}^d(\xi,T) = \frac{\max_t |\sum_{i=1}^N w_i [R_{\xi,T}(t) * \frac{\ddot{u}_i(t)}{SA_i(\xi,T)}]|}{(\sum_{k=1}^N w_k)}. \tag{7.2.8}$$

In the following sections, the dynamic response ratio given by equation (7.2.8) is evaluated for various structural modes and support spacings using the SMART 1 recordings from events 5 and 24 as ground motion inputs at the supports.

7.2.1 Rigid Structures

Consider the fundamental structural mode $(w_k)=1$ of a rigid structure. The dynamic response ratios for this mode using the transverse component of acceleration from event 5 with N=2 for stations pairs C00-I06 and C00-I03 are shown in figures 7.1a-b. The station spacing is 200 meters. A reference line is drawn to indicate the dynamic response ratio that results from a simple plane wave propagating across the array with an apparent velocity of 4 km/sec and the azimuth determined from the wavenumber spectra (see figure 5.9) in chapter 5. The line is not fit to the data and is included just for reference. Stations C00 and I03 are aligned nearly perpendicular to the direction of propagation while stations C00 and I06 are aligned nearly parallel to the direction of propagation (figure 7.2). The difference in alignment accounts for the difference in the two reference lines in figures 7.1a and 7.1b.

The data from station pair C00-I06 show a substantially larger reduction in the response spectrum than those data from station pair C00-I03. The dynamic response ratio is approximately 0.70 at 5 Hz for supports at C00 and I06 while the ratio is approximately 0.94 at 5 Hz

for supports at stations C00 and I03. If the phase shifts are due to incoherent waves, then the dynamic response ratio across 200 meters will be independent of support orientation. The large disparity in the ratios between the two station pairs indicates that most of the reduction is due to coherent horizontally propagating waves and not to incoherent waves. The radial component of ground motion exhibits this same effect (figures 7.3a-b).

At frequencies above 6 Hz, the dynamic response ratio estimates in figures 7.1 and 7.3 deviate from the curves predicted by simple plane waves. At frequencies above 6 Hz, the dynamic response ratio estimates in figures 1 and 3 deviate from the curves predicted by simple plane waves. The recorded accelerograms have little energy at frequencies above 6 Hz which causes the motion of the oscillator to be similar to the input motion. the long period energy in the input motion tends to increase the estimates of the fundamental mode of the dynamic response ratio.

As a comparison with the results from Taiwan, the dynamic response ratio was also estimated from equation (7.2.8) using the El Centro differential array data recorded during the 1979 Imperial Valley earthquake. It was found that, for a 205 meter spacing, the dynamic response ratio is 0.8-0.9 at 5 Hz. The Imperial fault ruptured past the differential array, however, Spudich and Cranswick (1984) give evidence that the largest accelerations are from a region 25-30 km northwest of the mainshock epicenter. This region is at an azimuth that makes an angle of approximately 40° with the array axis. Assuming this azimuth, then the observation that the spectral ratio at El Centro falls between the values from the two station pairs of the SMART 1 array is as expected from a purely geometrical argument. The consistency between estimates of the dynamic response ratio found in Northeast Taiwan and in Imperial Valley, California, give an initial indication that the dynamic response ratios from SMART 1 can be applied at other soil sites.

7.2.2 Flexible Structures

In the previous section, the fundamental mode or "in-phase" motion was analyzed. In this section the "out-of-phase" motion is considered. This corresponds to the case $w_1=1, w_2=-1$

($\gamma=-1$ in the notation of Loh *et al.* 1982). Large flexible structures such as bridges have long natural periods (up to 5-10 seconds), so rather than consider the dynamic response ratio as a function of frequency as in section 7.2.1, the dynamic response ratio is considered as a function of support spacing at a single frequency. The dynamic response ratio at a period of 1 second for station pairs aligned approximately parallel to the wave propagation is shown in figure 7.4a. Following a similar approach as before, a reference curve indicating the dynamic response ratio that results from a simple plane wave propagating across the array is also plotted.

The observed ratios follow the general shape of the curve. The effect of random energy is to shift the values from the two extremes values of 0 and 1 toward the center. This increases the ratio at short separations and decreases the ratio at separations close to one half of a wavelength.

Figure 7.4b shows the dynamic response ratio at a period of 1 second for station pairs aligned within 15° of perpendicular to the wave propagation. For a simple plane wave, these ratios should be less than the ratios found for stations aligned parallel to the direction of propagation. From 600 meters to 1000 meters separations, the ratios in 7.4b are lower than the ratios in 7.4a but at the small separations, there is no significant difference between the two plots. At a separation of 200 meters, both station alignments give ratios between 0.2 and 0.3.

The analysis is repeated for a 3 second period structure (figures 7.5a-b) to compare with the 1 second period results . For a constant velocity, the wave length increases with period leading to smaller phase shifts between supports from a plane wave so the reference curves in figures 7.5a-b are lower than in figures 7.4a-b. As expected the ratios estimated for the 3 second period structure are lower than for the 1 second period structure. As seen previously for the 1 second period dynamic response ratios, the ratios for the supports aligned almost perpendicular to the wave propagation are less than for the parallel alignment of supports, however, the difference disappears at separations less than 300 meters. At a separation of 200 meters, parallel alignments at 1 and 3 second periods give a dynamic response ratio of 0.10 to 0.20.

Finally, for comparison with the shallow focus earthquake of January 29, 1981, the preceding analysis is repeated for event 24 (see figure 2.3 and table 2.2). This magnitude 7.2 earthquake ($\Delta=75$ km) triggered most of the inner ring stations so that some 100 meter separation measurements can be made. The dynamic response ratio at 1 Hz are shown in figures 7.6a-b. These data show the same general features as for event 5. At separations greater than 500 meters, the ratios for the transverse support alignment are lower than for the radial support alignment. At separations between 600 and 1000 meters, the dynamic response ratio for event 24 are clustered between 0.6 and 0.95 while for event 5 the ratios are between 0.4 and 0.9. In contrast, at a separation of 200 meters, the dynamic response ratio for event 24 is between 0.15 and 0.3 for both the parallel and perpendicular support alignments which is slightly less than the ratios found for event 5. The ratios for event 24 are closer to the reference lines than for event 5. This difference in dynamic response ratios is due to the different epicentral distances from the array to the two events. The epicentral distance from from the SMART 1 array to event 24 is 75 km compared to an epicentral distance of 30 km from event 5. At larger distances there is less variation in the waveforms observed across the array and the plane wave approximation is more appropriate.

7.3 A Seismic Response Phase Spectrum

The estimation of the dynamic response ratio in section 7.2 involves the complete time series at the supports for each support grouping and structural mode. The dynamic response ratio defined in equation (7.2.8) is a measure of the phase difference between the oscillator time series at the supports. The estimation can be greatly simplified by defining a response phase spectrum analogous to the Fourier phase spectrum. The dynamic response ratio will then depend only on the difference in the response phases between supports rather than the complete oscillator time series at each support.

The motion of a simple damped harmonic oscillator $y(t)$ satisfies the differential equation

$$\frac{d^2y(t)}{dt^2} + 2\xi\omega_o\frac{dy(t)}{dt} + \omega_o^2 y(t) = -\frac{d^2u(t)}{dt^2} \qquad (7.3.1)$$

where ξ is the damping and ω_o is the natural frequency. The oscillator motion $y(t)$ has dominant frequency $\omega'=\omega_o\sqrt{1-\xi^2}$.

In the formulation of Housner *et al.* (1953), the oscillator motion is described by its maximum amplitude. In order to study the phasing, the complete oscillator time history needs to be analyzed. Some examples of time histories of oscillators driven by the event 5 accelerograms recorded at station C00 are shown in figure 7.7. At high natural frequencies, the oscillator motion is similar to the input motion.

The single dominant frequency of the oscillator motion suggests that an appropriate mathematical model for the complete vibrational motion is

$$y_{\omega,\xi}(t) = A_{\omega,\xi}(t) \cos(\omega't + \psi_{\omega,\xi}(t)) + \epsilon_{\omega,\xi}(t) \tag{7.3.2}$$

where $y_{\omega,\xi}(t)$ is the time history of the oscillator with natural frequency ω and damping ξ, $A_{\omega,\xi}(t)$ and $\psi_{\omega,\xi}(t)$ are the instantaneous amplitude and phase respectively and $\epsilon_{\omega,\xi}(t)$ is the residual of the fit. If $A_{\omega,\xi}(t)$ and $\psi_{\omega,\xi}(t)$ are smooth functions in t, they can be estimated by the complex demodulation method. Complex demodulation is essentially narrow-band filtering that is realized by low-pass filtering the series $y_{\omega,\xi}(t)e^{i\omega't}$. The amplitude and phase of the resulting series give estimates for $A_{\omega,\xi}(t)$ and $\psi_{\omega,\xi}(t)$. A more detailed description of the complex demodulation algorithm is given in Appendix A.

The appropriate corner frequency of the low-pass filter used in the complex demodulation is determined by examining the oscillator transfer function. An example of such a transfer function is shown in figure 7.8. If the bandwidth of the transfer function is taken as its width at $\frac{1}{e}$ of the maximum, then for damping $\xi < 0.2$, the bandwidth is approximately

$$\Delta\omega \approx 2(1+0.7\xi)\omega. \tag{7.3.3}$$

A corner frequency setting of $\omega_c = \frac{\Delta\omega}{2}$ in the low-pass filter will pass this same frequency band. This filtering is used in the following analysis.

The form of equation (7.3.2) suggests that the response amplitude and phase be defined in terms of $A_{\omega,\xi}(t)$ and $\psi_{\omega,\xi}(t)$ respectively, but this would be inconsistent with current

engineering practice. The response (amplitude) spectrum is the maximum of the sequence $|y_{\omega,\xi}(t)|$ over t so it includes the residual term $\epsilon_{\omega,\xi}(t)$. Therefore, in this development, the acceleration response spectrum at frequency ω and damping ξ is defined by

$$SA_\xi(\omega) = \max_t |A_{\omega,\xi}(t)\cos(\omega't+\psi_{\omega,\xi}(t)) + \epsilon_{\omega,\xi}(t)|. \qquad (7.3.4)$$

If the energy at frequencies other than ω' is small (e.g. $\dfrac{\epsilon_{\omega,\xi}(t)}{A_{\omega,\xi}(t)} < < 1$) then $SA_\xi(\omega)\approx A_{max}$, where A_{max} is the maximum of $A_{\omega,\xi}(t)$. If there is significant energy in $y_{\omega,\xi}(t)$ at frequencies far from ω', then the response spectrum may be much larger than A_{max}. As an illustration, the ratio $SA_\xi(\omega)/A_{max}$ found for the accelerograms in figure 7.7 is shown in figure 7.9. As expected, at frequencies where there is significant power in the free-field accelerogram, (in this case 0.3 - 5 Hz, see figure 7.10), the residual $\epsilon_{\omega,\xi}(\omega)$ is negligible and $SA_\xi(\omega)\approx A_{max}$. At frequencies outside of this range, the residual in the fit of the demodulate becomes significant and $SA_\xi(\omega)$ is more than twice A_{max}.

If $SA_\xi(\omega)\approx A_{max}$, then equation (7.3.2) suggests that the response phase $\Psi_\xi(\omega)$ be defined as

$$\Psi_\xi(\omega) = \psi_{\omega,\xi}(\tau), \qquad (7.3.5)$$

where τ is the time at which $|y_{\omega,\xi}(t)|$ is a maximum. Such a response phase is not a complete description of the phasing, but it is the "most important" phase since it is associated with the maximum amplitude. What is crucial is that this definition of the response phase spectrum is consistent with the response (amplitude) spectrum currently used by engineers.

The form of equation (7.3.2) has been tested by examining the accelerograms recorded during event 5. The Fourier amplitude spectrum shown in figure 7.10 is for the accelerogram recorded by the EW component at station C00. Typically, acceleration spectra have a low frequency corner and a high frequency corner shown here by f_l and f_u. These two frequencies conveniently divide the spectrum into three parts; two regions with low power and one region with high power. Within each region, the oscillator time histories have similar characteristics. Figures 7.11a-c show the oscillator time histories $y(t)$ and the demodulates of equation (7.3.2)

97

for frequencies f=0.3, 3.0 and 10 Hz respectively. The fits are much closer for the two lower frequencies than for the high frequency case. This is because of the relatively large residual term in the high frequency portion of the spectrum compared to the rest of the spectrum.

The Fourier spectra of the oscillator time histories from figures 7.11a-c and the associated residual terms $\epsilon_{\omega,\xi}(t)$ are shown in figures 7.12a-c. In each case, the upper plot is the spectrum of the oscillator time history and the lower plot is the spectrum of the residual term. At frequencies shorter than ω, the amplitude of the residual is approximately equal to the amplitude of the input accelerogram. For f=3.0 and f=0.3 Hz, the spectrum of the oscillator time history is dominated by a single large peak. The spectra of the residual show that in both cases, the large peak has been fit by complex demodulation and is no longer present. For the third case, f=10 Hz, the Fourier spectrum of the oscillator time history does not have a single large peak. This property is due to the small amplitude of the input accelerogram at the resonant frequency. The energy at the resonant frequency has been fit by complex demodulation, but there are still many other peaks at lower frequencies with comparable amplitudes.

The conclusion is that the suggested model may not fit well for resonant frequencies above the high frequency corner f_u, but the model is acceptable for resonant frequencies below f_u.

Estimation of the dynamic response ratio can be simplified if the oscillator time history $y_{\omega,\xi}(t)$ is approximated by a cosinusoid with amplitude and phase given by the response amplitude and phase. The approximation is

$$y_{\omega,\xi}(t) \approx SA_{\xi}(\omega) \cos(\omega't + \Psi_{\xi}(\omega)). \tag{7.3.6}$$

This approximation becomes exact if $\psi_{\omega,\xi}(t)$ is a constant and $\epsilon_{\omega,\xi}(t)=0$. For real data, these conditions do not occur, but as shown in the last section, equation (7.3.4) gives a good approximation to the largest accelerations at frequencies below f_u.

The estimate of the dynamic response ratio using the above approximation is found by averaging two or more phase shifted cosinusoids with unit amplitude. For n input points, the

98

dynamic response ratio given in equation (7.2.8) becomes

$$\Phi^d(\omega) = \frac{\displaystyle\max_t \ |\ \sum_{k=1}^{n} w_k \cos(\omega' t + \Psi_{\xi}^k(\omega))\ |}{\displaystyle\sum_{k=1}^{n} w_k} \tag{7.3.7}$$

where $\Psi_{\xi}^k(\omega)$ is the response phase at input k. Evaluating the maximum over time gives

$$\Phi^d(\omega) = \frac{[(\sum_{k=1}^{n} w_k)\cos(\Psi_{\xi}^k(\omega))^2 + (\sum_{k=1}^{n} w_k \sin(\Psi_{\xi}^k(\omega))^2]^{\frac{1}{2}}}{\displaystyle\sum_{k=1}^{n} w_k}. \tag{7.3.8}$$

The $\Phi_j^d(\omega)$ can be smoothed over narrow frequency bands. With such smoothing over $2M+1$ frequencies, the mean and variance of the dynamic response ratio are estimated by

$$\overline{\Phi_j^d(\omega)} = \frac{1}{2M+1} \sum_{k=-M}^{M} \Phi_j^d(\omega+k\Delta f), \tag{7.3.9}$$

$$Var\,[\Phi_j^d(\omega)] = \frac{1}{2M} \sum_{k=-M}^{M} (\Phi_j^d(\omega+k\Delta f)-\overline{\Phi_j^d(\omega)})^2 \tag{7.3.10}$$

where Δf is the frequency step used in the smoothing. The dynamic response ratio is limited to the range [0,1] which may truncate one side of the variance if the mean estimate is near either extreme value.

Equation (7.3.8) uses the response phase spectra which are calculated only once for each station. Estimating the dynamic response ratio for multiple input points or various modes of the structure foundation only requires changing the weights w_k.

7.3.1 Application to Recorded Ground Motions

The estimate of the dynamic response ratio using equation (7.3.8) is compared to the dynamic response ratio found in section 7.2.1. The first step is to estimate the response phase spectra. These estimates for the accelerograms from event 5 at stations C00 and I06 are shown in figure 7.13a-b. To estimate the dynamic response ratio at 3 Hz, the response phases are read from figures 7.13a-b. In this case the phases are $\Psi_{\xi}^1(\omega) = 4.1$ radians and $\Psi_{\xi}^2(\omega) = 3.1$ radians. The phase difference is 1.0 radians and using the weights $w_k=1$ for a rigid structure as before,

the dynamic response ratio is 0.88. This compares with a value of 0.89 using equation (7.2.8) (see figure 7.1). The dynamic response ratio estimates calculated using equation (7.3.9) are shown in figure 7.14a by the circles and the estimates found using equation (7.2.8) are shown by the line. At frequencies below 6 Hz, the ratios estimated using the response phases are quite close to the ratios estimated using equation (7.2.8), while above 6 Hz, the small amplitude in the input accelerograms which resulted in poor fit of the demodulate (see figure 7.11) lead to a poor agreement between the two ratio estimates.

A poor fit of the demodulate is characterized by a large uncertainty in the phase estimates. Large phase uncertainties lead to large uncertainties on the dynamic response ratio. In figure 7.14a, there is a large increase in the standard error of the dynamic response ratio above 5 Hz indicating that these estimates are not as reliable as the estimates at the lower frequencies.

The dynamic response ratio calculated using inputs at station C00 and I03 is shown in figure 7.14b. Except for three points that have very large standard errors, the ratios estimated using the response phase spectra are again quite close to the ratios estimated using equation (7.2.8). In this case, the two methods for estimating the ratio agree at frequencies up to 10 Hz. Figures 7.14a-b indicate that the response phase can be used to quickly construct reasonable estimates of the dynamic response ratio.
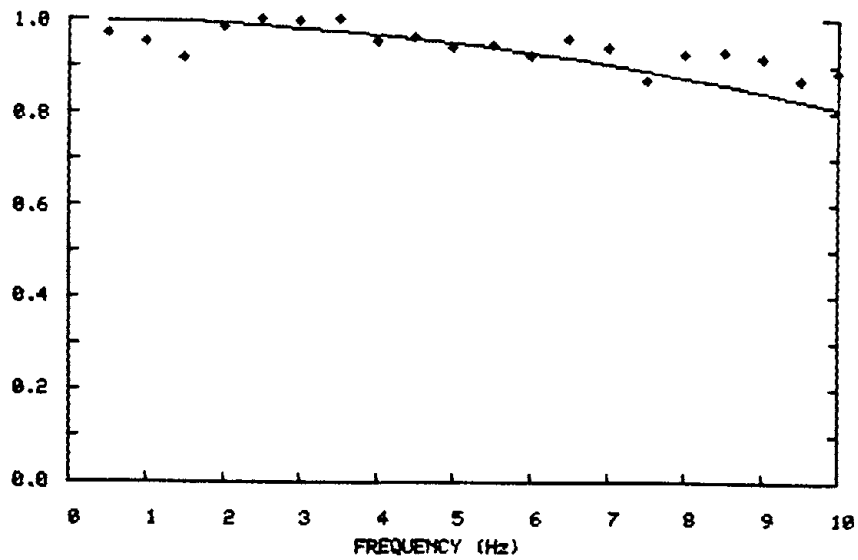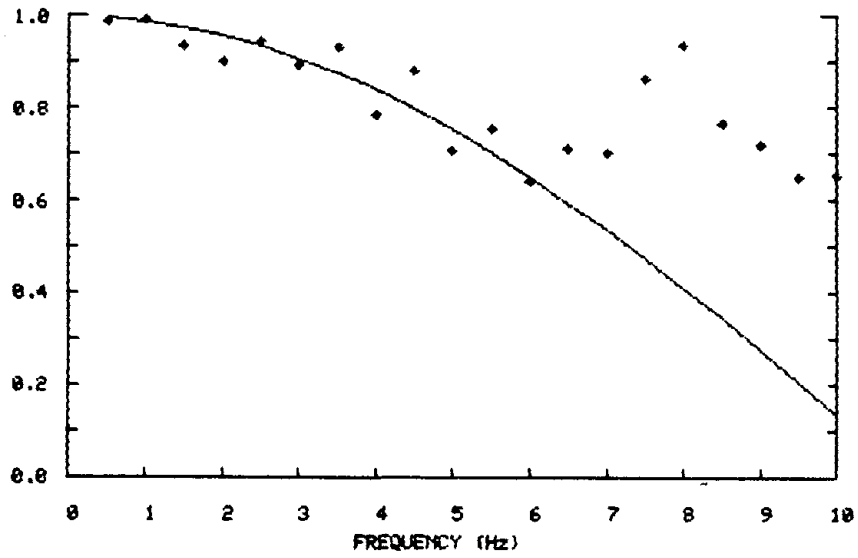
Figure 7.1 The fundamental mode (in-phase motion) dynamic response ratio for 200 meter support spacing using the transverse component of acceleration from event 5. The diamonds are the estimated ratios and the line gives the ratio expected for a simple plane wave propagating from the source region.
(a) Station pair C00-I06. (b) Station pair C00-I03.

101
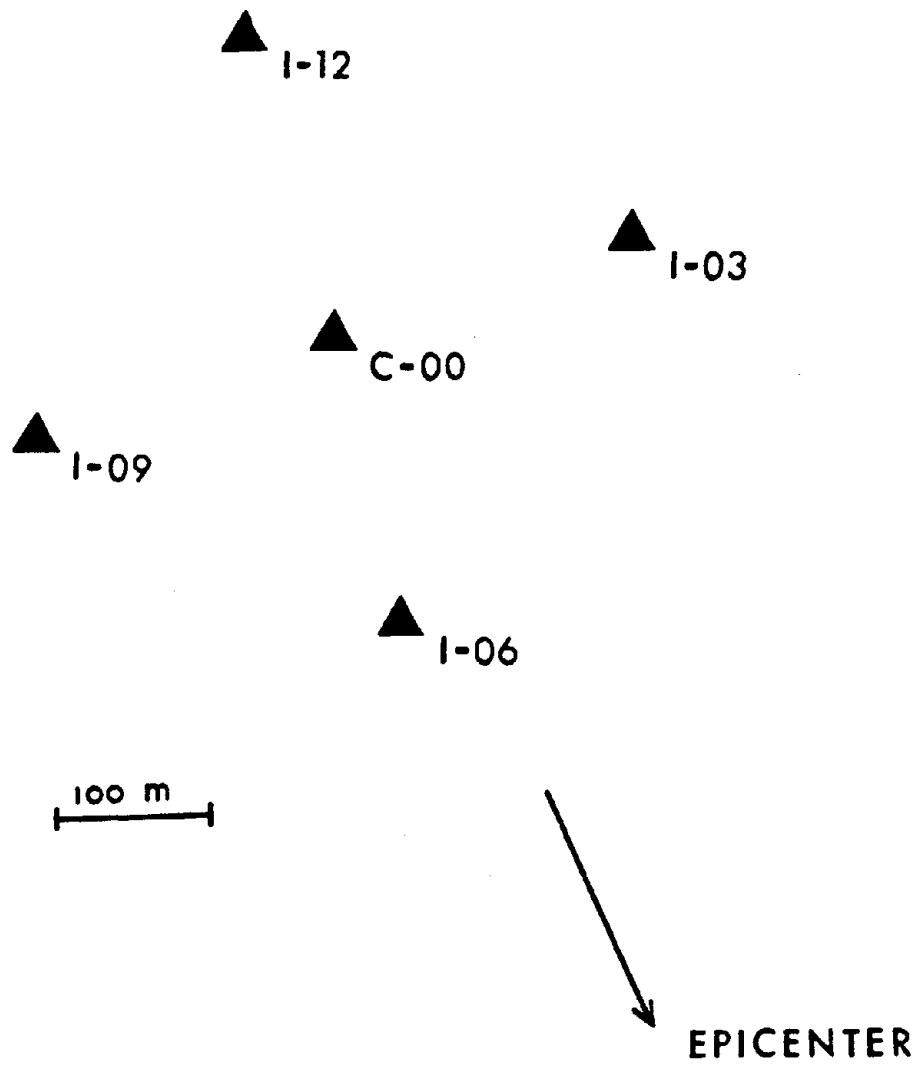
Figure 7.2 The alignment of the inner ring stations with respect to the epicenter of event 5. Stations I06-C00-I12 are aligned nearly parallel to the epicentral direction while stations I03-C00-I09 are aligned nearly perpendicular to the epicentral direction.
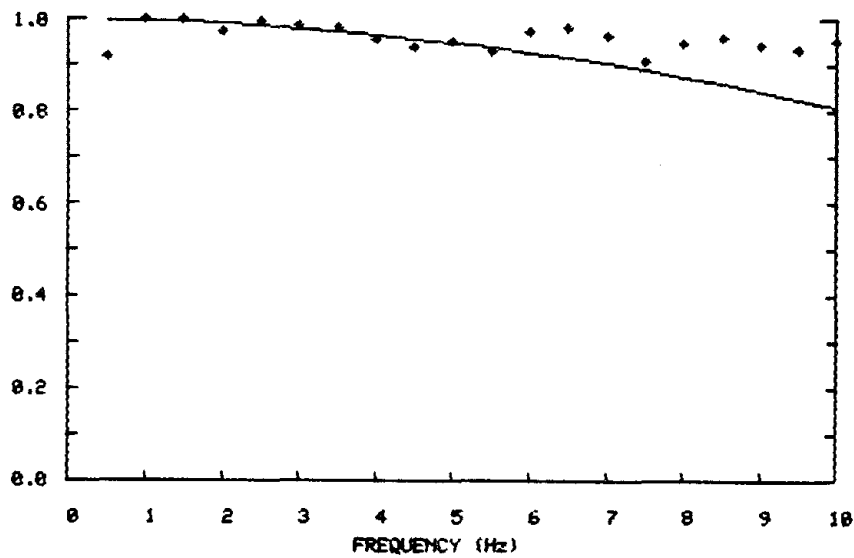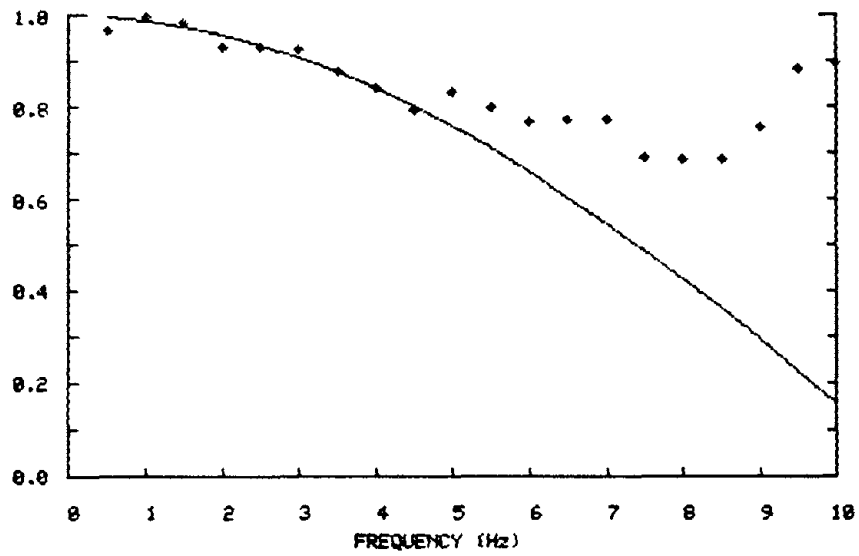
Figure 7.3 The fundamental mode (in-phase motion) dynamic response ratio for 200 meter support spacing using the radial component of acceleration from event 5. The diamonds are the estimated ratios and the line gives the ratio expected for a simple plane wave propagating from the source region.
(a) Station pair C00-I06. (b) Station pair C00-I03.
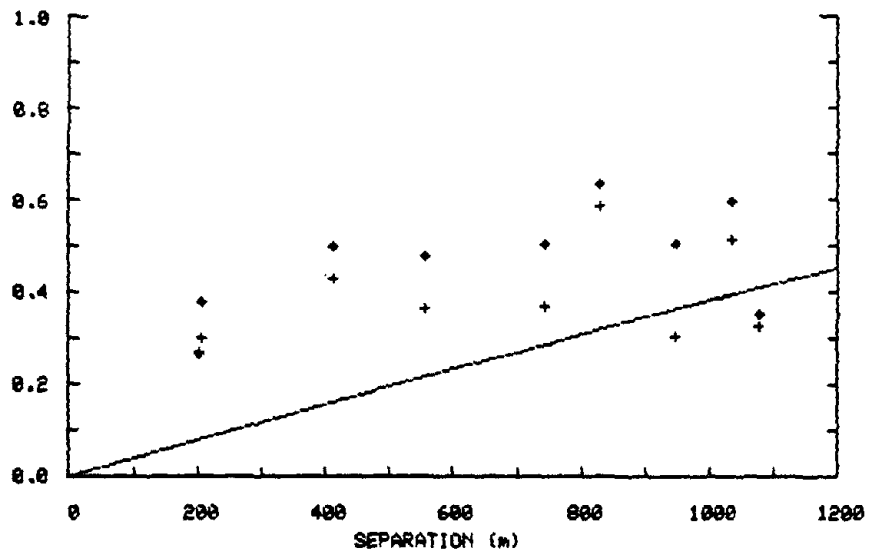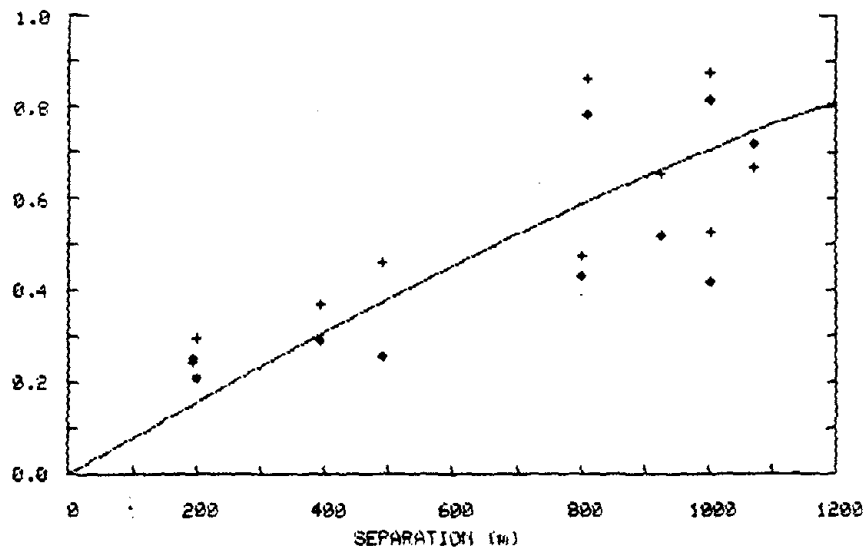
Figure 7.4 The out-of-phase dynamic response ratio at a period of 1 second using accelero-grams from event 5. The diamonds indicate the radial component of acceleration and the crosses indicate the transverse component of acceleration. The line gives the ratio expected for a simple plane wave propagating from the source region.
(a) Station pair C00-I06. (b) Station pair C00-I03.
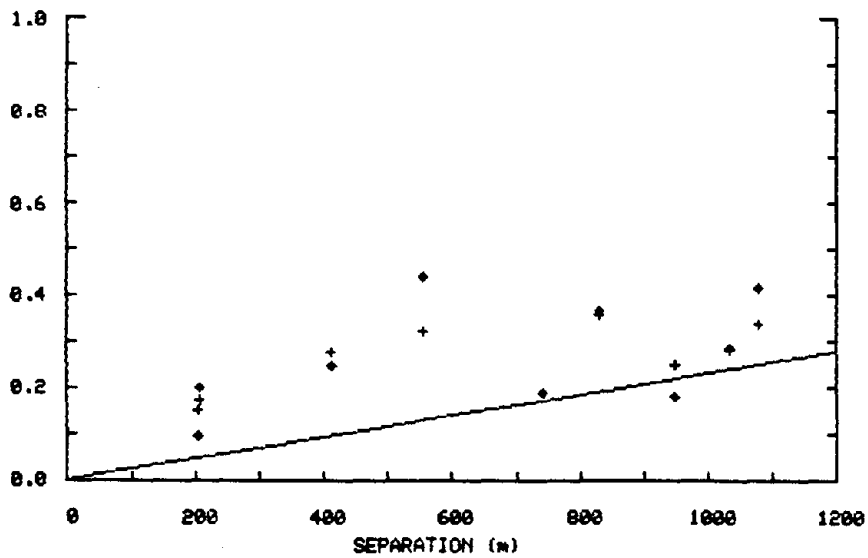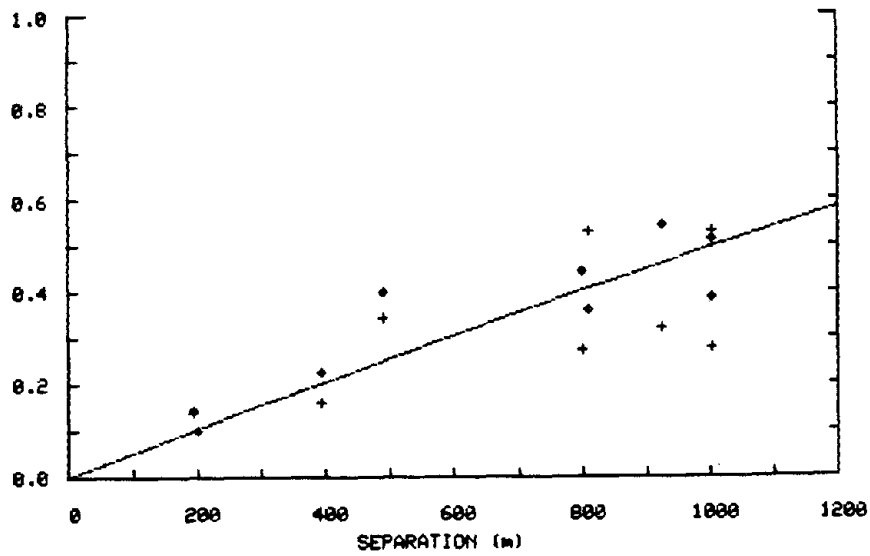
Figure 7.5 The out-of-phase dynamic response ratio at a period of 3 seconds using accelerograms from event 5. The diamonds indicate the radial component of acceleration and the crosses indicate the transverse component of acceleration. The line gives the ratio expected for a simple plane wave propagating from the source region.
(a) Station pair C00-I06. (b) Station pair C00-I03.

105
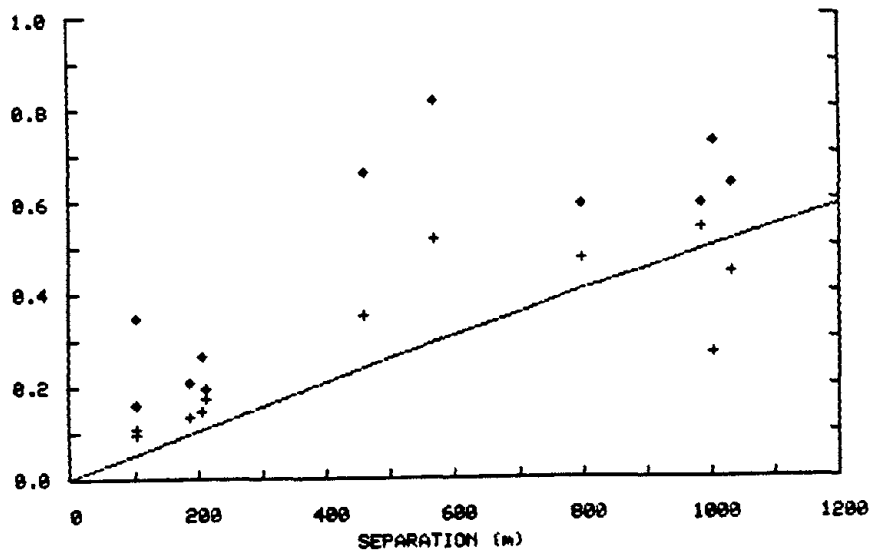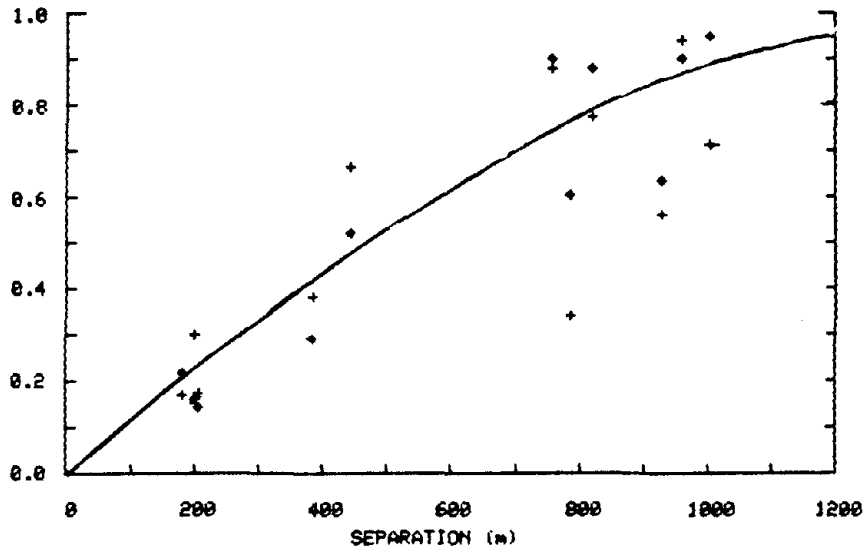
Figure 7.6 The out-of-phase dynamic response ratio at a period of 1 second using accelerograms from event 24. The diamonds indicate the radial component of acceleration and the crosses indicate the transverse component of acceleration. The line gives the ratio expected for a simple plane wave propagating from the source region.
(a) Station pair C00-I06. (b) Station pair C00-I03.

106
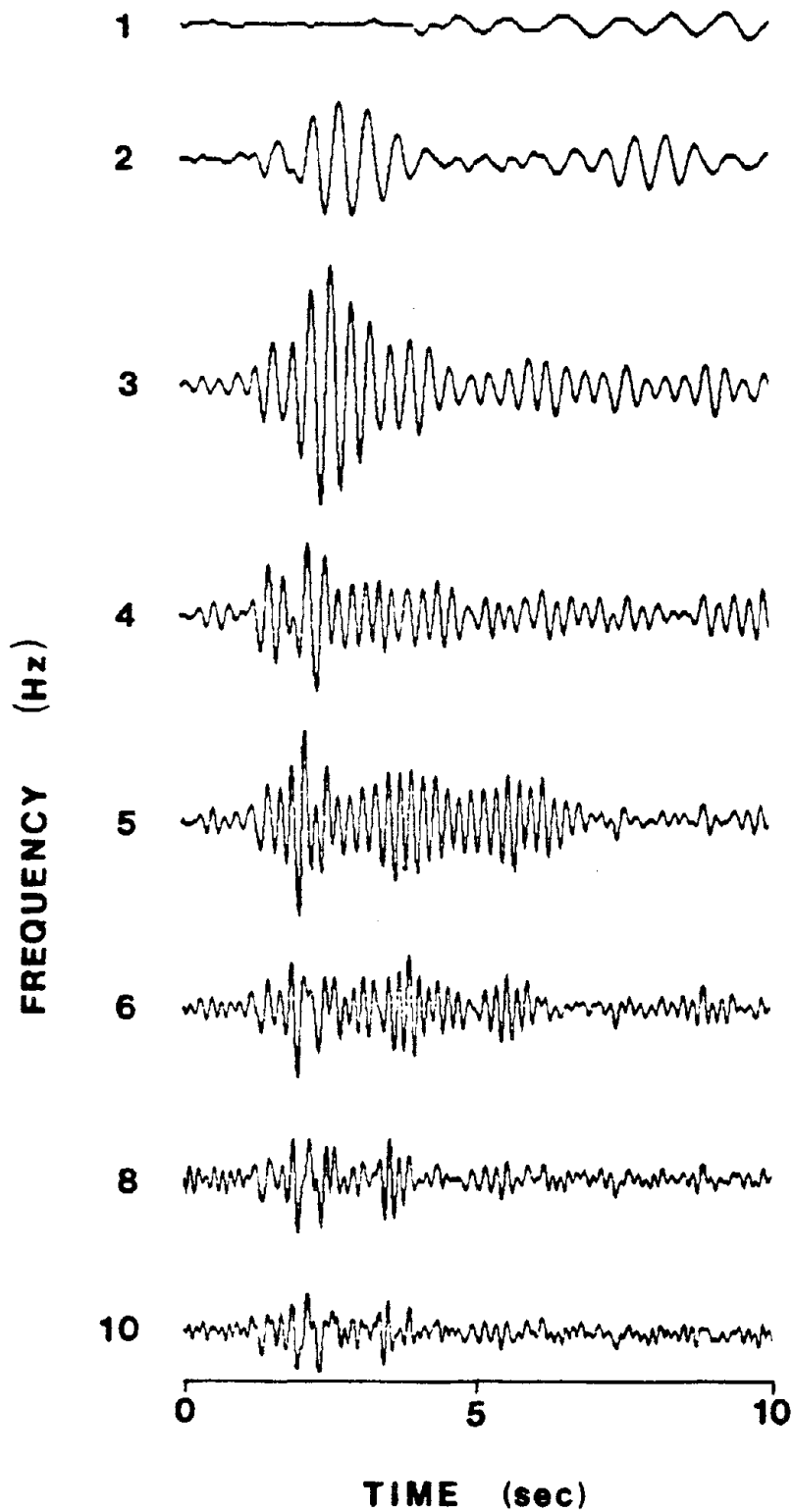
Figure 7.7 Oscillator time histories at 5% damping from the transverse component of acceleration recorded at station C00 during event 5 (peak acceleration = 0.24 g).
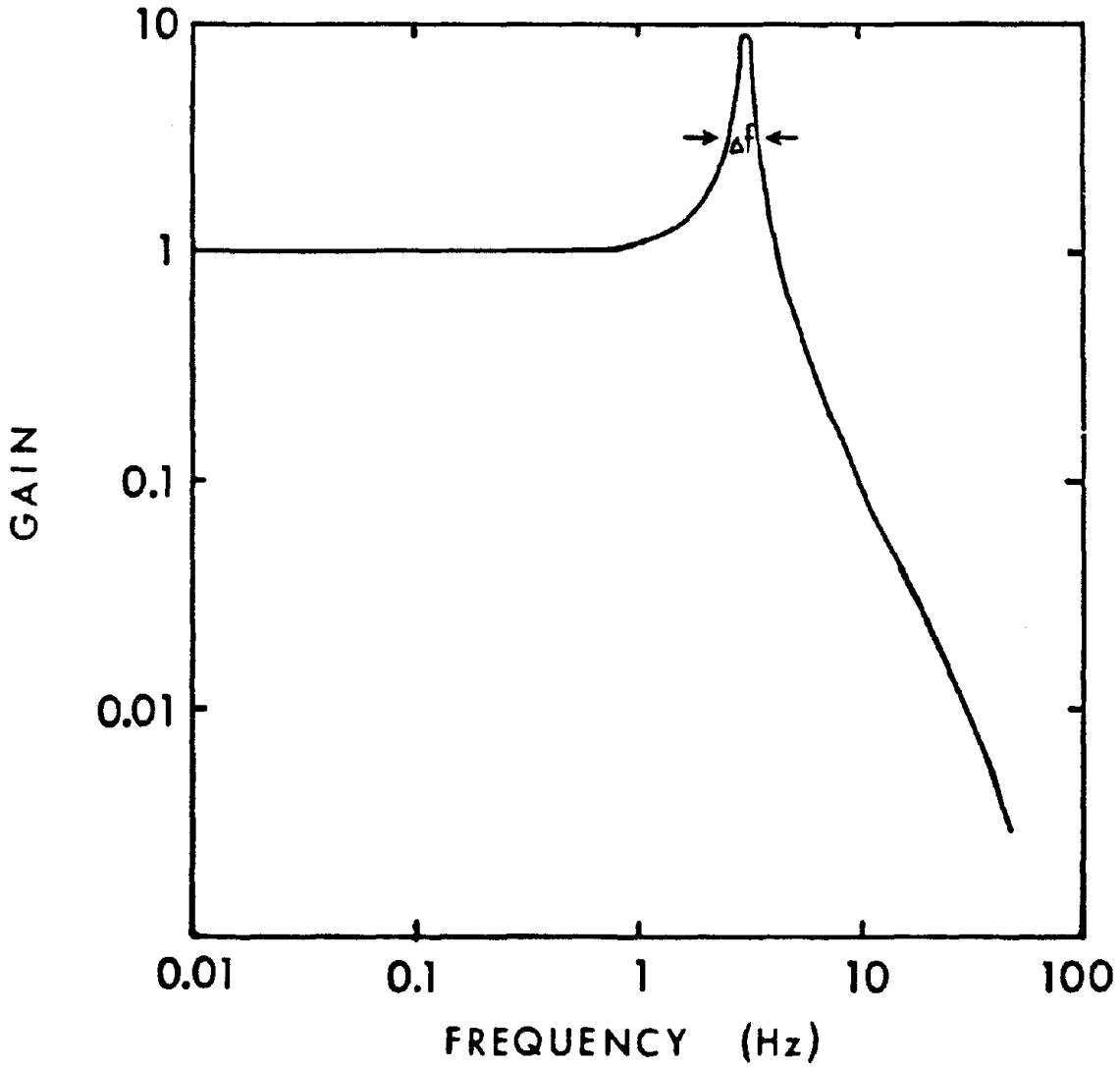
Figure 7.8 The transfer function of a simple oscillator with a natural frequency of 3 Hz and a damping of 5% of critical.
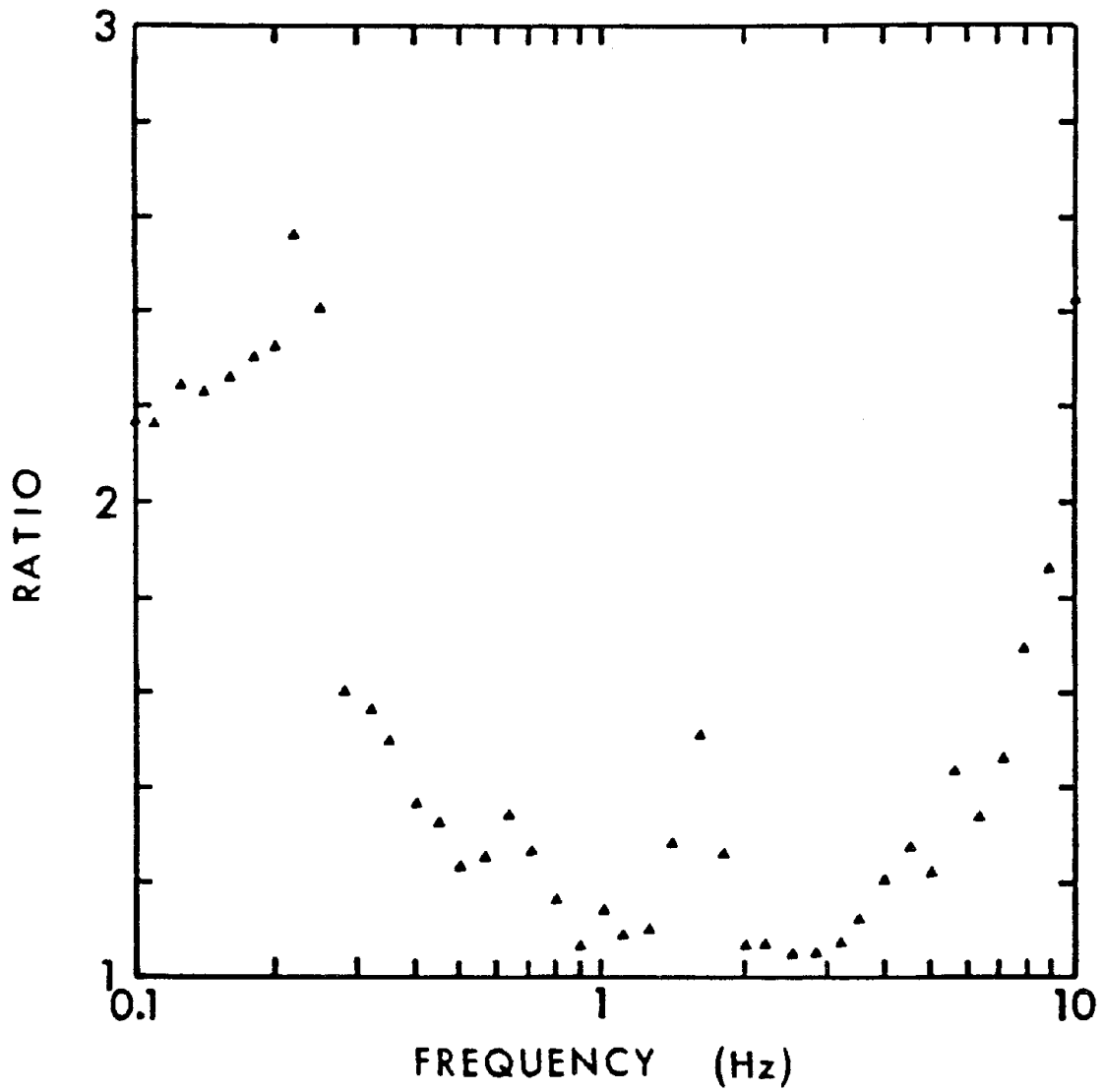
Figure 7.9 Ratio of the response (amplitude) spectrum $SA(\omega)$ to R_{max} for the transverse component recorded at station C00.
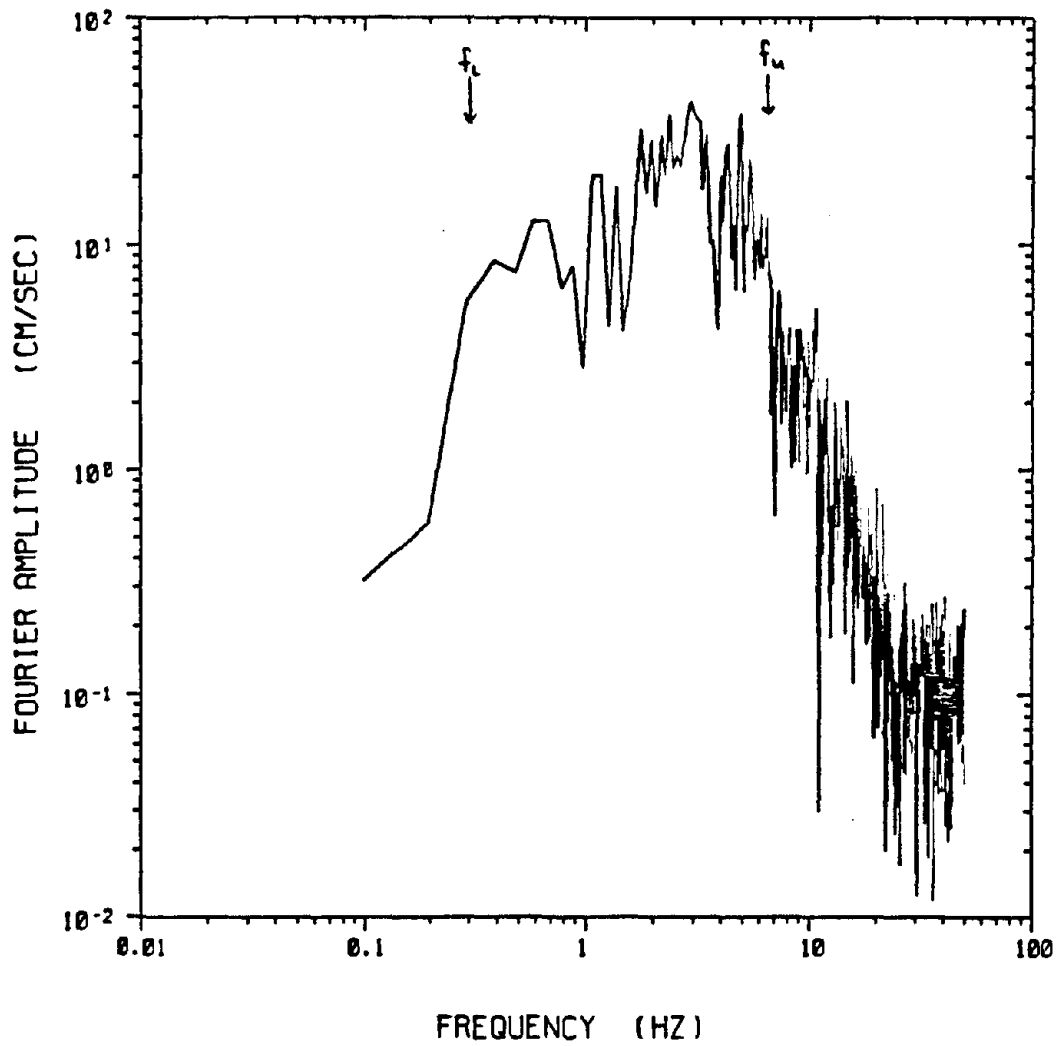
Figure 7.10 Fourier amplitude of the transverse component of acceleration recorded at station C00.
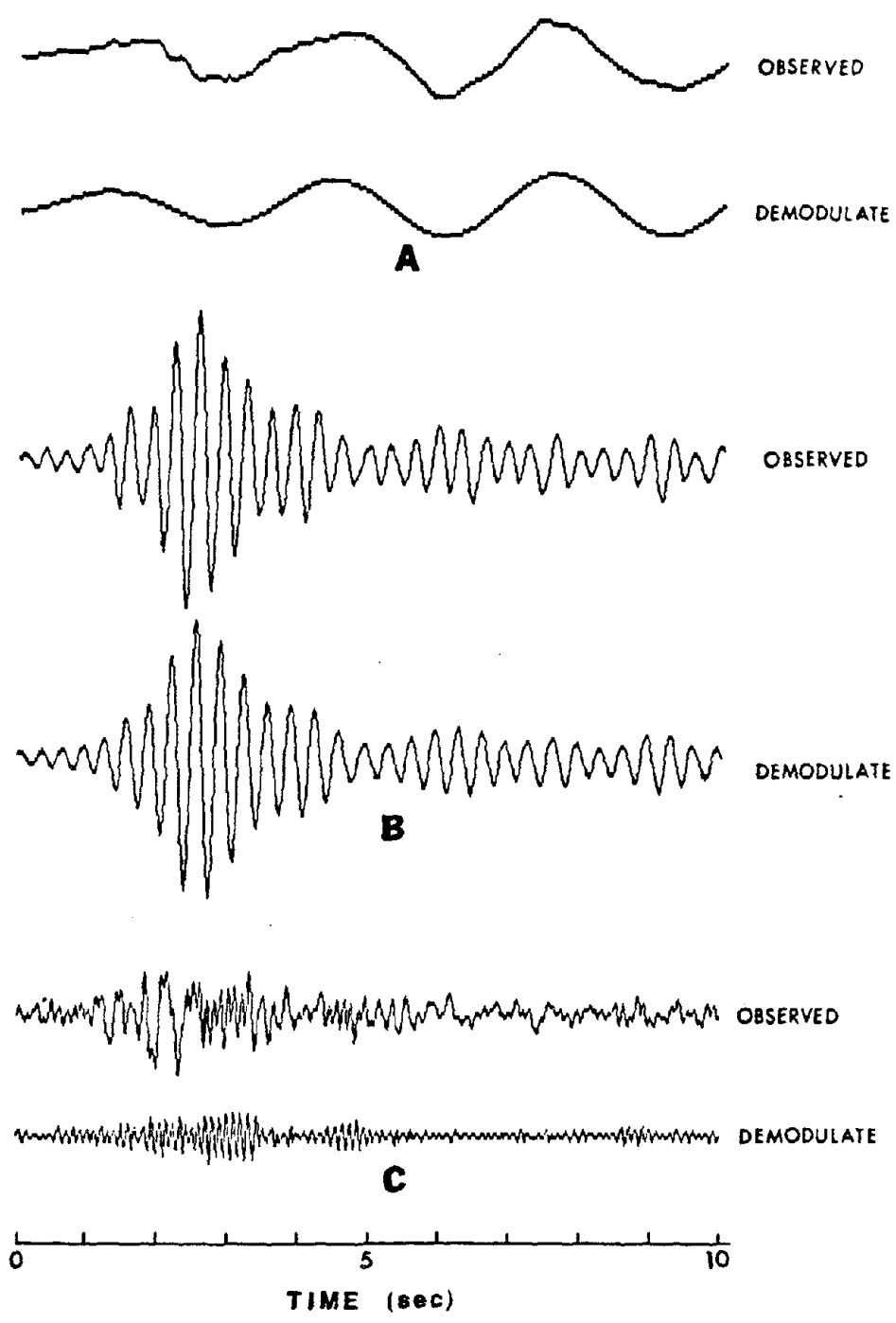
Figure 7.11 Oscillator time histories and demodulates of equation (7.3.2) for three oscillator frequencies.
(a) f=0.3 Hz. (b) f=3.0 Hz. (c) f=10 Hz.

111
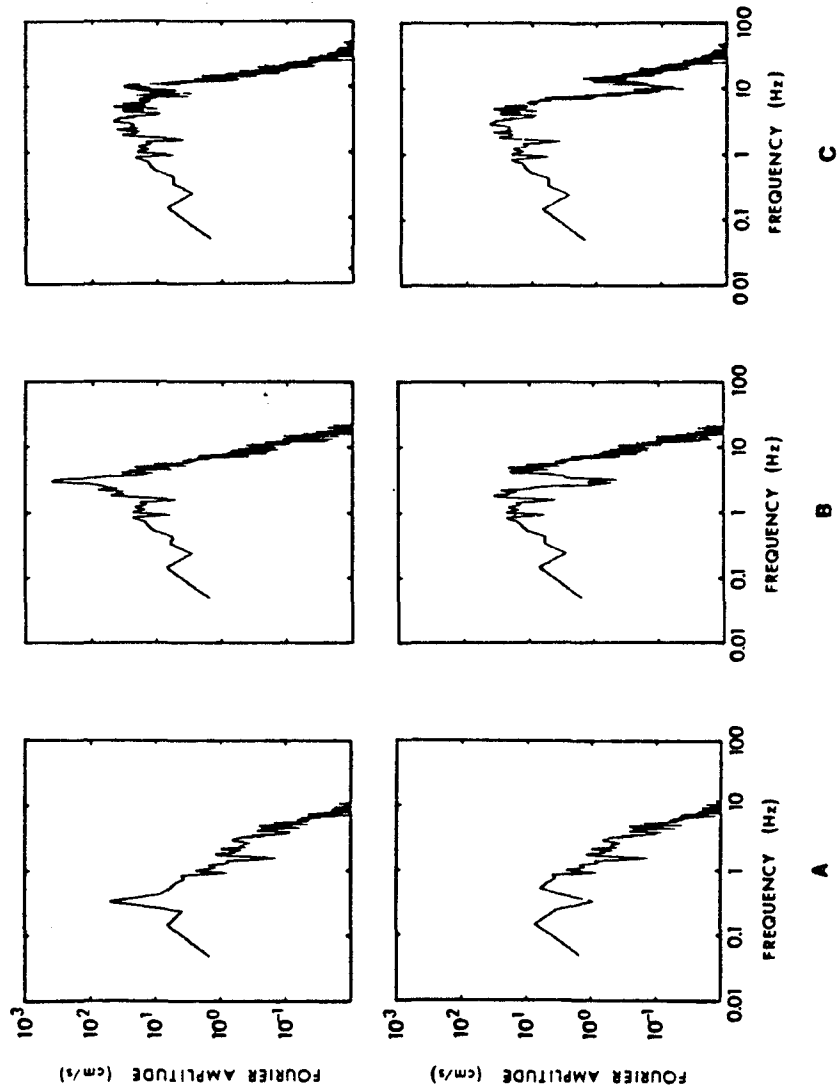
Figure 7.12 Fourier amplitude of the oscillator time history (top) and of the residual (bottom) for the three cases shown in figures 7.11a-c. (a) f=0.3 Hz. (b) f=3.0 Hz. (c) f=10 Hz.

112
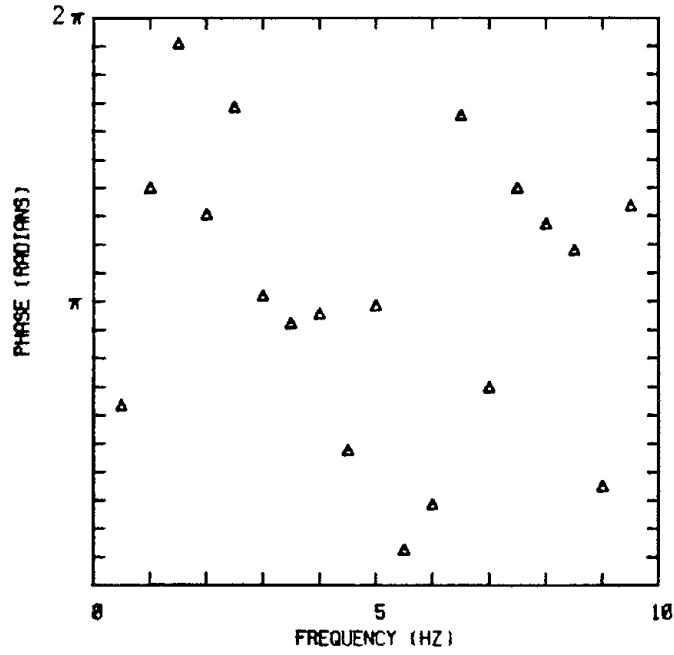
Figure 7.13 (a). The response phase spectra $\Psi_\xi^k(\omega)$ at 5% damping. Station C00, transverse component.
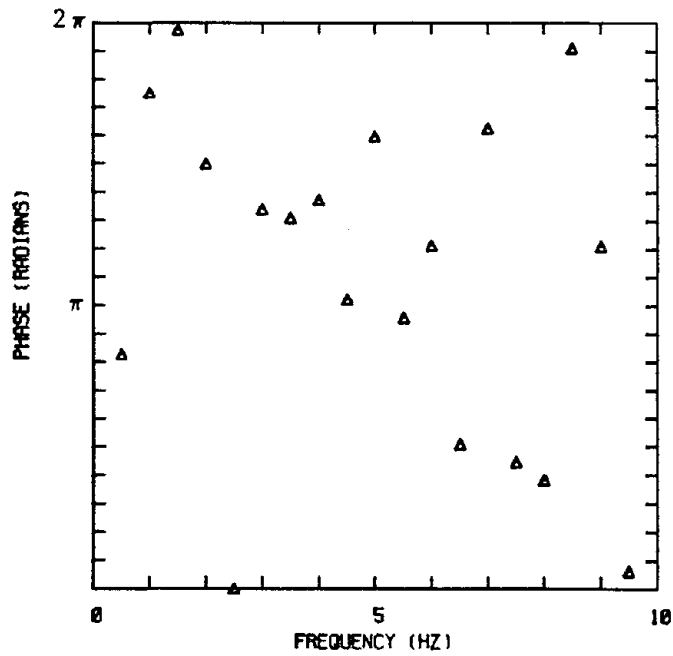
Figure 7.13 (b). The response phase spectra $\Psi_\xi^k(\omega)$ at 5% damping. Station I06, transverse component.

113
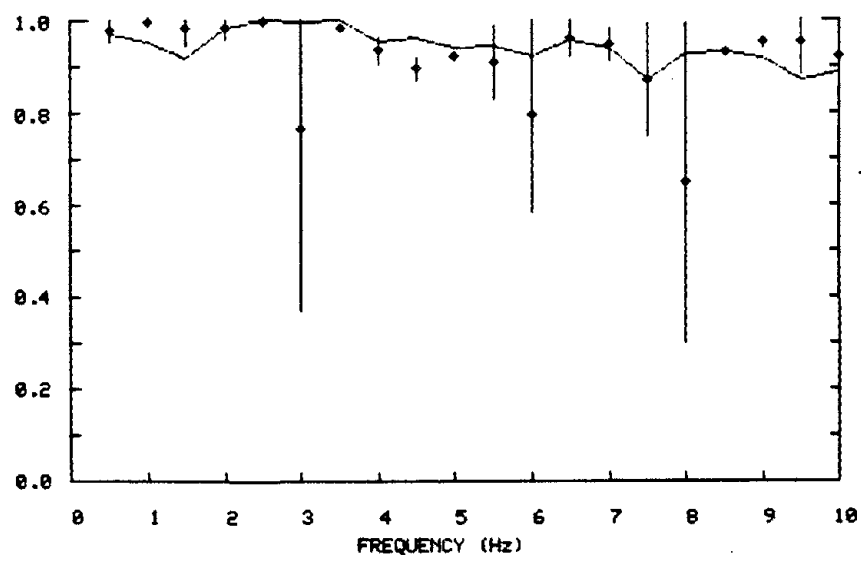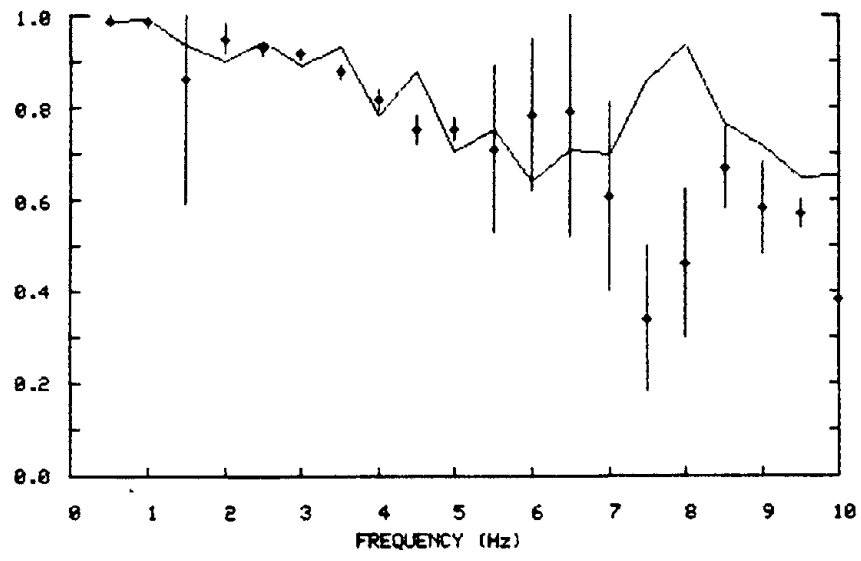
Figure 7.14 Dynamic response ratio estimates for a 200 meter base. The diamonds are the estimates found using equation (7.3.9) and the vertical lines indicate one standard error. The curve is the dynamic response ratio estimated in section 7.2.1 (see figure 7.1).
(a) Station pair C00-I06. (b) Station pair C00-I03.

114

Chapter 8

Conclusions and Recommendations

The work in this report demonstrates the power of array recordings with a common time base over single station recordings. Strong motion arrays are useful to both engineers and seismologists. Engineers require a dense array to measure the variations of ground motions over distances comparable to the dimensions of large structures (50-1000 meters). In contrast, seismologists prefer to have complete azimuthal coverage of the seismic source and therefore may prefer an array with larger dimensions to study extended sources and to increase the chances of recording an earthquake within the array.

The SMART 1 array is a compromise between these two competing objectives. The inner ring has a minimum station spacing of 100 meters and is excellent for engineering use while the outer ring with a radius of 2 km provides some of the extended coverage needed by seismologists. The dense inner ring stations would be useful to seismologists if the rupture was close to the array.

The analysis of the January 29, 1981 rupture process would have benefited from a larger array dimension with greater azimuthal coverage, but the 14° provided by the outer ring stations was sufficient for estimating the rupture velocity. Adding more stations to the interior of the array would not be of much help for frequency-wavenumber analysis, however, an extension of the array to increase the azimuthal coverage would be very useful.

Recommendations

The over 1400 SMART 1 seismic recordings (28 events on three components) in or close to the near-field of the seismic source are an important set of data and require further analysis.

115

Some avenues of future research are outlined below.

The dependence of the coherency and dynamic response ratio on source mechanism, epicentral distance and focal depth can be studied by examining the SMART 1 recordings from the other 27 events recorded as of May, 1984 besides event 5. The coherence estimates from sources at various azimuths can be used to study the seismic wave scattering mechanism.

The rupture model constructed in chapter 6 could be tested through waveform modeling. Waveform modeling requires detailed knowledge of the velocity structure which is not yet available for Taiwan, however, researchers at the Institute of Earth Sciences in Taiwan are developing a three-dimensional velocity model for northeastern Taiwan. When this work is completed, waveform modeling using a stochastic-deterministic model that includes random energy will be possible. The low frequency part of the accelerogram can be generated using deterministic methods such as convolving a source time function with a Green's function. At higher frequencies, the percentage of incoherent or random energy increases and eventually dominates the recorded motion. A suite of ground motions at a single site can be generated, with only one convolution of the source with the Green's function, by resampling the random energy while keeping the coherent energy constant.

As shown in chapter 5, two-dimensional array recordings can be used to separate the different wave types such as P, S and surface wave in strong motion recordings. A full analysis of the percentages of P, S and surface waves at each frequency for sliding time windows is needed. The analysis should also measure the amount of incoherent or random energy that is present in each time window. Such information on wave mixing would be valuable to both seismologists and engineers.

References

Aki, K. and P.G. Richards (1980). *Quantitative Seismology Theory and Methods*, W. H. Freeman and Co., San Francisco.

Archuleta, R. (1982). Analysis of the near-source static and dynamic measurements from the 1979 Imperial Valley Earthquake, *Bull. Seism. Soc. Am.*, 72, 1927-1956.

Båth, M. (1979). *Spectral Analysis in Geophysics*, Elsevier Scientific Publishing Co.

Ben-Menahem, A. (1961). Radiation of seismic surface-waves from finite moving sources, *Bull. Seism. Soc. Am.*, 51, 401-435.

Ben-Menahem, A. and M. Toksöz (1962). Source mechanism from the spectra of long period seismic surface waves, 1. The Mongolian earthquake of December 4, 1957, *J. Geophys. Res.*, 67, 1943-1955.

Benioff, H. (1951). The mechanism of earthquake generation, Paper read at *The meeting of the Seism. Soc. Am.*, Univ. Southern Calif.

Benioff, H. (1955). Mechanism and strain characteristics of the White Wolf fault as indicated by the aftershock sequence, in *Calif. Div. Mines Bulletin* 171, 199-202.

Bingham, C., M.D. Godfrey and J. W. Tukey (1967). Modern techniques of power spectrum estimation, *IEEE Trans.*, AU-15, 56-66.

Bloomfield, P. (1976). *Fourier Analysis of Time Series, An Introduction*, John Willey & Sons Inc., New York.

Bollinger, G.A. (1968). Determination of earthquake fault parameters from long period P waves, *J. Geophys. Res.*, 73, 785-807.

Bollinger, G.A. (1970). Fault length and fracture velocity for the Kyushu, Japan, earthquake of October 3, 1963, *J. Geophys. Res.*, 75, 955-964.

Bolt, B.A. and D.R. Brillinger (1979). Estimation of uncertainties in eigenspectral estimation from decaying geophysical time series, *Geophys. J. R. Astr. Soc.*, 59, 593-603.

Bolt, B.A., C.H. Loh, J. Penzien, Y.B. Tsai, and Y.T. Yeh (1982). Preliminary report on the SMART 1 strong motion array in Taiwan, *EERC Report No. UCB/EERC-82/13*.

Bolt, B.A., N.A. Abrahamson, and Y.T. Yeh (1984). The variation of strong ground motion over short distances, *Eighth World Conf. Earth. Engin.*, San Francisco. 183-189.

Brillinger, D.R. (1981). *Time Series Data Analysis and Theory. Expanded Edition.* Holden-Day, Inc. San Francisco.

Brillinger, D.R., A. Udias and B.A. Bolt (1980). A probability model for regional focal mechanism solutions, *Bull. Seism. Soc. Am.,* **70**, 149-170.

Brune, J.N. (1970). Tectonic stress and the spectra of seismic shear waves from earthquakes, *J. Geophys. Res.,* **75**, 4997-5009.

Brune, J.N. (1971). Correction to "Tectonic stress and the spectra of seismic shear waves from earthquakes", *J. Geophys. Res.,* **76**, 5002.

Capon, J., R.J. Greenfield, and R.J. Kolker (1967). Multidimensional maximum-likelihood processing of a large aperture seismic array, *Proc. IEEE,* **55**, 192-211.

Capon, J. (1969). High resolution frequency-wavenumber spectrum analysis, *Proc. IEEE,* **57**, 1408-1418.

Capon, J. and N.R. Goodman (1970). Probability distribution for estimators of the frequency-wavenumber spectrum, *Proc. IEEE,* **58**, 1785-1786.

Capon, J. (1973). Signal processing and frequency wavenumber spectrum analysis for a large aperature seismic array, in *Methods of Computational Physics,* **13**, 1-59.

Chu, S.T. (1984). *Statistical estimation of the parameters of a moving source from array data,* Ph.D. Thesis, University of California, Berkeley.

Cox, H.(1973). Resolving power and sensitivity to mismatch of optimal array processors, *JASA,* **54**, 771-785.

Ferguson, R., B. Schecter and R. Uhrhammer (1980). *Bulletin of the Seismographic Stations of the University of California,* **50** , No. 1, 82-87.

Filson, J. and T.V. McEvilly (1967). Love wave spectra and the mechanism of the 1966 Parkfield sequence, *Bull. Seism. Soc. Am.,* **57**, 1245-1259.

Gutenburg, B. (1955). Magnitude determination for larger Kern County shocks, 1952; effects of station azimuth and calculation methods, *Calif. Div. Mines Bull.,* **171**, 171-175.

Hartzell, S.H. and D.V. Helmburger (1982). Strong motion modeling of the Imperial Valley Earthquake of 1979, *Bull. Seism. Soc. Am.,* **72**, 571-599.

Hartzell, S.H. and T.H. Heaton (1983). Inversion of strong ground motion and teleseismic waveform data for the fault rupture history of the 1979 Imperial Valley, California earthquake, *Bull, Seism, Soc. Am.,* **73**, 1553-1584.

Housner, G.W., R.R. Martel, and J.C. Alford (1953). Spectrum analysis of strong-motion earthquakes, *Bull. Seism. Soc. Am.,* **43**, 97-119.

Hudson, D.E. (1962). Some problems in the application of spectrum techniques to strong-motion earthquake analysis, *Bull. Seism. Soc. Am.*, **52**, 417-430.

Iwan, W.D. (Editor) (1978). *Strong-Motion Earthquake Instrument Arrays: Proceedings of the International Workshop on Strong-Motion Earthquake Instrument Arrays*, May 2-5, 1978. Honolulu, Hawaii.

Juan, V.C. (1975). Tectonic Evolution of Taiwan, *Tectonophysics*, **26**, 197-212.

Kanamori, H. and P.C. Jennings (1978). Determination of local magnitude M_L, from strong-motion accelerograms, *Bull. Seism. Soc. Am.*, **68**, 471-485.

Kanasewich, E.R. (1981). *Time Sequence Analysis in Geophysics*, University of Alberta Press.

Lacoss R.T. (1975). Review of some techniques for array processing, in *Exploitation of Seismographic Networks*, Noordhoff Int., Netherlands, 11-21.

Lawson, C.L. and R.J. Hanson (1974). *Solving Least Squares Problems*, Prentice Hall, Inc., New Jersey, Chapter 25.

Liaw, A.L. (1977). *Microseisms in geothermal exploration studies in Grass Valley, Nevada.* Ph.D. Thesis. University of California, Berkeley.

Liaw, Z.S. and Y.B. Tsai (1981). Relation between the Richter magnitude and total signal duration of Taiwan earthquakes. *Bull. Inst. Earth Sci. Academia Sinica*, **1**, 23-30.

Lin, M.T. and Y.B. Tsai (1981). Seismotectonics in Taiwan-Luzon area, *Bull. Inst. Earth Sci. Academia Sinica*, **1**, 51-82.

Liu, C.C. (1981). Installation and operation of the SMART 1, *Inst. Earth Sci, Academia Sinica report.*

Liu, H.L. and T. Heaton (1984). Array analysis of the ground velocities and accelerations from the 1971 San Fernando, California, earthquake, *Bull. Seism. Soc. Am.*, **74**, 1951-1968.

Loh, C.H., J. Penzien and Y.B. Tsai (1982). Engineering analysis of SMART 1 array accelerograms, *Earth. Engin. Struc. Dyn.*, **10**, 575-591.

Madariaga, R. (1977). High frequency radiation from crack (stress drop) models of earthquake faulting, *Geophys. J.*, **51**, 625-651.

Madariaga, R. (1983). High frequency radiation from dynamic earthquake fault models, *Ann. Geophys.*, **1**, 17-23.

McLaughlin, K.L. (1983) *Spatial Coherency of Seismic Waveforms* Ph.D. Thesis, University of California, Berkeley.

Nagamune, T. (1971). Source regions of great earthquakes, *Geophys. Mag.*, **35**, 333-339.

Newmark, N.M., W.J. Hall and J.K. Morgan (1978). Building response and free field motion in earthquakes, *Proc. Sixth World Conf. Earth. Engin.*, New Delhi, India, 972-978.

Niazi, M. (1982). Source dynamics of the 1979 Imperial Valley Earthquake from near-source observations of ground acceleration and velocity, *Bull. Seism. Soc. Am.*, 72, 1957-1968.

Olson, A.H., and R. Apsel (1982). Finite faults and inverse theory with applications to the 1979 Imperial Valley Earthquake, *Bull. Seism. Soc. Am.*, 72, 1969-2002.

Richter, C., (1958). *Elementary Seismology*, W. H. Freeman, San Francisco.

Seno, T. (1977). The instantaneous rotation vector of the Philippine Sea Plate relative to the Eurasian Plate, *Tectonophysics*, 42, 209-226.

Seno, T. and K. Kurita (1978). Focal mechanisms and tectonics in the Taiwan-Philippine region, In: S. Uyeda, R. W. Murphy and Kobayashi (Editors) Geodynamics of the Western Pacific. *J. Phys. Earth Suppl. Issue*, 249-263.

Smith, S.W., J.E. Ehrenberg, and E.N. Hernandez (1982). Analysis of the El Centro differential array for the 1979 Imperial Valley Earthquake, *Bull. Seism. Soc. Am.*, 72, 237-258.

Sprengnether Instrument Co. (1980). SA-3000 Instrumentation manual.

Spudich, P. and E. Cranswick (1984). Direct observation of rupture propagation during the 1979 Imperial Valley Earthquake using a short baseline accelerometer array, *Bull. Seism. Soc. Am.*, In press.

Tocher, D. (1958). Earthquake energy and ground breakage, *Bull. Seism. Soc. Am.*, 48, 147-153.

Udias, A. (1971). Source parameters of earthquakes from spectra of Rayleigh waves, *Geophys. J. R. Astron. Soc.*, 22, 353-376.

Wang, J.H., Y.B. Tsai and K.C. Chen (1983). Some aspects of seismicity in Taiwan region, *Bull. Inst. Earth Sci., Academia Sinica*, 3, 87-104.

Wen, K.L. and Y.T. Yeh (1983). Subsurface structure of the large scale strong motion array in Lo Tung, *Institute of Earth Sciences, Academia Sinica*, Report No. ASIES-CR8302. (In Chinese)

Wu, F.T. (1970). Focal mechanisms and tectonics in the vicinity of Taiwan, *Bull. Seism. Soc. Am.*, 60, 2045-2056.

Wu, F.T. (1978). Recent tectonics of Taiwan, In S. Uyeda, R. W. Murphy and K Kobayashi (Editors), *J. Phys. Earth Suppl. Issue*, 39-54.

Wyss, M., and J. Brune (1967). The Alaska earthquake of 28 March 1964: a complex multiple rupture, *Bull. Seism. Soc. Am.*, 57, 1017-1023.

Yeh, Y.T., G.B. Ou and C.C. Lin (1982). Determination of local magnitude scale for Taiwan, *Bull. Inst. Earth Sci. Academia Sinica*, 2, 37-48.

Appendix A

Complex Demodulation

Fourier analysis assumes the time series is stationary but this assumption is not always acceptable. Complex demodulation can be used to study nonstationary time series. Consider a time series of the form

$$x(t) = R(t) \exp\{i(\omega t + \phi(t))\}, \tag{A.1}$$

where $R(t)$ is a slowly changing amplitude and $\phi(t)$ is a slowly changing phase. Complex demodulation is a method for estimating the functions $R(t)$ and $\phi(t)$.

Complex demodulation is a local version of Fourier analysis. It describes the amplitude and phase of an oscillation as in standard Fourier analysis, but it is local because the amplitude and phase are determined only by the data in the neighborhood of t, rather than by the entire time series.

The frequency ω is assumed known and estimation of $R(t)$ and $\phi(t)$ in equation (A.1) involves forming the new series

$$y(t) = x(t) \exp\{-i\omega t\} \tag{A.2}$$

$$= R(t) \exp\{i\phi(t)\}. \tag{A.3}$$

The amplitude and phase estimates are then given simply by

$$R(t) = |y(t)| \tag{A.4}$$

$$\phi(t) = -\tan^{-1}\left[\frac{\mathrm{Im}\{y(t)\}}{\mathrm{Re}\{y(t)\}}\right]. \tag{A.5}$$

$y(t)$ is said to be the **demodulate** of $x(t)$ at frequency ω.

The form of equation (A.1) must be generalized to include negative frequencies. Equation (A.1) becomes

123

$$x(t) = \frac{1}{2} R(t) \left[\exp\{i(\omega t + \phi(t))\} + \exp\{-i(\omega t + \phi(t))\} \right]. \qquad (A.6)$$

The demodulate is

$$y(t) = \frac{1}{2} R(t) \exp\{i\phi(t)\} + \frac{1}{2} R(t) \exp\{-i(2\omega t + \phi(t))\}. \qquad (A.7)$$

The first term on the left hand side is the desired term. The second term is a sinusoid with frequency 2ω and must be removed. This second term can be removed by low-pass filtering the complex demodulate $y(t)$.

The impulse response of the low-pass filter corresponds to the time window used with the standard Fourier transform. The corner frequency of the low-pass filter must be significantly less than 2ω so that the undesired sinusoidal term is removed. As the corner frequency is decreased, the time window length increases so the corner frequency must be chosen to achieve the desired temporal resolution.

In general, complex demodulation can be thought of as narrow-band filtering that is realized by low-pass filtering the series $x(t) \exp\{i\omega t\}$ where $x(t)$ is the observed time series. More detailed descriptions of complex demodulation are given in Bingham *et al.* (1967) and Bloomfield (1976, chapter 6). The first use of complex demodulation in seismology appears to have been by Bolt and Brillinger (1979).

Appendix B

Accelerogram Processing and Array Performance

Each DR-100 records the three components of acceleration digitally on magnetic cassettes in multiplexed format. The digital data are transferred from the cassette to a 9 track tape in ASCII format at the Institute of Earth Sciences. A copy of the 9 track tape is sent to the Seismographic Station at the University of California.

The data are processed at the seismographic station. First, the multiplexing is removed. The digital samples should cycle regularly through the three channels. Occasionally, a sample from a channel is missing. This is called data dropout. To insure the correct timing on all of the components, any missing samples are replaced by linear interpolation. The average frequency of occurrence of data dropout during the first 25 events is approximately 1 per 2000 samples.

Another problem with the digital data is the occurrence of glitches. A glitch or spike is a single sample that is clearly not part of the actual ground acceleration. The glitches are identified by visual inspection of the accelerograms and are replaced by linear interpolation. The average frequency of occurrence of glitches during the first 25 events is approximately 1 per 1000 samples.

The baseline correction procedure used either one of two schemes: an automated scheme or an interactive scheme. The automated scheme simply high-pass filters the data with a four-pole zero phase shift filter with corner frequency at 0.1 Hz. This scheme is adequate for most problems.

The interactive scheme removes slopes in the baseline rather than removing all of the long period information. For example, the velocity trace found by intergrating the accelerogram is shown in figure B1. Here, the only baseline correction is the removal of the initial DC level of the accelerogram. Clearly, there is a hinge at point B where the slope in the velocity baseline changes abruptly. This implies a step in the acceleration baseline at point B. By removing such steps in the acceleration baseline, all of the long period information is not lost. This baseline correction method is time consuming because it is interactive. The interactive scheme is used for the event 5 accelerograms in this thesis but for most problems, the automated scheme is sufficient.

Of the 1419 recorded produced by the SMART 1 array during its first four years of operation, only 24 components failed to operate correctly. This is a success rate of over 98%.
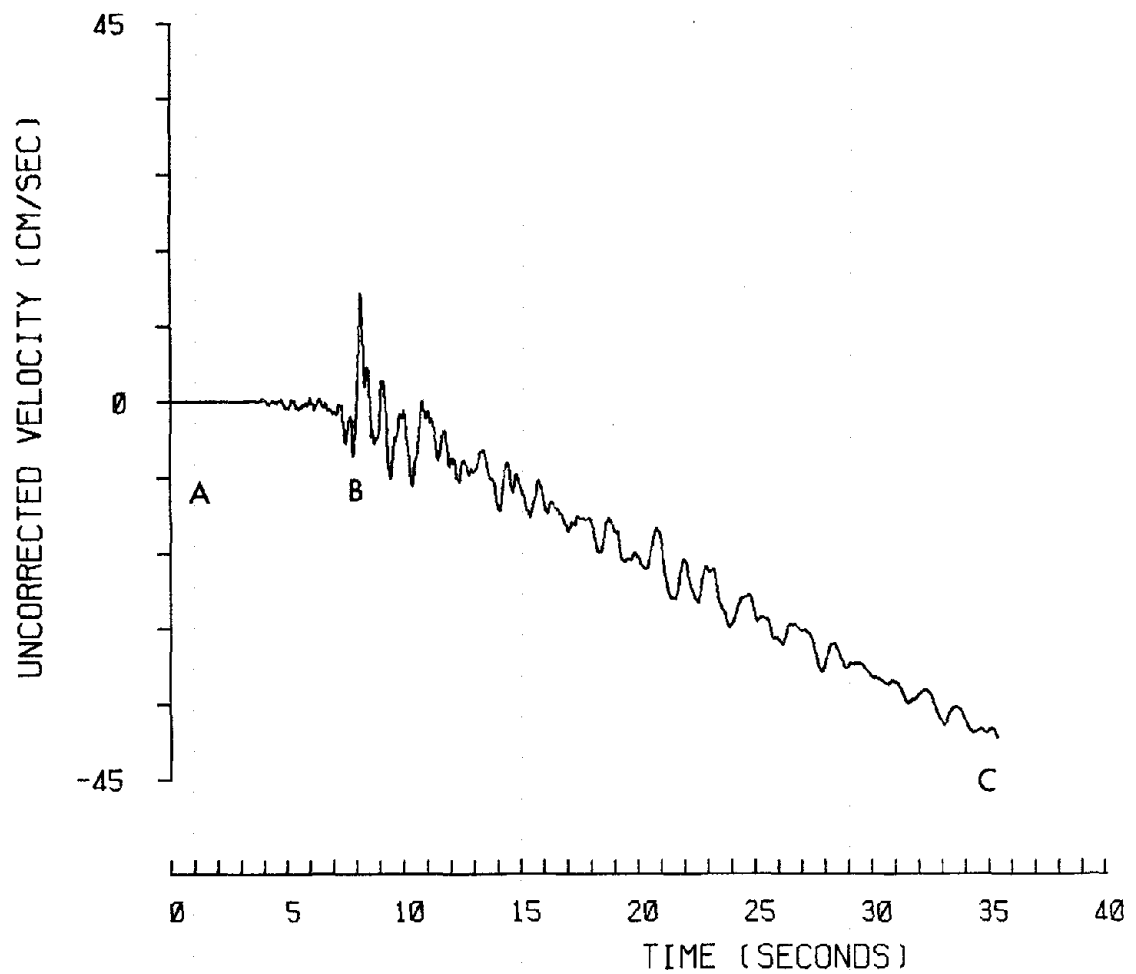
Figure B1. Velocity trace from C00 NS during event 5. The DC level at the start of the accelerogram was removed before integrating. At point B, there is a hinge in the velocity baseline. The slope between B-C indicates a step in the acceleration baseline at point B.

127

NOTE: Numbers in parentheses are Accession Numbers assigned by the National Technical Information Service; these are followed by a price code. Copies of the reports may be ordered from the National Technical Information Service, 5285 Port Royal Road, Springfield, Virginia, 22161. Accession Numbers should be quoted on orders for reports (PB --- ---) and remittance must accompany each order. Reports without this information were not available at time of printing. The complete list of EERC reports (from EERC 67-1) is available upon request from the Earthquake Engineering Research Center, University of California, Berkeley, 47th Street and Hoffman Boulevard, Richmond, California 94804.

UCB/EERC-79/01 "Hysteretic Behavior of Lightweight Reinforced Concrete Beam-Column Subassemblages," by B. Forzani, E.P. Popov and V.V. Bertero - April 1979(PB 298 267)A06

UCB/EERC-79/02 "The Development of a Mathematical Model to Predict the Flexural Response of Reinforced Concrete Beams to Cyclic Loads, Using System Identification," by J. Stanton & H. McNiven - Jan. 1979(PB 295 875)A10

UCB/EERC-79/03 "Linear and Nonlinear Earthquake Response of Simple Torsionally Coupled Systems," by C.L. Kan and A.K. Chopra - Feb. 1979(PB 298 262)A06

UCB/EERC-79/04 "A Mathematical Model of Masonry for Predicting its Linear Seismic Response Characteristics," by Y. Mengi and H.D. McNiven - Feb. 1979(PB 298 266)A06

UCB/EERC-79/05 "Mechanical Behavior of Lightweight Concrete Confined by Different Types of Lateral Reinforcement," by M.A. Manrique, V.V. Bertero and E.P. Popov - May 1979(PB 301 114)A06

UCB/EERC-79/06 "Static Tilt Tests of a Tall Cylindrical Liquid Storage Tank," by R.W. Clough and A. Niwa - Feb. 1979 (PB 301 167)A06

UCB/EERC-79/07 "The Design of Steel Energy Absorbing Restrainers and Their Incorporation into Nuclear Power Plants for Enhanced Safety: Volume 1 - Summary Report," by P.N. Spencer, V.F. Zackay, and E.R. Parker - Feb. 1979(UCB/EERC-79/07)A09

UCB/EERC-79/08 "The Design of Steel Energy Absorbing Restrainers and Their Incorporation into Nuclear Power Plants for Enhanced Safety: Volume 2 - The Development of Analyses for Reactor System Piping,""Simple Systems" by M.C. Lee, J. Penzien, A.K. Chopra and K, Suzuki "Complex Systems" by G.H. Powell, E.L. Wilson, R.W. Clough and D.G. Row - Feb. 1979(UCB/EERC-79/08)A10

UCB/EERC-79/09 "The Design of Steel Energy Absorbing Restrainers and Their Incorporation into Nuclear Power Plants for Enhanced Safety: Volume 3 - Evaluation of Commercial Steels," by W.S. Owen, R.M.N. Pelloux, R.O. Ritchie, M. Faral, T. Ohhashi, J. Toplosky, S.J. Hartman, V.F. Zackay and E.R. Parker - Feb. 1979(UCB/EERC-79/09)A04

UCB/EERC-79/10 "The Design of Steel Energy Absorbing Restrainers and Their Incorporation into Nuclear Power Plants for Enhanced Safety: Volume 4 - A Review of Energy-Absorbing Devices," by J.M. Kelly and M.S. Skinner - Feb. 1979(UCB/EERC-79/10)A04

UCB/EERC-79/11 "Conservatism In Summation Rules for Closely Spaced Modes," by J.M. Kelly and J.L. Sackman - May 1979(PB 301 328)A03

UCB/EERC-79/12 "Cyclic Loading Tests of Masonry Single Piers; Volume 3 - Height to Width Ratio of 0.5," by P.A. Hidalgo, R.L. Mayes, H.D. McNiven and R.W. Clough - May 1979(PB 301 321)A08

UCB/EERC-79/13 "Cyclic Behavior of Dense Course-Grained Materials in Relation to the Seismic Stability of Dams," by N.G. Banerjee, H.B. Seed and C.K. Chan - June 1979(PB 301 373)A13

UCB/EERC-79/14 "Seismic Behavior of Reinforced Concrete Interior Beam-Column Subassemblages," by S. Viwathanatepa, E.P. Popov and V.V. Bertero - June 1979(PB 301 326)A10

UCB/EERC-79/15 "Optimal Design of Localized Nonlinear Systems with Dual Performance Criteria Under Earthquake Excitations," by M.A. Bhatti - July 1979(PB 80 167 109)A06

UCB/EERC-79/16 "OPTDYN - A General Purpose Optimization Program for Problems with or without Dynamic Constraints," by M.A. Bhatti, E. Polak and K.S. Pister - July 1979(PB 80 167 091)A05

UCB/EERC-79/17 "ANSR-II, Analysis of Nonlinear Structural Response, Users Manual," by D.P. Mondkar and G.H. Powell July 1979(PB 80 113 301)A05

UCB/EERC-79/18 "Soil Structure Interaction in Different Seismic Environments," A. Gomez-Masso, J. Lysmer, J.-C. Chen and H.B. Seed - August 1979(PB 80 101 520)A04

UCB/EERC-79/19 "ARMA Models for Earthquake Ground Motions," by M.K. Chang, J.W. Kwiatkowski, R.F. Nau, R.M. Oliver and K.S. Pister - July 1979(PB 301 166)A05

UCB/EERC-79/20 "Hysteretic Behavior of Reinforced Concrete Structural Walls," by J.M. Vallenas, V.V. Bertero and E.P. Popov - August 1979(PB 80 165 905)A12

UCB/EERC-79/21 "Studies on High-Frequency Vibrations of Buildings - 1: The Column Effect," by J. Lubliner - August 1979 (PB 80 158 553)A03

UCB/EERC-79/22 "Effects of Generalized Loadings on Bond Reinforcing Bars Embedded in Confined Concrete Blocks," by S. Viwathanatepa, E.P. Popov and V.V. Bertero - August 1979(PB 81 124 018)A14

UCB/EERC-79/23 "Shaking Table Study of Single-Story Masonry Houses, Volume 1: Test Structures 1 and 2," by P. Gülkan, R.L. Mayes and R.W. Clough - Sept. 1979 (HUD-000 1763)A12

UCB/EERC-79/24 "Shaking Table Study of Single-Story Masonry Houses, Volume 2: Test Structures 3 and 4," by P. Gülkan, R.L. Mayes and R.W. Clough - Sept. 1979 (HUD-000 1836)A12

UCB/EERC-79/25 "Shaking Table Study of Single-Story Masonry Houses, Volume 3: Summary, Conclusions and Recommendations," by R.W. Clough, R.L. Mayes and P. Gülkan - Sept. 1979 (HUD-000 1837)A06

UCB/EERC-79/26   "Recommendations for a U.S.-Japan Cooperative Research Program Utilizing Large-Scale Testing Facilities,"
                  by U.S.-Japan Planning Group - Sept. 1979(PB 301 407)A06

UCB/EERC-79/27   "Earthquake-Induced Liquefaction Near Lake Amatitlan, Guatemala," by H.B. Seed, I. Arango, C.K. Chan,
                  A. Gomez-Masso and R. Grant de Ascoli - Sept. 1979(NUREG-CR1341)A03

UCB/EERC-79/28   "Infill Panels: Their Influence on Seismic Response of Buildings," by J.W. Axley and V.V. Bertero
                  Sept. 1979(PB 80 163 371)A10

UCB/EERC-79/29   "3D Truss Bar Element (Type 1) for the ANSR-II Program," by D.P. Mondkar and G.H. Powell - Nov. 1979
                  (PB 80 169 709)A02

UCB/EERC-79/30   "2D Beam-Column Element (Type 5 - Parallel Element Theory) for the ANSR-II Program," by D.G. Row,
                  G.H. Powell and D.P. Mondkar - Dec. 1979(PB 80 167 224)A03

UCB/EERC-79/31   "3D Beam-Column Element (Type 2 - Parallel Element Theory) for the ANSR-II Program," by A. Riahi,
                  G.H. Powell and D.P. Mondkar - Dec. 1979(PB 80 167 216)A03

UCB/EERC-79/32   "On Response of Structures to Stationary Excitation," by A. Der Kiureghian - Dec. 1979(PB 80166 929)A03

UCB/EERC-79/33   "Undisturbed Sampling and Cyclic Load Testing of Sands," by S. Singh, H.B. Seed and C.K. Chan
                  Dec. 1979(ADA 087 298)A07

UCB/EERC-79/34   "Interaction Effects of Simultaneous Torsional and Compressional Cyclic Loading of Sand," by
                  P.M. Griffin and W.N. Houston - Dec. 1979(ADA 092 352)A15

UCB/EERC-80/01   "Earthquake Response of Concrete Gravity Dams Including Hydrodynamic and Foundation Interaction
                  Effects," by A.K. Chopra, P. Chakrabarti and S. Gupta - Jan. 1980(AD-A087297)A10

UCB/EERC-80/02   "Rocking Response of Rigid Blocks to Earthquakes," by C.S. Yim, A.K. Chopra and J. Penzien - Jan. 1980
                  (PB80 166 002)A04

UCB/EERC-80/03   "Optimum Inelastic Design of Seismic-Resistant Reinforced Concrete Frame Structures," by S.W. Zagajeski
                  and V.V. Bertero - Jan. 1980(PB80 164 635)A06

UCB/EERC-80/04   "Effects of Amount and Arrangement of Wall-Panel Reinforcement on Hysteretic Behavior of Reinforced
                  Concrete Walls," by R. Iliya and V.V. Bertero - Feb. 1980(PB81 122 525)A09

UCB/EERC-80/05   "Shaking Table Research on Concrete Dam Models," by A. Niwa and R.W. Clough - Sept. 1980(PB81 122 368)A06

UCB/EERC-80/06   "The Design of Steel Energy-Absorbing Restrainers and their Incorporation into Nuclear Power Plants for
                  Enhanced Safety (Vol 1A): Piping with Energy Absorbing Restrainers: Parameter Study on Small Systems,"
                  by G.H. Powell, C. Oughourlian and J. Simons - June 1980

UCB/EERC-80/07   "Inelastic Torsional Response of Structures Subjected to Earthquake Ground Motions," by Y. Yamazaki
                  April 1980(PB81 122 327)A08

UCB/EERC-80/08   "Study of X-Braced Steel Frame Structures Under Earthquake Simulation," by Y. Ghanaat - April 1980
                  (PB81 122 335)A11

UCB/EERC-80/09   "Hybrid Modelling of Soil-Structure Interaction," by S. Gupta, T.W. Lin, J. Penzien and C.S. Yeh
                  May 1980(PB81 122 319)A07

UCB/EERC-80/10   "General Applicability of a Nonlinear Model of a One Story Steel Frame," by B.I. Sveinsson and
                  H.D. McNiven - May 1980(PB81 124 877)A06

UCB/EERC-80/11   "A Green-Function Method for Wave Interaction with a Submerged Body," by W. Kioka - April 1980
                  (PB81 122 269)A07

UCB/EERC-80/12   "Hydrodynamic Pressure and Added Mass for Axisymmetric Bodies," by F. Nilrat - May 1980(PB81 122 343)A08

UCB/EERC-80/13   "Treatment of Non-Linear Drag Forces Acting on Offshore Platforms," by B.V. Dao and J. Penzien
                  May 1980(PB81 153 413)A07

UCB/EERC-80/14   "2D Plane/Axisymmetric Solid Element (Type 3 - Elastic or Elastic-Perfectly Plastic) for the ANSR-II
                  Program," by D.P. Mondkar and G.H. Powell - July 1980(PB81 122 350)A03

UCB/EERC-80/15   "A Response Spectrum Method for Random Vibrations," by A. Der Kiureghian - June 1980(PB81 122 301)A03

UCB/EERC-80/16   "Cyclic Inelastic Buckling of Tubular Steel Braces," by V.A. Zayas, E.P. Popov and S.A. Mahin
                  June 1980(PB81 124 885)A10

UCB/EERC-80/17   "Dynamic Response of Simple Arch Dams Including Hydrodynamic Interaction," by C.S. Porter and
                  A.K. Chopra - July 1980(PB81 124 000)A13

UCB/EERC-80/18   "Experimental Testing of a Friction Damped Aseismic Base Isolation System with Fail-Safe
                  Characteristics," by J.M. Kelly, K.E. Beucke and M.S. Skinner - July 1980(PB81 148 595)A04

UCB/EERC-80/19   "The Design of Steel Energy-Absorbing Restrainers and their Incorporation into Nuclear Power Plants for
                  Enhanced Safety (Vol 1B): Stochastic Seismic Analyses of Nuclear Power Plant Structures and Piping
                  Systems Subjected to Multiple Support Excitations," by M.C. Lee and J. Penzien - June 1980

UCB/EERC-80/20   "The Design of Steel Energy-Absorbing Restrainers and their Incorporation into Nuclear Power Plants
                  for Enhanced Safety (Vol 1C): Numerical Method for Dynamic Substructure Analysis," by J.M. Dickens
                  and E.L. Wilson - June 1980

UCB/EERC-80/21   "The Design of Steel Energy-Absorbing Restrainers and their Incorporation into Nuclear Power Plants
                  for Enhanced Safety (Vol 2): Development and Testing of Restraints for Nuclear Piping Systems," by
                  J.M. Kelly and M.S. Skinner - June 1980

UCB/EERC-80/22   "3D Solid Element (Type 4-Elastic or Elastic-Perfectly-Plastic) for the ANSR-II Program," by
                  D.P. Mondkar and G.H. Powell - July 1980(PB81 123 242)A03

UCB/EERC-80/23   "Gap-Friction Element (Type 5) for the ANSR-II Program," by D.P. Mondkar and G.H. Powell - July 1980
                  (PB81 122 285)A03

130

UCB/EERC-80/24   "U-Bar Restraint Element (Type 11) for the ANSR-II Program," by C. Oughourlian and G.H. Powell
                  July 1980(PB81 122 293)A03

UCB/EERC-80/25   "Testing of a Natural Rubber Base Isolation System by an Explosively Simulated Earthquake," by
                  J.M. Kelly - August 1980(PB81 201 360)A04

UCB/EERC-80/26   "Input Identification from Structural Vibrational Response," by Y. Hu - August 1980(PB81 152 308)A05

UCB/EERC-80/27   "Cyclic Inelastic Behavior of Steel Offshore Structures," by V.A. Zayas, S.A. Mahin and E.P. Popov
                  August 1980(PB81 196 180)A15

UCB/EERC-80/28   "Shaking Table Testing of a Reinforced Concrete Frame with Biaxial Response," by M.G. Oliva
                  October 1980(PB81 154 304)A10

UCB/EERC-80/29   "Dynamic Properties of a Twelve-Story Prefabricated Panel Building," by J.G. Bouwkamp, J.P. Kollegger
                  and R.M. Stephen - October 1980(PB82 117 128)A06

UCB/EERC-80/30   "Dynamic Properties of an Eight-Story Prefabricated Panel Building," by J.G. Bouwkamp, J.P. Kollegger
                  and R.M. Stephen - October 1980(PB81 200 313)A05

UCB/EERC-80/31   "Predictive Dynamic Response of Panel Type Structures Under Earthquakes," by J.P. Kollegger and
                  J.G. Bouwkamp - October 1980(PB81 152 316)A04

UCB/EERC-80/32   "The Design of Steel Energy-Absorbing Restrainers and their Incorporation into Nuclear Power Plants
                  for Enhanced Safety (Vol 3): Testing of Commercial Steels in Low-Cycle Torsional Fatigue," by
                  P. Spencer, E.R. Parker, E. Jongewaard and M. Drory

UCB/EERC-80/33   "The Design of Steel Energy-Absorbing Restrainers and their Incorporation into Nuclear Power Plants
                  for Enhanced Safety (Vol 4): Shaking Table Tests of Piping Systems with Energy-Absorbing Restrainers,"
                  by S.F. Stiemer and W.G. Godden - Sept. 1980

UCB/EERC-80/34   "The Design of Steel Energy-Absorbing Restrainers and their Incorporation into Nuclear Power Plants
                  for Enhanced Safety (Vol 5): Summary Report," by P. Spencer

UCB/EERC-80/35   "Experimental Testing of an Energy-Absorbing Base Isolation System," by J.M. Kelly, M.S. Skinner and
                  K.E. Beucke - October 1980(PB81 154 072)A04

UCB/EERC-80/36   "Simulating and Analyzing Artificial Non-Stationary Earthquake Ground Motions," by R.F. Nau, R.M. Oliver
                  and K.S. Pister - October 1980(PB81 153 397)A04

UCB/EERC-80/37   "Earthquake Engineering at Berkeley - 1980," - Sept. 1980(PB81 205 874)A09

UCB/EERC-80/38   "Inelastic Seismic Analysis of Large Panel Buildings," by V. Schricker and G.H. Powell - Sept. 1980
                  (PB81 154 338)A13

UCB/EERC-80/39   "Dynamic Response of Embankment, Concrete-Gravity and Arch Dams Including Hydrodynamic Interaction,"
                  by J.F. Hall and A.K. Chopra - October 1980(PB81 152 324)A11

UCB/EERC-80/40   "Inelastic Buckling of Steel Struts Under Cyclic Load Reversal," by R.G. Black, W.A. Wenger and
                  E.P. Popov - October 1980(PB81 154 312)A08

UCB/EERC-80/41   "Influence of Site Characteristics on Building Damage During the October 3, 1974 Lima Earthquake," by
                  P. Repetto, I. Arango and H.B. Seed - Sept. 1980(PB81 161 739)A05

UCB/EERC-80/42   "Evaluation of a Shaking Table Test Program on Response Behavior of a Two Story Reinforced Concrete
                  Frame," by J.M. Blondet, R.W. Clough and S.A. Mahin

UCB/EERC-80/43   "Modelling of Soil-Structure Interaction by Finite and Infinite Elements," by F. Medina -
                  December 1980(PB81 229 270)A04

UCB/EERC-81/01   "Control of Seismic Response of Piping Systems and Other Structures by Base Isolation," edited by J.M.
                  Kelly - January 1981 (PB81 200 735)A05

UCB/EERC-81/02   "OPTNSR - An Interactive Software System for Optimal Design of Statically and Dynamically Loaded
                  Structures with Nonlinear Response," by M.A. Bhatti, V. Ciampi and K.S. Pister - January 1981
                  (PB81 218 851)A09

UCB/EERC-81/03   "Analysis of Local Variations in Free Field Seismic Ground Motions," by J.-C. Chen, J. Lysmer and H.B.
                  Seed - January 1981 (AD-A099508)A13

UCB/EERC-81/04   "Inelastic Structural Modeling of Braced Offshore Platforms for Seismic Loading," by V.A. Zayas,
                  P.-S.B. Shing, S.A. Mahin and E.P. Popov - January 1981(PB82 138 777)A07

UCB/EERC-81/05   "Dynamic Response of Light Equipment in Structures," by A. Der Kiureghian, J.L. Sackman and B. Nour-
                  Omid - April 1981 (PB81 218 497)A04

UCB/EERC-81/06   "Preliminary Experimental Investigation of a Broad Base Liquid Storage Tank," by J.G. Bouwkamp, J.P.
                  Kollegger and R.M. Stephen - May 1981(PB82 140 385)A03

UCB/EERC-81/07   "The Seismic Resistant Design of Reinforced Concrete Coupled Structural Walls," by A.E. Aktan and V.V.
                  Bertero - June 1981(PB82 113 358)A11

UCB/EERC-81/08   "The Undrained Shearing Resistance of Cohesive Soils at Large Deformations," by M.R. Pyles and H.B.
                  Seed - August 1981

UCB/EERC-81/09   "Experimental Behavior of a Spatial Piping System with Steel Energy Absorbers Subjected to a Simulated
                  Differential Seismic Input," by S.F. Stiemer, W.G. Godden and J.M. Kelly - July 1981

131

UCB/EERC-81/10   "Evaluation of Seismic Design Provisions for Masonry in the United States," by B.I. Sveinsson, R.L. Mayes and H.D. McNiven - August 1981 (PB82 166 075)A08

UCB/EERC-81/11   "Two-Dimensional Hybrid Modelling of Soil-Structure Interaction," by T.-J. Tzong, S. Gupta and J. Penzien - August 1981(PB82 142 118)A04

UCB/EERC-81/12   "Studies on Effects of Infills in Seismic Resistant R/C Construction," by S. Brokken and V.V. Bertero - September 1981 (PB82 166 190)A09

UCB/EERC-81/13   "Linear Models to Predict the Nonlinear Seismic Behavior of a One-Story Steel Frame," by H. Valdimarsson, A.H. Shah and H.D. McNiven - September 1981(PB82 138 793)A07

UCB/EERC-81/14   "TLUSH: A Computer Program for the Three-Dimensional Dynamic Analysis of Earth Dams," by T. Kagawa, L.H. Mejia, H.B. Seed and J. Lysmer - September 1981(PB82 139 940)A06

UCB/EERC-81/15   "Three Dimensional Dynamic Response Analysis of Earth Dams," by L.H. Mejia and H.B. Seed - September 1981 (PB82 137 274)A12

UCB/EERC-81/16   "Experimental Study of Lead and Elastomeric Dampers for Base Isolation Systems," by J.M. Kelly and S.B. Hodder - October 1981 (PB82 166 182)A05

UCB/EERC-81/17   "The Influence of Base Isolation on the Seismic Response of Light Secondary Equipment," by J.M. Kelly - April 1981 (PB82 255 266)A04

UCB/EERC-81/18   "Studies on Evaluation of Shaking Table Response Analysis Procedures," by J. Marcial Blondet - November 1981 (PB82 197 278)A10

UCB/EERC-81/19   "DELIGHT.STRUCT: A Computer-Aided Design Environment for Structural Engineering," by R.J. Balling, K.S. Pister and E. Polak - December 1981 (PB82 218 496)A07

UCB/EERC-81/20   "Optimal Design of Seismic-Resistant Planar Steel Frames," by R.J. Balling, V. Ciampi, K.S. Pister and E. Polak - December 1981 (PB82 220 179)A07

UCB/EERC-82/01   "Dynamic Behavior of Ground for Seismic Analysis of Lifeline Systems," by T. Sato and A. Der Kiureghian - January 1982 (PB82 218 926)A05

UCB/EERC-82/02   "Shaking Table Tests of a Tubular Steel Frame Model," by Y. Ghanaat and R. W. Clough - January 1982 (PB82 220 161)A07

UCB/EERC-82/03   "Behavior of a Piping System under Seismic Excitation: Experimental Investigations of a Spatial Piping System supported by Mechanical Shock Arrestors and Steel Energy Absorbing Devices under Seismic Excitation," by S. Schneider, H.-M. Lee and W. G. Godden - May 1982 (PB83 172 544)A09

UCB/EERC-82/04   "New Approaches for the Dynamic Analysis of Large Structural Systems," by E. L. Wilson - June 1982 (PB83 148 080)A05

UCB/EERC-82/05   "Model Study of Effects of Damage on the Vibration Properties of Steel Offshore Platforms," by F. Shahrivar and J. G. Bouwkamp - June 1982 (PB83 148 742)A10

UCB/EERC-82/06   "States of the Art and Practice in the Optimum Seismic Design and Analytical Response Prediction of R/C Frame-Wall Structures," by A. E. Aktan and V. V. Bertero - July 1982 (PB83 147 736)A05

UCB/EERC-82/07   "Further Study of the Earthquake Response of a Broad Cylindrical Liquid-Storage Tank Model," by G. C. Manos and R. W. Clough - July 1982 (PB83 147 744)A11

UCB/EERC-82/08   "An Evaluation of the Design and Analytical Seismic Response of a Seven Story Reinforced Concrete Frame - Wall Structure," by F. A. Charney and V. V. Bertero - July 1982(PB83 157 628)A09

UCB/EERC-82/09   "Fluid-Structure Interactions: Added Mass Computations for Incompressible Fluid," by J. S.-H. Kuo - August 1982 (PB83 156 281)A07

UCB/EERC-82/10   "Joint-Opening Nonlinear Mechanism: Interface Smeared Crack Model," by J. S.-H. Kuo - August 1982 (PB83 149 195)A05

UCB/EERC-82/11   "Dynamic Response Analysis of Techi Dam," by R. W. Clough, R. M. Stephen and J. S.-H. Kuo - August 1982 (PB83 147 496)A06

UCB/EERC-82/12   "Prediction of the Seismic Responses of R/C Frame-Coupled Wall Structures," by A. E. Aktan, V. V. Bertero and M. Piazza - August 1982 (PB83 149 203)A09

UCB/EERC-82/13   "Preliminary Report on the SMART 1 Strong Motion Array in Taiwan," by B. A. Bolt, C. H. Loh, J. Penzien, Y. B. Tsai and Y. T. Yeh - August 1982 (PB83 159 400)A10

UCB/EERC-82/14   "Shaking-Table Studies of an Eccentrically X-Braced Steel Structure," by M. S. Yang - September 1982 (PB83 260 778)A12

UCB/EERC-82/15   "The Performance of Stairways in Earthquakes," by C. Roha, J. W. Axley and V. V. Bertero - September 1982 (PB83 157 693)A07

UCB/EERC-82/16   "The Behavior of Submerged Multiple Bodies in Earthquakes," by W.-G. Liao - Sept. 1982 (PB83 158 709)A07

UCB/EERC-82/17   "Effects of Concrete Types and Loading Conditions on Local Bond-Slip Relationships," by A. D. Cowell, E. P. Popov and V. V. Bertero - September 1982 (PB83 153 577)A04

UCB/EERC-82/18 "Mechanical Behavior of Shear Wall Vertical Boundary Members: An Experimental Investigation," by M. T. Wagner and V. V. Bertero - October 1982 (PB83 159 764)A05

UCB/EERC-82/19 "Experimental Studies of Multi-support Seismic Loading on Piping Systems," by J. M. Kelly and A. D. Cowell - November 1982

UCB/EERC-82/20 "Generalized Plastic Hinge Concepts for 3D Beam-Column Elements," by P. F.-S. Chen and G. H. Powell - November 1982 (PB03 247 981)A13

UCB/EERC-82/21 "ANSR-III: General Purpose Computer Program for Nonlinear Structural Analysis," by C. V. Oughourlian and G. H. Powell - November 1982 (PB83 251 330)A12

UCB/EERC-82/22 "Solution Strategies for Statically Loaded Nonlinear Structures," by J. W. Simons and G. H. Powell - November 1982 (PB83 197 970)A06

UCB/EERC-82/23 "Analytical Model of Deformed Bar Anchorages under Generalized Excitations," by V. Ciampi, R. Eligehausen, V. V. Bertero and E. P. Popov - November 1982 (PB83 169 532)A06

UCB/EERC-82/24 "A Mathematical Model for the Response of Masonry Walls to Dynamic Excitations," by H. Sucuoğlu, Y. Mengi and H. D. McNiven - November 1982 (PB83 169 011)A07

UCB/EERC-82/25 "Earthquake Response Considerations of Broad Liquid Storage Tanks," by F. J. Cambra - November 1982 (PB83 251 215)A09

UCB/EERC-82/26 "Computational Models for Cyclic Plasticity, Rate Dependence and Creep," by B. Mosaddad and G. H. Powell - November 1982 (PB83 245 829)A08

UCB/EERC-82/27 "Inelastic Analysis of Piping and Tubular Structures," by M. Mahasuverachai and G. H. Powell - November 1982 (PB83 249 987)A07

UCB/EERC-83/01 "The Economic Feasibility of Seismic Rehabilitation of Buildings by Base Isolation," by J. M. Kelly - January 1983 (PB83 197 988)A05

UCB/EERC-83/02 "Seismic Moment Connections for Moment-Resisting Steel Frames," by E. P. Popov - January 1983 (PB83 195 412)A04

UCB/EERC-83/03 "Design of Links and Beam-to-Column Connections for Eccentrically Braced Steel Frames," by E. P. Popov and J. O. Malley - January 1983 (PB83 194 811)A04

UCB/EERC-83/04 "Numerical Techniques for the Evaluation of Soil-Structure Interaction Effects in the Time Domain," by E. Bayo and E. L. Wilson - February 1983 (PB83 245 605)A09

UCB/EERC-83/05 "A Transducer for Measuring the Internal Forces in the Columns of a Frame-Wall Reinforced Concrete Structure," by R. Sause and V. V. Bertero - May 1983 (PB84 119 494)A06

UCB/EERC-83/06 "Dynamic Interactions between Floating Ice and Offshore Structures," by P. Croteau - May 1983 (PB84 119 486)A16

UCB/EERC-83/07 "Dynamic Analysis of Multiply Tuned and Arbitrarily Supported Secondary Systems," by T. Igusa and A. Der Kiureghian - June 1983 (PB84 118 272)A11

UCB/EERC-83/08 "A Laboratory Study of Submerged Multi-body Systems in Earthquakes," by G. R. Ansari - June 1983 (PB83 261 842)A17

UCB/EERC-83/09 "Effects of Transient Foundation Uplift on Earthquake Response of Structures," by C.-S. Yim and A. K. Chopra - June 1983 (PB83 261 396)A07

UCB/EERC-83/10 "Optimal Design of Friction-Braced Frames under Seismic Loading," by M. A. Austin and K. S. Pister - June 1983 (PB84 119 288)A06

UCB/EERC-83/11 "Shaking Table Study of Single-Story Masonry Houses: Dynamic Performance under Three Component Seismic Input and Recommendations," by G. C. Manos, R. W. Clough and R. L. Mayes - June 1983

UCB/EERC-83/12 "Experimental Error Propagation in Pseudodynamic Testing," by P. B. Shing and S. A. Mahin - June 1983 (PB84 119 270)A09

UCB/EERC-83/13 "Experimental and Analytical Predictions of the Mechanical Characteristics of a 1/5-scale Model of a 7-story R/C Frame-Wall Building Structure," by A. E. Aktan, V. V. Bertero, A. A. Chowdhury and T. Nagashima - August 1983 (PB84 119 213)A07

UCB/EERC-83/14 "Shaking Table Tests of Large-Panel Precast Concrete Building System Assemblages," by M. G. Oliva and R. W. Clough - August 1983

UCB/EERC-83/15 "Seismic Behavior of Active Beam Links in Eccentrically Braced Frames," by K. D. Hjelmstad and E. P. Popov - July 1983 (PB84 119 676)A09

UCB/EERC-83/16 "System Identification of Structures with Joint Rotation," by J. S. Dimsdale and H. D. McNiven - July 1983

UCB/EERC-83/17 "Construction of Inelastic Response Spectra for Single-Degree-of-Freedom Systems," by S. Mahin and J. Lin - July 1983

UCB/EERC-83/18 "Interactive Computer Analysis Methods for Predicting the Inelastic Cyclic Behaviour of Structural Sections," by S. Kaba and S. Mahin - July 1983 (PB84 192 012) A06

133

UCB/EERC-83/19   "Effects of Bond Deterioration on Hysteretic Behavior of Reinforced Concrete Joints," by F.C. Filippou, E.P. Popov and V.V. Bertero - August 1983 (PB84 192 020) A10

UCB/EERC-83/20   "Analytical and Experimental Correlation of Large-Panel Precast Building System Performance," by M.G. Oliva, R.W. Clough, M. Velkov, P. Gavrilovic and J. Petrovski - November 1983

UCB/EERC-83/21   "Mechanical Characteristics of Materials Used in a 1/5 Scale Model of a 7-Story Reinforced Concrete Test Structure," by V.V. Bertero, A.E. Aktan, H.G. Harris and A.A. Chowdhury - September 1983 (PB84 193 697) A05

UCB/EERC-83/22   "Hybrid Modelling of Soil-Structure Interaction in Layered Media," by T.-J. Tzong and J. Penzien - October 1983 (PB84 192 178) A08

UCB/EERC-83/23   "Local Bond Stress-Slip Relationships of Deformed Bars under Generalized Excitations," by R. Eligehausen, E.P. Popov and V.V. Bertero - October 1983 (PB84 192 848) A09

UCB/EERC-83/24   "Design Considerations for Shear Links in Eccentrically Braced Frames," by J.O. Malley and E.P. Popov - November 1983 (PB84 192 186) A07

UCB/EERC-84/01   "Pseudodynamic Test Method for Seismic Performance Evaluation: Theory and Implementation," by P.-S. B. Shing and S. A. Mahin - January 1984 (PB84 190 644) A08

UCB/EERC-84/02   "Dynamic Response Behavior of Xiang Hong Dian Dam," by R.W. Clough, K.-T. Chang, H.-Q. Chen, R.M. Stephen, G.-L. Wang, and Y. Ghanaat - April 1984

UCB/EERC-84/03   "Refined Modelling of Reinforced Concrete Columns for Seismic Analysis," by S.A. Kaba and S.A. Mahin - April, 1984

UCB/EERC-84/04   "A New Floor Response Spectrum Method for Seismic Analysis of Multiply Supported Secondary Systems," by A. Asfura and A. Der Kiureghian - June 1984

UCB/EERC-84/05   "Earthquake Simulation Tests and Associated Studies of a 1/5th-scale Model of a 7-Story R/C Frame-Wall Test Structure," by V.V. Bertero, A.E. Aktan, F.A. Charney and R. Sause - June 1984

UCB/EERC-84/06   "R/C Structural Walls: Seismic Design for Shear," by A.E. Aktan and V.V. Bertero

UCB/EERC-84/07   "Behavior of Interior and Exterior Flat-Plate Connections subjected to Inelastic Load Reversals," by H.L. Zee and J.P. Moehle

UCB/EERC-84/08   "Experimental Study of the Seismic Behavior of a two-story Flat-Plate Structure," by J.W. Diebold and J.P. Moehle

UCB/EERC-84/09   "Phenomenological Modeling of Steel Braces under Cyclic Loading," by K. Ikeda, S.A. Mahin and S.N. Dermitzakis - May 1984

UCB/EERC-84/10   "Earthquake Analysis and Response of Concrete Gravity Dams," by G. Fenves and A.K. Chopra - August 1984

UCB/EERC-84/11   "EAGD-84: A Computer Program for Earthquake Analysis of Concrete Gravity Dams," by G. Fenves and A.K. Chopra - August 1984

UCB/EERC-84/12   "A Refined Physical Theory Model for Predicting the Seismic Behavior of Braced Steel Frames," by K. Ikeda and S.A. Mahin - July 1984

UCB/EERC-84/13   "Earthquake Engineering Research at Berkeley - 1984" - August 1984

UCB/EERC-84/14   "Moduli and Damping Factors for Dynamic Analyses of Cohesionless Soils," by H.B. Seed, R.T. Wong, I.M. Idriss and K. Tokimatsu - September 1984

UCB/EERC-84/15   "The Influence of SPT Procedures in Soil Liquefaction Resistance Evaluations," by H. B. Seed, K. Tokimatsu, L. F. Harder and R. M. Chung - October 1984

UCB/EERC-84/16   "Simplified Procedures for the Evaluation of Settlements in Sands Due to Earthquake Shaking," by K. Tokimatsu and H. B. Seed - October 1984

UCB/EERC-84/17   "Evaluation and Improvement of Energy Absorption Characteristics of Bridges under Seismic Conditions," by R. A. Imbsen and J. Penzien - November 1984

UCB/EERC-84/18   "Structure-Foundation Interactions under Dynamic Loads," by W. D. Liu and J. Penzien - November 1984

UCB/EERC-84/19   "Seismic Modelling of Deep Foundations," by C.-H. Chen and J. Penzien - November 1984

UCB/EERC-84/20   "Dynamic Response Behavior of Quan Shui Dam," by R. W. Clough, K.-T. Chang, H.-Q. Chen, R. M. Stephen, Y. Ghanaat and J.-H. Qi - November 1984

UCB/EERC-85/01   "Simplified Methods of Analysis for Earthquake Resistant Design of Buildings," by E. F. Cruz and A. K. Chopra - February 1985

UCB/EERC-85/02   "Estimation of Seismic Wave Coherency and Rupture Velocity using the SMART 1 Strong-Motion Array Recordings," by N.A. Abrahamson - March 1985